Improved Design and Performance of Haptic Two-Port Networks through Force Feedback and Passive Actuators

A Thesis
Presented to
The Academic Faculty

by

Lawrence J. Tognetti

In Partial Fulfillment
of the Requirements for the Degree of
Doctor of Philosophy

School of Mechanical Engineering
Georgia Institute of Technology
January 2005

Improved Design and Performance of Haptic Two-Port Networks through Force Feedback and Passive Actuators

Approved by:

Dr. Wayne Book, Committee Chair
School of Mechanical Engineering
Georgia Institute of Technology

Dr. David Taylor
School of Electrical & Computer Engineering
Georgia Institute of Technology

Dr. Amy Pritchett
School of Industrial & Systems Engineering
School of Aerospace Engineering
Georgia Institute of Technology

Dr. Imme Ebert-Uphoff
School of Mechanical Engineering
Georgia Institute of Technology

Dr. Nader Sadegh
School of Mechanical Engineering
Georgia Institute of Technology

Date Approved: January 10, 2005

Dedicated to both my parents, Rod and Laurette Tognetti, my living grandfather Julius Faoro, and my "adopted grandmother" Betty Hayes, who are always in my thoughts.

ACKNOWLEDGEMENTS

I give my thanks to Dr. Book for sticking with me through my "brief" stay at Georgia Tech and providing the resources and guidance to pursue this project. I thank my committee members for taking the time to meet with me and providing assistance when approached. I also thank Davin Swanson for our countless hours of Diesel talk, Ryan Krauss for his friendship over the past year, and J.D. Huggins for his friendship and assistance with all the hardware projects.

My family has given invaluable support throughout my graduate career, for without them I would not have made it this far. I also thank the Burgess, Trimble, and Jacob families for providing a family away from home.

My time at Georgia Tech would not have been as enjoyable if I did not have the opportunity to be involved with Outdoor Recreation Georgia Tech (ORGT), which ultimately lead to my cherished relationship with Andrea and the close friends we have in the Dogwood City Grotto.

TABLE OF CONTENTS

LIST OF TABLES

LIST OF FIGURES

SUMMARY

Haptic systems incorporate many different components, ranging from virtual simulations, physical robotic displays (super joysticks), robotic slaves, signal communication, and digital control; two-port networks offer compact and modular organization of such haptic components. By establishing specific stability properties of the individual component networks, their control parameters can be tuned independently of external components or interfacing environment. This allows the development of independent haptic two-port networks for interfacing with a class of haptic components. Furthermore, by using the two-port network with virtual coupling paradigm to analyze linear haptic systems, the complete duality between an admittance controlled device with velocity (position) feedback and virtual coupling can be compared to an impedance controlled device with force feedback and virtual coupling.

This research first provides background on linear haptic two-port networks and use of Llewelyn's Stability Criterion to prove their stability when interfaced with passive environments, with specific comments regarding application of these linear techniques to nonlinear systems. Furthermore, man–machine interaction dynamics are addressed, with specific attention given to the "human is a passive element" assumption and how to include estimated human impedance / admittance dynamic limits into the two–port design. Two–port numerical tuning algorithms and analysis techniques are presented and lay the groundwork for testing of said haptic networks on HuRBiRT (Human Robotic Bilateral Research Tool), a large scale nonlinear hybrid active / passive haptic display.

First, two–port networks are numerically tuned using a linearized dynamic model of

HuRBiRT. Resulting admittance and impedance limits of the respective networks are compared to add insight on the advantages / disadvantages of the two different implementations of haptic causality for the same device, with specific consideration given to the advantage of adding force feedback to the impedance network, selection of virtual coupling form, effects of varying system parameters (such as physical or EMF damping, filters, etc.), and effects of adding human dynamic limits into the network formulation. Impedance and admittance two–port network implementations are experimentally validated on HuRBiRT, adding further practical insight into network formulation. Resulting experimental networks are directly compared to those numerically formulated through use of HuRBiRT's linearized dynamic models.

CHAPTER 1

HAPTICS INTRODUCTION & BACKGROUND

As we approach the 21st century, programmable and intelligent mechanical systems are becoming more prevalent in our lives. One particular area of interest is mechanical systems intended for use directly with humans; such systems share desired workspace and interact with humans to complete specific tasks. More explicitly, many of these devices consist of a mechanism that an operator physically manipulates to position a particular part of the device or "end point". The mechanical system may merely record the "end point's" path or restrict an operator's movements to a preprogrammed path, possibly assisting the operator's effort. This chapter first presents several classifications of haptic devices. After this various relevant research topics are touched upon, with special attention given to possible hybrid active / passive systems and passivity control of active systems.

1.1 Human Machine Interface Classifications and Applications

The first classification of devices are completely passive and intended to only record and compare information. A computer interface may be utilized to visually assist an operator in maneuvering the device by graphically showing where the end point is in comparison to a desired position. The device's "end point" may hold a specific tool, part, or mechanical jig to be held in place, while built in brakes lock the system once it is in proper position. Such a device acts as a holder, allowing the operator to perform a desired job without worrying about keeping the tool, part, or jig steady. Potential applications are assembly, medical, or machining processes. Two such surgical examples are operations where a needle must be held constant while being inserted in the patient or machining where a template is held in position as the tool performs its task along the guide. For instance John Hopkins uses

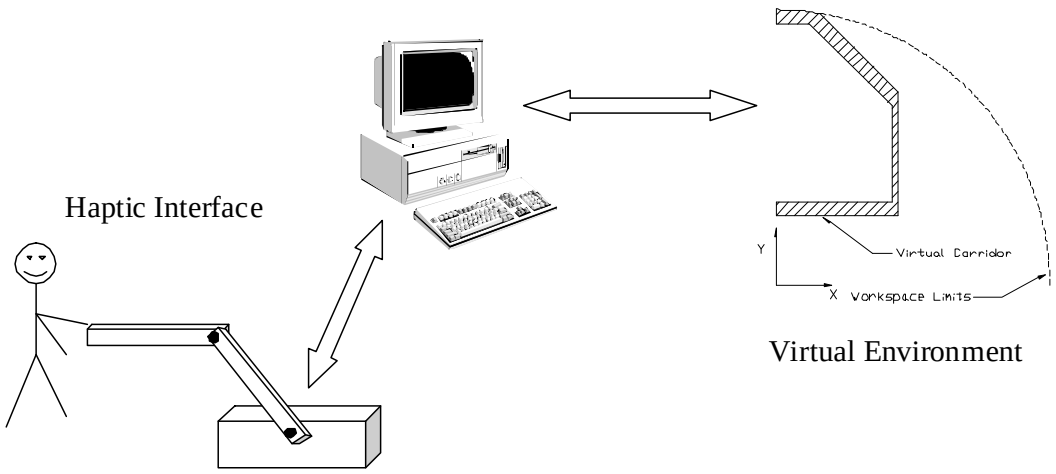

Figure 1: Haptic System

a 7 dof passive arm with central braking to position PAKY (Percutaneous Access of the Kidney), a needle insertion mechanism.[81] Furthermore, such position sensing devices may be used as joysticks for unilateral tele-operation of another machine, similar to existing joysticks except that the device's kinematics are tailored to match the remote machine's configuration or task's natural motion. As can be inferred, these systems are entirely passive and rely solely on the operator to move and restrict motion of the device; intrinsically making a safe operator / machine interface.

Next in this progression is for the haptic system to work with the operator to restrict or aid in the device's motion, feeding back tactile information to the user. Devices (joy stick, mouse, or large scale mechanism) that relay tactile information back to the user with regards to position, machine being tele-operated, or virtual environment being simulated are referred to as synergistic systems.[141] These devices may relay scaled force or position constraint information based on the programmed virtual environment, slave actuator limitations, and environment of the remote tele-operated machine (slave).[87, 86] One such application studied by Salcudean is the bilateral tele-operation of earth excavation equipment.[116] In this example the haptic controller of a backhoe relays information regarding hardness of earth being excavated or obstacles in the workspace to the user. Another application of synergistic haptic interfaces in manufacturing is as an assembly tool. Here the haptic interface

Table 1: Various Active Haptic Devices

Haptic Device	PI or Facilities	Kinematic Form
Phantom	Sensable Technologies	5 Bar Mechanism + pivot
HuRBiRT	Book	5 Bar Mechanism (planar)
High Bandwidth Force Display	Hannaford, Adams	X - Y Table
Excalibur	Haptic Technologies	X-Y Table
Twin Pantograph	Salcudean	5 Dof twin Pantograph
Mag Lev Joy Stick	Salcudean	Magnetically Levitated
Steady-Hand	John Hopkins	7 DOF Tool Holder

might be a mechanism that holds an assembly part either too heavy or delicate for the line worker to handle. The worker can now direct the haptic mechanism to correctly position the assembly part, but the worker is restricted to moving the part into the correct location and orientation because of the haptic interface's pre-programmable path.[145] Because the haptic device may be reprogrammed for changes in assembly part or processes, it is more versatile than a dedicated assembly machine. Furthermore, the device may supply most of the required force for movement, but only travels in the direction guided by the operator and at a rate proportional to the operator's input force.[31, 56] Because the required force to impart motion is shared by the operator and the device's actuators, the operator feels tactile information from the performed task. Such machines can act as force multipliers, allowing an operator to maneuver tools and objects much heavier than ordinarily possible while still feeling tactile information based on the operation or programmed restrictions. On the other hand this type of device can be used to scale down forces and filter "unsteady" tremors produced by humans at small movements, ultimately increasing the resolution of tactile sense and motion available to the operator.[78]

Synergistic systems may be accomplished through restricting the device's motion with motors, creating an actively actuated haptic device. Table 1 lists several active haptic devices, who the principle investigator (PI) developing the device is or where (Facilities) the device is being developed, and the primary kinematics they are based on. Due to the size or nature of specific applications it may not be desirable to use an active haptic interface with capabilities of unpredictable self-initiated motion, potentially overpowering or

Table 2: Various Passively Actuated Haptic Interfaces

Haptic Device	PI or Facilities	Passive Actuation
Cobots	Colgate & Peshkin	Continuos Variable Transmission
PADyC	Troccaz	One way clutches for velocity constraints
PTER	Book	Electromagnetic Friction Clutches
PALM-V2	Kanade	Hydraulic Cylinders
6 DOF Joystick	Crane & Chesney	Hysteresis Clutches
Mag Lev Joy Stick	Salcudean	Magnetically Levitated
Steady-Hand	John Hopkins	7 DOF Tool Holder

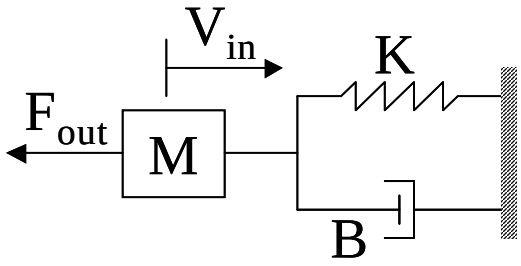

Figure 2: Impedance Causality

interfering with the human's input. Alternatively, passively actuated haptic interfaces do not use actuators capable of adding energy to the system, but rather utilize actuators that dissipate, store, or redirect user-supplied energy. This may be accomplished through modulating clutches / brakes, continuous variable transmissions, or fluid systems. Table 2 lists several passively actuated haptic devices, who the principle investigator (PI) developing the device is or where (Facilities) the device is being developed, and the primary forms of passive actuation.

1.2 Haptic Impedance and Admittance

Force and velocity interactions between objects have ambiguous causality in the real world. For example, is an object's trajectory / deflection a causal function of applied force, or is its resistive forces a causal function of applied trajectory / deflection? Is this causality relationship different for compliant and stiff interactions? Control of haptic interfaces requires an assumption of what variables in the system are considered input and output. Implementation causality of a haptic interface, slave device, or virtual environment can be

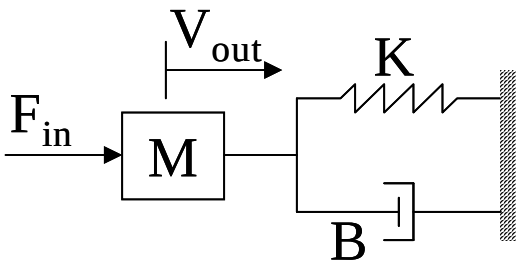

Figure 3: Admittance Causality

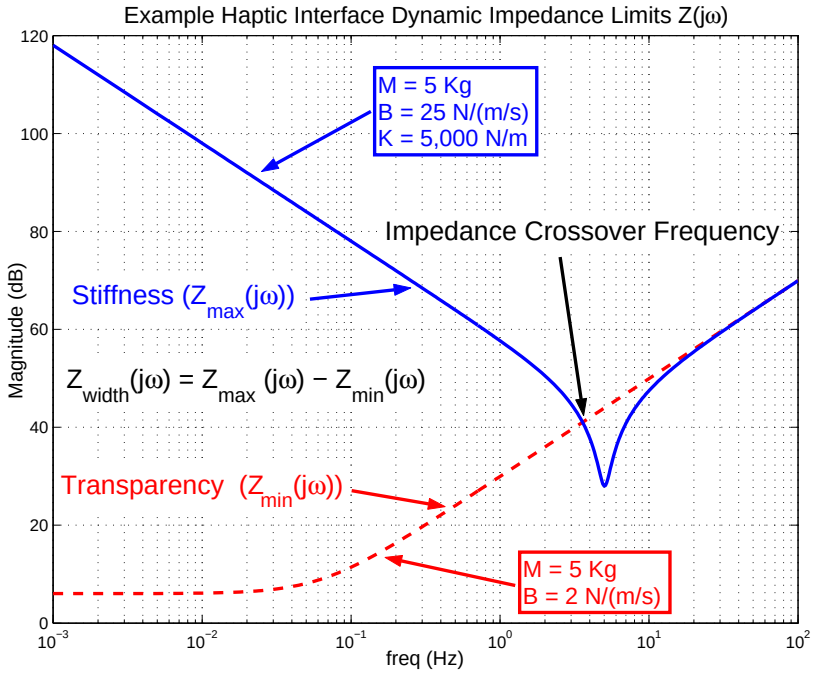

Figure 4: Illustration of Haptic Interface Dynamic Impedance Limits

categorized as either an impedance or admittance. An impedance interface or environment is designed to generate forces based on measured velocity, or rate of deflection, as illustrated in figure 2. Such an impedance causality can be described by the differential equation

$$F_{out} = M\frac{dV_{in}}{dt} + BV_{in} + K\int V_{in}dt \tag{1}$$

or transfer function

$$Z(s) = \frac{F_{out}(s)}{V_{in}(s)} = \left(Ms + B + \frac{1}{s}K\right) \tag{2}$$

where $Z(s)$ is referred to as the complex impedance. Alternatively, if as illustrated by figure 3 an interface or environment is designed to deflect (rate of deflection) based on an applied force, it is an admittance interface. Admittance causality illustrated in figure 3 can be described by the complex admittance $Y(s)$ defined as

$$Y(s) = \frac{V_{out}(s)}{F_{in}(s)} = \frac{s}{(Ms^2 + Bs + K)} \tag{3}$$

The primary difference between the two implementations is the causality of what is considered input and what is considered output, with a system's admittance being the inverse of its impedance. Note that F_{in} in the admittance structure, which is an actuating force, is the opposite direction of F_{out} in the impedance structure, which is a restive force. Though some devices may be designed for both haptic interface implementations, admittance devices tend to be larger and less back drivable while impedance devices tend to be light with back drivable actuators. Traditionally impedance (Z) and admittance (Y) of mechanical devices and haptic interfaces are expressed in terms of velocity and force (or torque) so that passivity properties of the device can be easily assessed.

An ideal haptic interface would be capable of emulating any desired impedance or admittance, but a haptic interface's performance abilities are limited by system dynamics, haptic control architecture, and control stability. Figure 4 and 5 respectively illustrate example impedance and admittance limits that a device may have. In these figures the minimum impedance (maximum admittance) is limited to dynamics equivalent of a mass with damping and the maximum impedance (minimum admittance) is limited to the dynamics of a

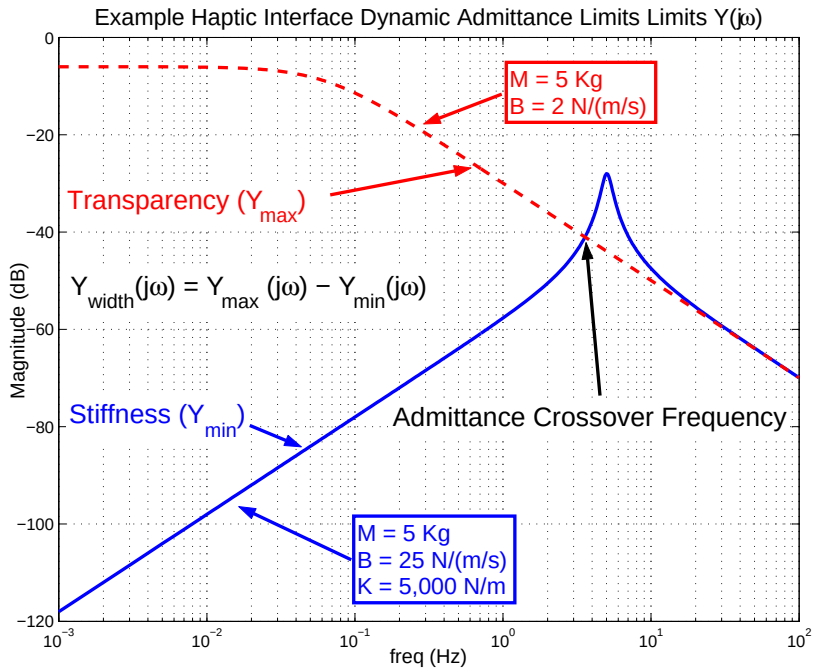

Figure 5: Illustration of Haptic Interface Dynamic Admittance Limits

mass–spring–damper. Minimum admittance (Y_{min}) and maximum impedance (Z_{max}) are referred to as the stiffness limit, while minimum impedance (Z_{min}) and maximum admittance (Y_{max}) are referred to as the transparency limit. The device's programmable range of achievable impedance or admittance for a given frequency is the Z_{width} and Y_{width} respectively. Another important property is the impedance crossover and admittance crossover frequency which represent the system's bandwidth; the frequency at which Z_{width} and Y_{width} approach zero, signifying the device can not accurately emulate or reflect varying dynamics at frequencies above the crossover.

1.3 Research Topics for Haptic Devices

As alluded to earlier, stability of the haptic device and ultimately safety of the user is very important. Active systems pose safety concerns when reflecting large forces. Some researchers are avoiding this problem by scaling their devices and using velocity control mode for force feedback, while others are exploring various ways to passively implement a

haptic device. Because passively actuated reflecting and guiding devices do not have mechanisms for imparting motion to the system, other than redirecting energy already provided by the user, these devices are intrinsically the safest forms of synergistic haptic interfaces. Unfortunately the design and implementation of such inherently passive devices is proving to be a challenging and difficult task with fundamental limitations. Alternatively, some researchers are using passivity theory based dynamic analysis and control formulation in the development of their control algorithms; guaranteeing stable closed loop control of an actively actuated device when the interface is in contact with passive environments, including interaction of the master with the human and slave with the remote environment.[24, 2] Two major assumptions are that the operator (human) and remote or virtual environment are passive. These assumptions have led some to investigate the effects of digital control and numerical simulation on violating the passive condition.[14, 34, 12] Of course modeling the human user to assist in controller design and guaranteeing passivity is also an important issue. The assumption of the human operator as a passive element and allowing passivity based controller design has stemmed from Hogan's work regarding modeling the human's muscular response.[61]

Other pertinent topics include performance and effectiveness of haptic interfaces along with human perception, or psychophysics, associated with a haptic device.[137, 16, 97] What form should the haptic device take? Should admittance or impedance algorithms be utilized? Hollerbach suggests that people tend to adapt to a device's characteristics, making the choice not critical.[65] Through the two–port formulation, Adams and Hannaford begin to show duality between configuring a haptic device in impedance or admittance form.[2] Salcudean discusses the benefit of using a network that can be switched from impedance to admittance, depending on the task at hand, or actual environment stiffness.[116] Salcudean uses full four-channel feedback, communicating both the haptic device's force and velocity to the slave and visa versa; allowing the relative communication gains to be adjusted so as to tune the haptic interface as admittance, impedance, or somewhere in between.

With respect to mechanical performance characteristics, what is the range of achievable dynamic impedance (Z width) or admittance (Y width) the device can simulate? What is the device's transparency, or minimum impedance (maximum admittance)? How stiff an environment can the device simulate? These are important properties that must be addressed when designing both the physical device and its control system. Devices with low damping and minimal dynamics are proven to provide superior transparency, while devices with large physical damping have proven more capable of simulating stiff environments. Theoretically it is true that a negative damping in the control can compensate for high physical damping, this can prove to be troublesome when implementing the algorithms digitally or with analog components. Another method is to utilize direct force feedback control on measured user applied force to compensate for any natural physical impedance, such as damping or friction, but direct force feedback has often proven to be a challenging stability problem. Future chapters will investigate with more detail such direct force feedback control.

1.4 Hybrid Active / Passive Haptic Systems

As mentioned earlier, passively actuated haptic devices have faced fundamental limitations. Hybrid active / passive devices that use both active and passive actuators (controllable dampers, clutches, or brakes) to bridge the performance gap is a fairly unexplored topic. Conceivably, a haptic device can safely reflect large-scale forces or limit velocities by synergistically using both active and passive actuators. Added safety comes from using passive actuators for the majority of the force reflection or kinematics' constraint and small motors to compensate for deficiencies possessed by a completely passive device. Such a device could be constructed so as to allow the active or passive element to be either locked or freed, allowing a comparison of the individual haptic contributions from each respective actuator. Two possible methodologies for combining the passive and active actuators, in series or in parallel, are presented.

By combining passive and active actuators in series, controllable dampers can be used

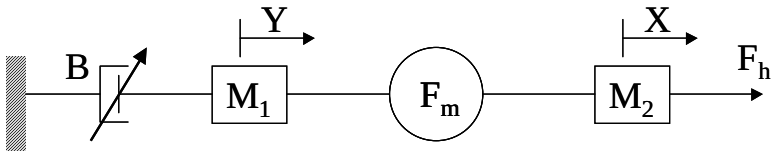

Figure 6: Active & Passive Actuators in Series (damper grounded)

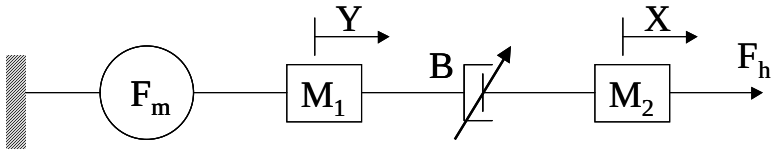

Figure 7: Active & Passive Actuators in Series (motor grounded)

to limit force and / or velocity transmitted by the motors. If one considers M_1 in figures 6 and 7 to be negligible, analogous to having the motor and damper directly connected in series at the device's base, both figure 6 and 7 are equivalent. If M_2 is considered negligible, analogous to a macro / micro configuration, then figure 6 and 7 are not equivalent. Rather figure 7 is similar to assembly mechanisms with structural compliance / admittance at the "wrist" for limiting forces. Such assembly mechanisms utilize small dampers at the tip and larger motors at the base for global positioning. Alternatively, in a haptic device it may be more desirable to use dampers as macro manipulators and utilize smaller motors at the tip (figure 6).

Sakaguchi has developed a variation of the active passive combination illustrated in figure 7.[111, 112, 113] He uses a motor to power the input of an electrorheological particle fluid clutch, forming what is referenced as an ER actuator. Though the motor in the ER actuator is set to a steady predetermined velocity, by utilizing an internal drive train it is capable of transmitting torque through ER clutches in either rotational direction of the ER actuator's output shaft. Sakaguchi found that output torque of an ER clutch utilizing particle type ER fluid was proportional to the applied voltage and fairly independent of the clutch's slip speed. Based on this observation, the developed ER actuator can be thought of as a torque source with very low inertia that is limited to a maximum driving velocity equal to that of the motor.

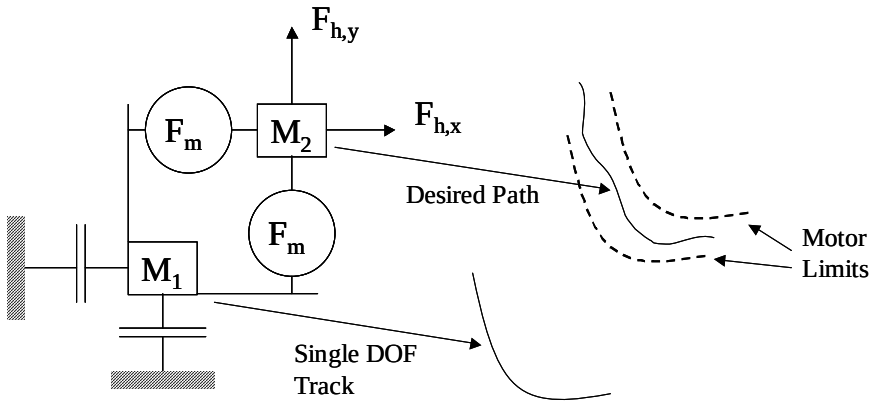

Figure 8: Two DOF Device Using Motors in Series with Brakes

Another alternative for an active / passive series synergistic device is to use locking brakes instead of programmable dampers. As illustrated in figure 8, brakes can be used to lock a multi degree of freedom mechanism to a single degree of freedom path while small micro motors at the tip of the device can perform small-scale adjustments to the device's actual path or desired resisting forces. In this configuration the actual path of tip travel is limited to the motor's window of motion with respect to the constrained single DOF path.

Traditionally motors in a haptic device are configured to allow back drive ability. One unexplored advantage of implementing admittance control with non-back drivable motors is high resisting forces can be maintained while still limiting the achievable driving force. One example of a non–back drivable gear train is the worm drive gearbox, which locks when external torque tries to directly drive the output shaft. Extending the use of non-back drivable motors in series with brakes as macro passive actuators, the tip of the haptic device could be fixed relative to the "locked" single DOF path without any motor activation force. Of course traditional admittance control laws utilizing "force" feedback would be required to provide tactile feedback.

Another method of increasing damping through use of DC electric motors is to utilize back EMF generated by the motor. For example, if an electric motor's leads are shorted

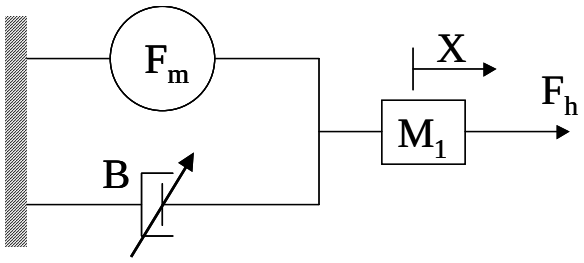

Figure 9: Active & Passive Actuators in Parallel

when the motor is manually turned by an externally applied torque, the motor will provide EMF damping from the current flow generated by the back EMF; essentially turning the motor into an electric generator. While this allows DC motors to be used as stand alone passive actuators, if the appropriate drive motor circuit were designed such back EMF can be harnessed from the "active" drive motors. Though in its initial stages, Colgate is currently investigating such use of back EMF damping in a haptic device's architecture. One method of utilizing back EMF from the drive motors, though not necessarily the same method used by Colgate, is outlined in Appendix B. Method outlined in Appendix B provides increased high frequency damping while simultaneously providing a lag–lead filter in the motor's drive circuit.

By having a synergistic system comprised of active and passive elements in parallel (see figure 9), algorithms can be developed to minimize actuation of the active elements by shifting the emphasis to the passive elements. Active actuators can be used to assist with gravity compensation and feedback linearization for improved transparency, while adjustable dampers can be used to reflect large dynamic forces and tune the device's Z width to match the task at hand. For example Massimo and Tadros found magnetic particle brakes, though not ideal dampers, were effective at creating safe large resistive impulse forces when simulating walls, but had residual torque when deactivated.[110, 132, 109] It was also found that resistive devices had trouble implementing frictionless walls unless the wall was orthogonal to the brake's DOF; rendering simulating arbitrarily orientated frictionless walls as not possible. Furthermore, by having the passive device in parallel with the active device, the passive device can be used to directly resist excessive forces generated by

the active actuator. As alluded to earlier, increased Z width of the device from the use of controllable physical damping is another characteristic that can be investigated through use of existing control theory and experimentation. Sakaguchi, though looking at the problem of robotic control and not haptic devices, found the use of an electrorheological homogeneous fluid clutch as an adjustable damper helped increase the gain margin of a system, allowing stiffer servo control.[45, 134, 135]

1.5 Passivity of Discretely Controlled Single DOF "Active" System

Colgate and his researchers used both Nyquist Criterion and Passivity formulation to independently derive an expression for unconditional stability of a single degree of freedom impedance haptic device, modeled as an inertia with damping (b), in contact with an impedance virtual environment, and discretely controlled with sampling period (T).[24] If the virtual coupling to the real environment is modeled as a spring (K), damper (B) and discretely implemented with backwards difference numerical differentiation, the condition can be simplified to

$$b > \frac{KT}{2} + |B| \tag{4}$$

The importance of this result is that it introduces the relationship of physical damping with the maximum achievable virtual stiffness and virtual damping. The first consequence is that the more rapidly the control system digitally samples, the higher the achievable virtual stiffness. Likewise, the more physical damping in the haptic system, the higher the achievable virtual stiffness. This leads to the conclusion that although eliminating physical damping when designing a haptic interface increases the device's transparency, it is not beneficial for simulating stiff environments. It should be noted that Colgate found passivity was a conservative condition for stability. By modeling the human as an arbitrary spring,

the virtual stiffness and damping relationships with respect to the physical damping are numerically found by investigating the discrete system's closed loop characteristic equation's Z domain poles. Their results are graphically presented and can be viewed in Colgate and Shankel's work.

Hannaford and Adams propose lumping the haptic device and haptic algorithm into a linear two–port system, analogous to a linear two–port electrical network.[2] This allows existing passivity and stability conditions derived in network theory to be applied to the haptic system. In network theory the input and output vectors of the two–port network are constructed from combinations of voltage and current signals. For mechanical systems, the input and output vectors represent combinations of velocity and force signals.

1.6 Contributions of this Research

Following chapters build on the two–port haptic network paradigm introduced by Adams and Hannaford through the following:

1. Investigation of how nonlinear components affect the application of previously used two–port passivity based stability criteria.

2. Expansion of the concept of virtual coupling to nonintuitive forms.

3. Introduction of force feedback into the traditional impedance two–port network.

4. Showing the true duality between the traditional admittance and traditional impedance two–port networks, giving insight into velocity and force feedback controller selection.

5. Proposed biomechanical based human dynamic models for interaction with mechanical devices are demonstrated using one human subject's frequency response to device perturbations. Resulting model properties are compared with various human models published in haptic literature.

6. Incorporation of human models as impedance or admittance limits and the investigation of how using experimentally determined human models affects selection of the two–port control parameters.

7. Application of the two–port haptic network analysis to a hybrid active / passive in parallel device and analysis of DC motor back EMF damping.

8. Experimental validation of haptic two–port network stability on a nonlinear two DOF haptic device that can be configured to provide admittance or impedance reflection, with one DOF converted so as to provide an axis of hybrid active / passive actuation.

CHAPTER 2

HUMAN INTERACTION WITH MECHANICAL SYSTEMS

Much interest has been expressed in understanding human behavior when interfaced with mechanical systems. Many researchers have attempted to describe the human's dynamics with linear, quasi-linear, optimal, and decision making models. Alternatively, some classify the human as passive, which carries implicit model properties. Historically the majority of human modeling has been with respect to pilot modeling by the aerospace community, though recently the haptic community has become interested in use of human models for designing and evaluating haptic controllers. Unfortunately there is little continuity between human modeling in the haptic community with previous work done by the aerospace community. Furthermore, accurate modeling of the human is not a simple task. McRuer and Jex expressed it well when they wrote

> "The human pilot is a multi mode, adaptive, learning controller capable of exhibiting an enormous variety of behavior" [92]

This complex and diverse human behavior is what makes the human so difficult to model. The following sections give a general overview of some human properties and established models. Comments on the assumption of the human as a passive element will be presented, along with a proposed method of treating existing experimentally determined human models as limiting cases rather than strict models.

2.1 Basic Human Characteristics

Humans tend to operate in three general modes; compensatory, pursuit, and precognitive, with these modes not being mutually exclusive. Humans have the ability to rely on combinations of each to achieve the best performance results.[147, 124, 91]

Compensatory mode consists of the human solely operating on error between desired and actual trajectory, often modeled as a traditional negative feedback system. Given such a compensatory action it is accepted that with sufficient practice and ability, the human develops a stable closed loop relationship that provides desired response characteristics, suppresses disturbances, and compensates for variations in the control loop.[92] For the most part, compensatory models are more prevalent in aerospace-based human models. Such models are in the form of single input - single output, unless multiple task compensatory models are being evaluated. Similarly, compensatory displays only communicate error to the operator and do not give any further information relating to the desired trajectory.

Pursuit is when the human acts in an open loop fashion with respect to desired trajectory, though they may have a priori knowledge of the plant and interface's dynamics and possibly a preview of the desired trajectory. In this mode the human may use this knowledge to adjust his / her dynamics through anticipation to cancel the dynamics of the plant being interfaced / controlled. Usually pursuit action is used to augment compensatory action, requiring a human model that incorporates two inputs and a single output. Pursuit behavior can be facilitated by a display that relays both desired trajectory and actual system path as opposed to just error. One example of pursuit reaction is tracking of a pure sine wave. It has been found that the human's response will initially lag the desired wave, but will eventually lock on. This is a result of the human anticipating the desired wave and adjusting the output accordingly.

Lastly, precognitive mode is when the human is highly trained and familiar with the system and task. This allows the human to "intuitively" react based on familiarity, often

related to muscle memory. Such examples may be driving a vehicle down a well-known windy driveway, typing at a keyboard, or any highly trained skill.

Other qualitative characteristics humans exhibit is the perception of position changes more precisely than velocity and velocity more precisely than acceleration. The human's output is usually defined as a position, with the derivation of required force to achieve such a position being automatic.[147] Furthermore it is accepted that the human's response contains some time delay associated with decision-making and the neuromuscular system. Actual delay may vary with complexity of the system being controlled or frequency of the signal being worked with. It has been reported that the human's delay can range from 150 - 300 ms when controlling zero and first order systems and 400 - 500 ms when controlling second order systems; with the increased decision making complexity of controlling a second order system causing the longer delay.[147] Exact delay is operator specific and varies based on different factors, such as training, environment, and multitasking of several activities. It should be noted that some researchers have determined the human's compensatory controller bandwidth for random signals to be between 0.5 and 1.0 Hz, corresponding to the ability of responding with approximately two tracking control actions per second. Alternatively, when the human is attempting to track predictable signals it has been shown they can follow signals as high as 2 or 3 Hz.[147].

2.2 Various Human models

Several researchers have used optimal control to model the human, theorizing the human works to minimize some cost function. These models may be simple bang-bang control or more thorough modern linear models, some incorporating Kalman filters.[124, 91] Cost functions for these optimal models usually take the form of quadratic equations incorporating input (u) or input rate ($\dot{u}$), state (x), and possibly output (y). The linear models can either be tuned by picking a cost function and adjusting specific free model parameters to fit the human's response, or by adjusting the cost function to tune the model's response

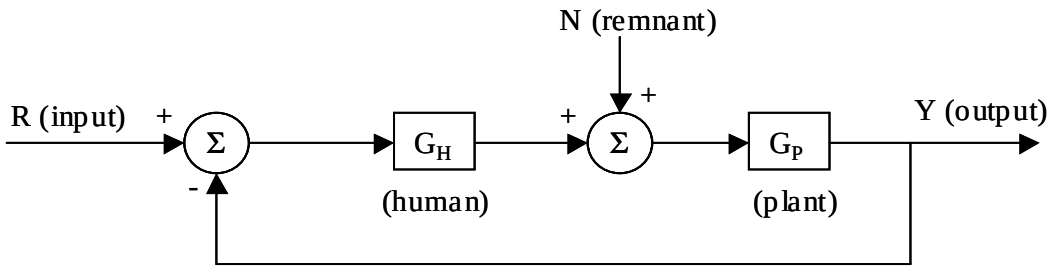

Figure 10: Human in the Loop Compensatory Control

to match the human's. Baron and Kleinman did some work with respect to adding human motor noise, muscular lag, and time delay to the model so as to better fit experimental data.[124] Modeling the human as an optimal controller has shown some success, but complexity and the increased number of parameters in the model make it somewhat laborious to apply. Furthermore, the optimal solution to one set of model parameters (such as time constants & noise parameters) and cost function may match the optimal solution to another set of parameters and cost function. One advantage of the optimal control model is that it can handle multi-input multi-output systems, as long as they are linear.

McRuer developed a slightly different approach to modeling the human in compensatory mode.[124, 92] He relied on quasi-linear models, where a non-linear system's response to a specific input can be split into a linear system and a remnant. The linear response is based on a linear model that closely matches the true system, while the remnant is the difference between the linear model and actual system response; often considered as an additional noise element with a broadband power spectral density. Furthermore, McRuer approached the problem by modeling the combined human / interface feed-forward transfer function instead of just the human. What he found was the human adjusted his / her dynamics based on the system being controlled so as to approach a desired feed-forward combination ($G_{OL} = G_H G_P$ in figure 10).

McRuer reported that the human strives to achieve an open loop gain much greater than unity for low frequencies so as to minimize low frequency error. Furthermore, for a

wide range of controlled dynamics the human worked to achieve a -20 db/decade gain vs frequency characteristic near the open loop crossover frequency. In addition to the 90° ($\pi/2$ radians) phase lag associated with the -20 db/decade, additional phase lag associated with reaction time and neuromuscular dynamics can be modeled near the crossover frequency as a pure time delay. McRuer used this information to model the open loop frequency function as

$$G_H G_P = G_{OL} = \frac{\omega_c e^{-j\omega\tau_e}}{j\omega} \tag{5}$$

referred to as the crossover model. This model is reported to capture magnitude data more accurately than phase. Because of this an extended crossover model, or α model, was formulated

$$G_H G_P = G_{OL} = \frac{\omega_c e^{-j(\omega\tau_e + \alpha/\omega)}}{j\omega} \tag{6}$$

It was found that even when the human controlled mildly unstable systems, the resulting open loop system could be approximated with the crossover model. This reassures the human's ability to stabilize certain systems; of course this ability is limited by the severity of the instability and the skill of the operator. In order to minimize least squared error, the operator can adjust the open loop gain (ω_c) and phase margin (by adjusting delay, τ_e); though it is reported that the crossover frequency is fairly constant for a given set of task variables, but usually limited to less than 10 rad/sec because of the lags associated with the pure time delay. Humans also have the ability to continually fine–tune their dynamics so as to compensate for varying dynamics in the interface, sustaining a fairly constant crossover model; such as when the interface's dynamics are smoothly time varying. Other factors that may contribute to different open loop gains (crossover frequency), effective time delay, and remnant "noise" are environmental, training, or human's mental and physical condition; such as being alert or intoxicated.

Given a task, or interface dynamics, and a highly skilled operator, McRuer found crossover frequency and time delay of the open loop dynamics were slightly dependent on the bandwidth of the input signal (ω_i). That is crossover frequency slightly increased and time delay decreased with increasing input signal bandwidth. He further stated that

crossover frequency was more dependent on the form of the controlled element's dynamics than on the input signal bandwidth. McRuer developed some relationships determining the neutrally stable crossover frequency (ω_{c0}) from a human's "relaxed" time delay (τ_0); which itself was dependent on the dynamic form of the controlled element. Neutrally stable crossover frequency is defined as the required crossover frequency (gain) to provide marginal stability when the input signal has an extremely low bandwidth and the human is exhibiting the "relaxed" delay. Relaxed delay is defined as the human's delay (τ_e) when frequency lead isn't used to cancel neuromuscular lags, as is the case for input signals with very low bandwidths. Relaxed time delay is found by extrapolating the human's time delay vs input bandwidth (τ_e vs. ω_i) relationship to vanishing input bandwidths ($\omega_i = 0$). As the input signal bandwidth increases, the human adjusts his / her delay by tightening up their neuromuscular loop, increasing the system's phase margin and effective closed loop damping. As long as the input signal bandwidth was considerably less than the neutrally stable crossover frequency, specifically ($\omega_i < 0.8\omega_{c0}$), McRuer found the crossover frequency was fairly independent of input bandwidth. In contrast, when the input bandwidth approached the crossover frequency, specifically ($\omega_i > 0.8\omega_{c0}$), the human reduces the crossover frequency to values much lower than the input bandwidth, effectively filtering out high frequency noise.

As noted earlier, remnant is the deviation of the true model from the approximated linear model. McRuer explains that the sources of remnant are pure noise injection, nonlinear operations, and non-steady operator behavior. Pure noise injection comes from various neuromuscular and sensing actions. Nonlinear operations include indifference thresholds, saturation, or other actions involving nonlinear actions. Non-steady operator behavior refers to deviations of the actual pilots behavior from the "averaged" quasi-linear model. Such time varying deviations may include pilot gain and delay. It has been found that remnant increases with increasing controlled element gain, resulting in a greater percentage of the system output being related to the remnant than the linear portion of the model. This causes decreased model accuracy when used on human controlled systems with high gains.

It has also been claimed that the crossover model breaks down when the human is attempting to control highly unstable systems or lightly damped high order systems.

Inaba and Matsuo investigated the crossover model characteristics of the operator in a single degree of freedom force reflective manual control system by performing tests for various programmed interface device dynamics, ranging from zero order to second order.[66] In conclusion they reported that the operator acted like a differentiator when interfaced with second order dynamics, a pure gain when interfaced with first order dynamics, but failed to act as an integrator when interfaced with zero order dynamics. It was also found the human could not shape the open loop characteristics into integral like form when interfaced with second order system requiring a high crossover frequency. For the most part, it was found that when interfaced with a haptic device the human could be characterized using the crossover model, with similar crossover frequencies as those reported in past work by McRuer.

2.3 Human as a Passive Element

In 1989 Neville Hogan published the idea of the human operator acting as a passive element. Specifically, Hogan stated

> "the human arm exhibits the impedance of a passive object, despite active neuromuscular feedback."[61]

Hogan's paper serves as a cornerstone for many others relying on the human as a passive element to guarantee stability of their haptic system. As many others have stated, Hogan comments that the human operator is very complex and difficult to characterize. By being able to classify the human operator as a passive element, implicit stability properties can be relied upon to design the haptic control algorithm.

To understand how Hogan came to classify the human's arm impedance as passive, one must look further back to the testing he, Bizzi, and Mussa-Ivaldi performed.[100] They

set out to characterize the steady state spring like behavior of the neuromuscular system. They wanted to measure the force / displacement relationship for different postures of the arm-hand serial linkage when the hand is displaced from an equilibrium position. This was accomplished by asking four human subjects to position a haptic device's handle in a specific location and then giving the device a random sequence of displacements in varying magnitude (5 or 8 mm) and direction (0 to 315 degrees, graduated in 45 degree increments). Because the steady state reaction force associated with the neuromuscular system was of interest and not the cognitive response of the human, the subjects were asked to delay their voluntary reaction by focusing on the direction of displacement, counting to three, and then move rapidly in the direction opposite to the imposed displacement. This allowed Hogan, Bizzi, and Mussa-Ivaldi to measure the steady state reaction force before the human voluntarily reacted to the disturbance. Again this was done for different postures to see how different positioning of the arm-elbow changed the resulting reaction forces. In order to produce a control data set, the human was replaced with a physical spring and the same tests were repeated.

For each human subject and arm posture the resulting measured reaction force was expressed as a two-dimensional stiffness matrix. This matrix was then split into symmetric and anti-symmetric components, with the symmetric part representing the conservative spring like component and the anti-symmetric part representing any non-conservative reaction forces. Because the curl, a way of representing the anti-symmetric component, gives rise to a static force field such that there exists a closed loop path through which power can be indefinitely extracted while moving along, the anti-symmetric portion of the stiffness matrix represents an active component. On the other hand, the symmetric component of the stiffness matrix can be associated with the potential energy stored by displacing the hand. On two of the subjects it was found that the curl was statistically insignificant, while the curl was showed to be statistically significant for the remaining two subjects. In his subsequent paper, Hogan further goes to show that the symmetric component of the stiffness matrix is positive definite, a property signifying a passive mechanical spring system.

From the assumption of a negligible anti-symmetric component and a positive definite symmetric component, Hogan derives the human acts as an element with a passive precognitive neuromuscular system.

Hogan followed up on the idea of the human having variable impedance and the ability to stabilize a system. He used a haptic device programmed with positive virtual stiffness and negative virtual damping. The subjects were instructed to move the handle, instigating oscillation around the equilibrium position from the negative damping. He then modeled the response as a lightly damped second order system, extracting the exponential growth and oscillating frequency. This information was used to determine effective stiffness, inertia, and damping of the operator / device combination. Hogan also noted that the response quit growing after several oscillations. Hogan's results showed that given the same negative damping, but differing virtual stiffness, the human's stiffness remained fairly constant. This is not too surprising since Mussa-Ivaldi found varying human stiffness was detected to be more defendant on varying global configurations of the arm to achieve the equivalent hand position rather than from varying interface stiffness or disturbances. Given McRuer's findings that the human, within his / her capabilities, works towards stabilizing the interfaced system, it is not surprising that Hogan found the human attempted to cancel the effects of the negative damping.

2.4 Can the Human in the Loop be Passive?

As mentioned earlier, many have taken Hogan's hypothesis of the steady state precognitive neuromuscular response being a passive element and extended it to classify the human as a passive element. The problem with this extension is that the human will not solely act in a precognitive manner when interfacing with haptic devices. Furthermore it has been accepted that all humans exhibit a pure time delay, either due to neuromuscular lags or reaction time. Once again, Hogan's analysis only dealt with the neuromuscular's steady state response and did not look into its dynamic response or lags. In order for a linear

system, or a linear approximation of a system, to be passive it must not exceed a 90° phase lag (or lead) between power variables (force & velocity). This is not possible for a linear system with a pure time delay because of the delay's linear phase lag contribution (with respect to input frequency). For example, given a human with an overall quick time delay of 150 ms, any input signal with frequency components greater than ≈ 0.5 rad / sec (≈ 1.67 Hz) will cause the delay's phase lag contribution to surpass 90°.

This is not to say that the human will destabilize a system designed to guarantee passivity. Many have found success with their passivity based haptic controllers. It is known that stability based on passivity is conservative with respect to other stability criteria. Compiled with the generally accepted hypotheses that a human will work to stabilize a system to the best of his / her ability, it is not surprising that stability of these haptic systems is maintained with the human in the loop. The human also has the advantage of using pursuit control to stabilize a system once a repeatable response is detected, as well as compensatory control to improve upon the pursuit's accuracy.

Stability problems will arise when the frequency of the response / input signal or system instability surpasses the human's pursuit and compensatory tracking capabilities. Such examples are when the gain of the interface increase beyond the human's ability to maintain proper open loop phase margin. Such situations often lead to "Pilot Induced Oscillations", where the response of the human lags behind the compensatory error signal such that the human loses control.

2.5 Modeling Human Impedance & Admittance Limits

Various researchers have attempted to model the human's gross arm control through traditional linear system identification of a mechanical system linked with the human arm, then subtracting out the known device dynamics. As already discussed, Hogan used this method to experimentally derive equation (7) as a second order estimate of the Human's

precognitive response when subjected to a perturbation. [61, 100]

$$Z_h = \frac{F}{\dot{X}} = \frac{0.8s^2 + 5.5s + 568}{s} \frac{N}{m/s} \tag{7}$$

Kosuge similarly used frequency based system identification methods to derive equation (8) as an estimate of the Human arm when interfaced with a mechanical system. [73]

$$Z_h = \frac{F}{\dot{X}} = \frac{1.95s^2 + 2.46s + 55}{s} \frac{N}{m/s} \tag{8}$$

As McGruer commented, the human is a very adaptive and changing dynamic system, changing his / her dynamics to deal with the task at hand. Models (7) and (8) were based on data from how a human reacts to a perturbation or sinusoidal forcing function. If the human lets go or changes intensity of the grip, the dynamic model changes. While modeling of human interaction with mechanical systems may be too complex to accurately achieve for all circumstances, ignoring humans' physical characteristics may not be realistic and may lead to an undesirable controller. For example, the human does not have infinite impedance or infinite bandwidth. As mentioned before, it has been estimated that the human's compensatory bandwidth for random signals to be less than 10 rad/sec (≈1.6 Hz). Furthermore, although the human may act as an infinite admittance by simply letting go of the device, it may not act as infinite impedance. The human, no matter how strong, will have compliance. Hogan's and Kosuge's models were derived while the human was trying to accurately regulate about a position, therefore models derived from such test can be thought of as impedance limits, or the maximum stiffness the human can exhibit. Similarly, Adams and Hannaford choose to use equation (9) as an estimate of the maximum human impedance when tuning their haptic networks. [3]

$$Z_{h(\max)} = \frac{F}{\dot{X}} = \frac{300s + 1000}{s} \frac{N}{m/s} \tag{9}$$

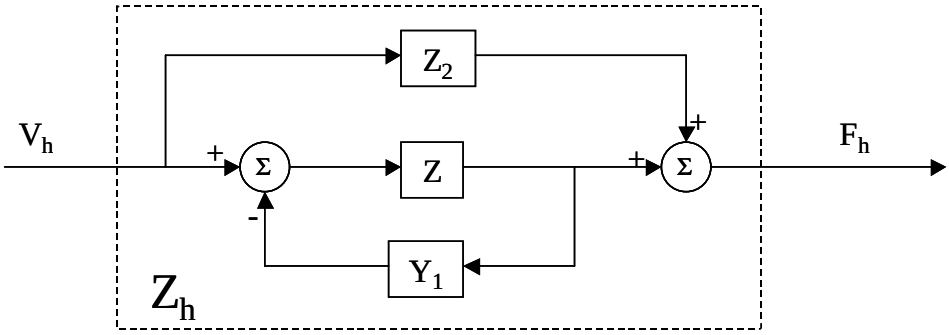

Figure 11: Human Impedance Model with Limits

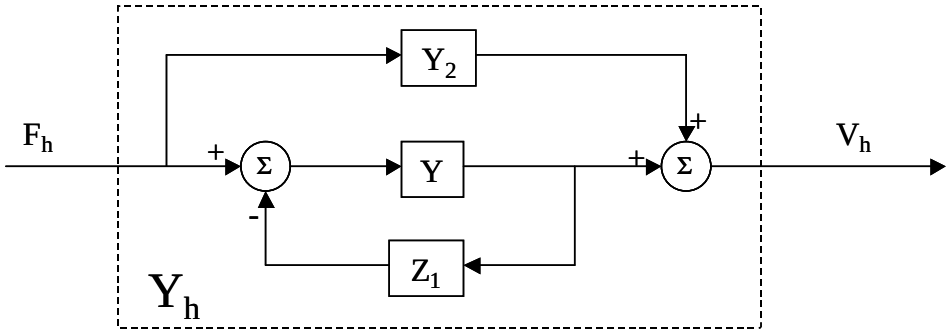

Figure 12: Human Admittance Model with Limits

How do these human models, or human impedance limits compare? Adams and Hannaford's model describes the human as having a first order cut off frequency of 3.33 rad/sec (0.53 Hz) through an equivalent damping of 300 N/(m/s) and a stiffness of 1000 N/m, but has no provisions for human arm mass. Kosuge's model incorporates a human arm mass in addition to the damping and stiffness. Their model describes a second order system with mass of 1.95 kg, a natural frequency of 5.31 rad/sec (0.85 Hz), and a damping ratio of 0.12. Similarly, Hogan's model is a second order system with mass of 0.8 kg, a natural frequency of 26.65 rad/sec (4.24 Hz), and a damping ratio of 0.13.

How can these impedance and admittance limits be incorporated into haptic algorithm design? First, assume the general human impedance and admittance models were estimated by the simple block diagrams outlined in figures 11 and 12 respectively, with Z and Y representing the human's desired impedance and admittance, then the remaining elements in the block diagram can be used to tune the human's actual limits. Two extreme cases

must be considered to do this, the first is when the human lets go and offers zero impedance and the second is when the human grasp as stiff as possible and applies their maximum impedance, or minimum admittance. First, lets consider the impedance model illustrated in figure 11, which has an overall transfer function of

$$Z_h = Z_2 + \frac{Z}{1 + Y_1 Z} \tag{10}$$

where Z is an intended impedance that ranges from zero to infinity and Z_1 & Z_2 represent the human's limits. If we let Z approach zero, for zero intended impedance as in the case when the human lets go, then the transfer function becomes

$$Z_{h(\min)} = Z_h|_{Z \to 0} = Z_2 \tag{11}$$

On the other hand, if the human grasps as tight as possible and acts as stiff as they are capable of, then we let the intended impedance, Z, approach infinity.

$$Z_{h(\max)} = Z_h|_{Z \to \infty} = Z_2 + \frac{1}{Y_1} = Z_2 + Z_1 \tag{12}$$

We know that when the human lets go they apply zero impedance to the device, therefore $Z_{h(\min)}$ must equal zero, which requires Z_2 to be zero. On the other hand, when the human acts as stiff as possible they are limited by their max impedance, therefore $Z_{h(\max)}$ must equal the model for maximum impedance. Since Z_2 is zero, Y_1 must be the inverse of the maximum impedance estimate.

Similarly, the overall transfer function for the admittance model can be expressed as

$$Y_h = Y_2 + \frac{Y}{1 + Z_1 Y} \tag{13}$$

where Y is an intended admittance that ranges from zero to infinity and Y_1 & Y_2 represent the human's limits. If we let Y approach infinity, for zero intended impedance or maximum intended admittance as in the case when the human lets go, then the transfer function becomes

$$Y_{h(\max)} = Y_h|_{Y \to \infty} = Y_2 + \frac{1}{Z_1} = Y_2 + Y_1 \tag{14}$$

On the other hand, if the human grasps as tight as possible and acts as stiff as they are capable of, then we let the desired admittance, Y, approach zero.

$$Y_{h(\min)} = Y_h|_{Y \to 0} = Y_2 \tag{15}$$

Again, we know when the human acts as stiff as possible they are limited by their max impedance, or minimum admittance, therefore $Y_{h(\min)}$ must equal the inverse of the model for maximum impedance. Furthermore, when the human lets go of the device they apply zero impedance, or infinite admittance, to the device; therefore $Y_{h(\max)}$ must equal infinity; this requires Y_1 to be infinity, or Z_1 to be zero.

Later chapters will illustrate how this modeling of human limits can be incorporated into design of the haptic system. Doing so allows controller stability constraints to be relaxed through knowledge of the human's dynamic limitations and exact modeling of the varying human is not necesary.

CHAPTER 3

PASSIVITY CONTROL OF TWO-PORT NETWORKS

Researchers are using passivity theory to select control parameters and algorithms that guarantee unconditional stability of active haptic devices when interfaced with a passive environment or virtual environment. If the haptic interface, consisting of the device and its control algorithms, can be considered passive or even dissipative, then it will not add energy to the human user or environment. If the human operator and the interaction environment are assumed to be passive, the complete system will be stable.

Several passivity haptic control schemes use virtual coupling to connect the haptic device to the virtual environment or slave, as will be covered in a later chapter. Virtual coupling essentially adds predetermined admittance / impedance limits into the haptic algorithm.[2, 24] This sets the maximum impedance or minimum admittance the device can simulate, regardless of the actual environment. Others use software programmed energy storage elements to conserve energy put into the system so that it may be used for future actuation; either continual energy checking or preset energy reservoir algorithms are used so as to guarantee their system, a two–port network, does not "generate" energy. [82]

One compact method for organizing haptic and bilateral teleoperation systems is through two–port networks. Sections in this chapter first introduce general two–port networks with respect to haptic systems. Existing stability criteria for linear two–port networks are presented, along with it's application to nonlinear two–port networks.

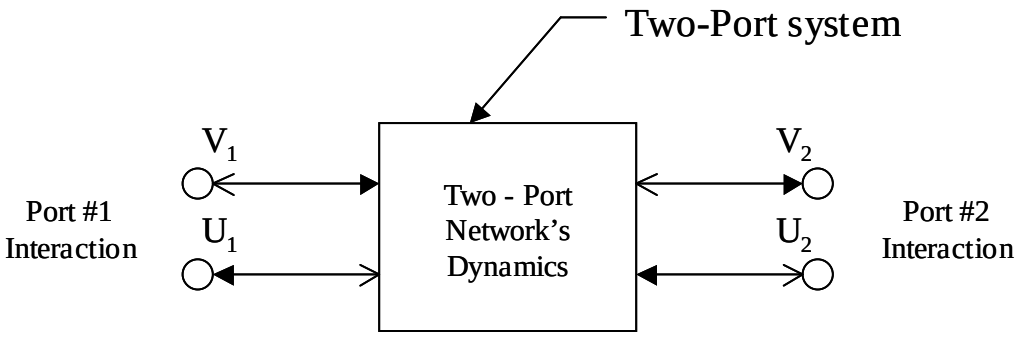

Figure 13: General Two–Port Network

3.1 General Two–Port Networks

Typically two–port networks utilize their "power variables" as inputs and outputs, such as current and voltage for electrical circuits or force and velocity for mechanical systems. The two–port network illustrated in figure 13 shows V_1 & U_2 as the inputs and U_1 & V_2 as the outputs (dark arrows) or U_1 & V_2 as the inputs and V_1 & U_2 as the outputs (light arrows); though any input / output permutation of the ports' respective power variables is possible. In the following discussions an impedance master (port #1) with an admittance slave, or environment, (port #2) will be used as the example system. Similarly, other two–port networks based on any of the other power variable permutations for input & output could be used for parallel discussions.

Linear two–port networks have been widely studied in network theory, lending existing linear passivity and stability criteria. In its most general form, a two–port network does not have to be linear and can take the form of

$$\begin{aligned} \dot{X} &= F_1(X, V_1, U_2, t) \\ \begin{bmatrix} U_1 \\ V_2 \end{bmatrix} &= \begin{bmatrix} H_1(X, V_1, U_2, t) \\ H_2(X, V_1, U_2, t) \end{bmatrix} \end{aligned} \tag{16}$$

where X represents the system's state vector and V_1 & U_2 are the system's inputs. For any general nonlinear N port network, given that the power variables of a real N-port network

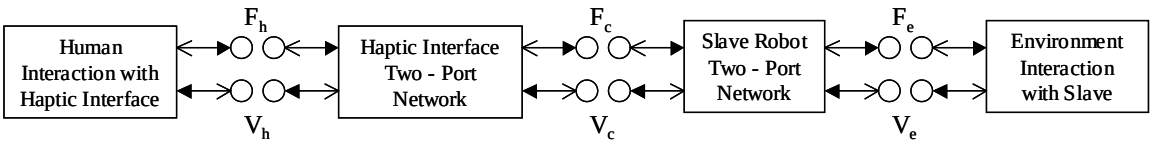

Figure 14: Haptic System Constructed with Two–Port Networks

can be represented as

$$U = \begin{bmatrix} u_1 \\ \vdots \\ u_n \end{bmatrix} \quad , \quad V = \begin{bmatrix} v_1 \\ \vdots \\ v_2 \end{bmatrix} \tag{17}$$

the system can be classified as passive if

$$\int_{t_0}^{t} V^T(\tau) U(\tau) d\tau + \varepsilon(t_0) \geq 0 \tag{18}$$

where $\varepsilon(t_0)$ is the initial energy stored in the system.

One advantage of two–port networks is that they allow system components to be lumped into a single model or separated into modular components. For example, one two–port model could describe a haptic interface, another for the remote device, and terminating one–port networks used to complete the system; stability of each two–port network can then be independently investigated.

3.2 Linear Time Invariant Two–Port Networks

One special case of two–port networks is linear, time invariant, two–port networks. Considerable work has been done in network theory concerning this special case. In network theory each two–port network can be described as passive, active, generative, or absolutely stable, with some of the definitions overlapping.[59] For example, given an impedance haptic device to be matched with an admittance environment or slave, the linear, time invariant two–port network's frequency response can be expressed as

$$\begin{bmatrix} u_1(j\omega) \\ -\hat{v}_2(j\omega) \end{bmatrix} = \begin{bmatrix} p_{11}(j\omega) & p_{12}(j\omega) \\ p_{21}(j\omega) & p_{22}(j\omega) \end{bmatrix} \begin{bmatrix} v_1(j\omega) \\ u_2(j\omega) \end{bmatrix} = P(j\omega) \begin{bmatrix} v_1(j\omega) \\ u_2(j\omega) \end{bmatrix} \tag{19}$$

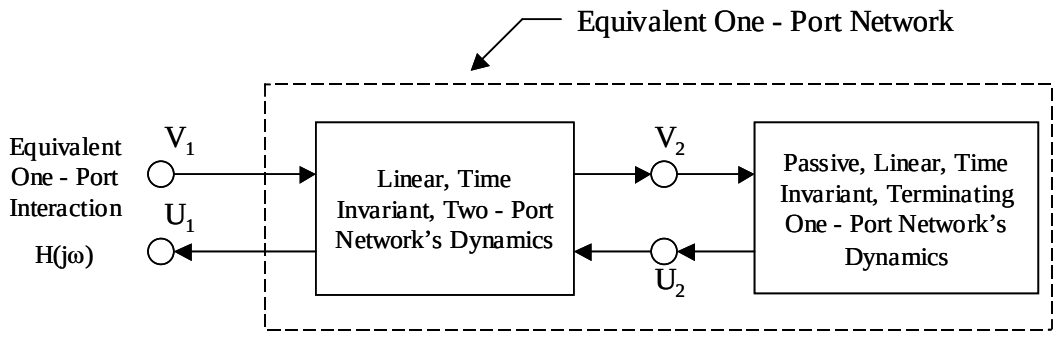

Figure 15: Equivalent One–Port from Terminated Two–Port Network

where each term in the $P(j\omega)$ matrix represents a frequency transfer function. Equation (19) uses $-\hat{v}_2(j\omega) = v_2(j\omega)$ in substitute of $v_2(j\omega)$ so that power associated with port two, specifically $\hat{v}_2^T(j\omega)u_2(j\omega)$, corresponds to the power flow out of port two. Similarly other combinations of impedance or admittance haptic devices can be matched with impedance or admittance slave / environments to form an equivalent two–port network. Each element of $P(\cdot)$ must be analytic in the complex right half plane and $P(j\omega)$ must be positive semi-definite. Requiring $P(j\omega)$ to be positive semi definite is equivalent to

$$\begin{aligned} \mathrm{Re}(p_{11}) \geq 0 \quad &, \quad \mathrm{Re}(p_{22}) \geq 0 \\ \mathrm{Re}(p_{11})\mathrm{Re}(p_{22}) \quad &- \quad \left|\frac{p_{21} + \bar{p}_{12}}{2}\right|^2 \geq 0, \quad \forall\omega \geq 0 \end{aligned} \tag{20}$$

a condition based on the Hermitian of $P(j\omega)$ [59]

$$He\left(P(j\omega)\right) = P(j\omega) + P(-j\omega)^T \tag{21}$$

Conversely, if the system is not passive it is considered active and $P(j\omega)$ is negative definite; if $P(j\omega)$ is semi-negative definite the system is considered generative.[76] Though passivity of a network results in implicit stability properties, it is often conservative with respect to stability. This led Llewelyn to develop a condition for absolute stability when assuming the two–port network was interfaced with a linear, time invariant, passive terminating one–port.

Llewelyn developed a set of conditions to guarantee that when the two–port network was terminated by a linear, time invariant, one port network, the equivalent overall linear time invariant one–port network ($H(j\omega)$) was passive. (figure 15) By assuming a terminating

port's frequency transfer function of

$$\frac{u_2(j\omega)}{v_2(j\omega)} = S(j\omega) \quad \& \quad \mathrm{Re}\left[S(j\omega)\right] \geq 0, \quad \forall\omega \geq 0 \tag{22}$$

Llewelyn desired the resulting overall equivalent two–port network to take the form of

$$\frac{u_1(j\omega)}{v_1(j\omega)} = H(j\omega) \quad \& \quad \mathrm{Re}\left[H(j\omega)\right] \geq 0, \quad \forall\omega \geq 0 \tag{23}$$

It was determined this could be guaranteed if the two–port network satisfied the following conditions.[59, 76]

$$\begin{aligned} \mathrm{Re}(p_{11}) \geq 0 \quad &, \quad \mathrm{Re}(p_{22}) \geq 0 \\ 2\mathrm{Re}(p_{11})\mathrm{Re}(p_{22}) \quad &\geq \quad |p_{12}p_{21}| + \mathrm{Re}(p_{12}p_{21}), \quad \forall\omega \geq 0 \end{aligned} \tag{24}$$

This criterion, referred to as Llewelyn's stability criterion, is not as restrictive as requiring the two–port network itself to be passive. Upon comparing the Llewelyn criterion with the criterion for passivity, it can be seen that only the third condition differs. As outlined by Haykin, if the third condition for Llewelyn stability is expressed as

$$\frac{\mathrm{Re}\left[\sqrt{p_{12}p_{21}}\right]}{\sqrt{\mathrm{Re}\left[p_{11}\right]\mathrm{Re}\left[p_{22}\right]}} \leq 1 \tag{25}$$

and the third condition for two–port passivity is expressed as

$$\frac{\left(\mathrm{Re}\left[\sqrt{p_{12}p_{21}}\right]\right)^2}{\mathrm{Re}\left[p_{11}\right]\mathrm{Re}\left[p_{22}\right]} + \frac{\left(|p_{12}| - |p_{21}|\right)^2}{4\mathrm{Re}\left[p_{11}\right]\mathrm{Re}\left[p_{22}\right]} \leq 1 \tag{26}$$

then a graphical comparison of the two criteria can be illustrated by plotting

$$\frac{\left(|p_{12}| - |p_{21}|\right)}{2\sqrt{\mathrm{Re}\left[p_{11}\right]\mathrm{Re}\left[p_{22}\right]}} \quad \text{vs.} \quad \frac{\mathrm{Re}\left[\sqrt{p_{12}p_{21}}\right]}{\sqrt{\mathrm{Re}\left[p_{11}\right]\mathrm{Re}\left[p_{22}\right]}} \tag{27}$$

as in figure 16.[59] It can be seen that passivity restrains the parameters to be contained within a unity circle, while the Llewelyn criterion only restricts one of the parameters to be less than unity.

Through inspection of the two conditions, passivity and Llewelyn stable, along with the original two–port model, insight to the advantage of the Llewelyn criterion can be seen. If the haptic device and the slave environment / device are comparably scaled so that velocity

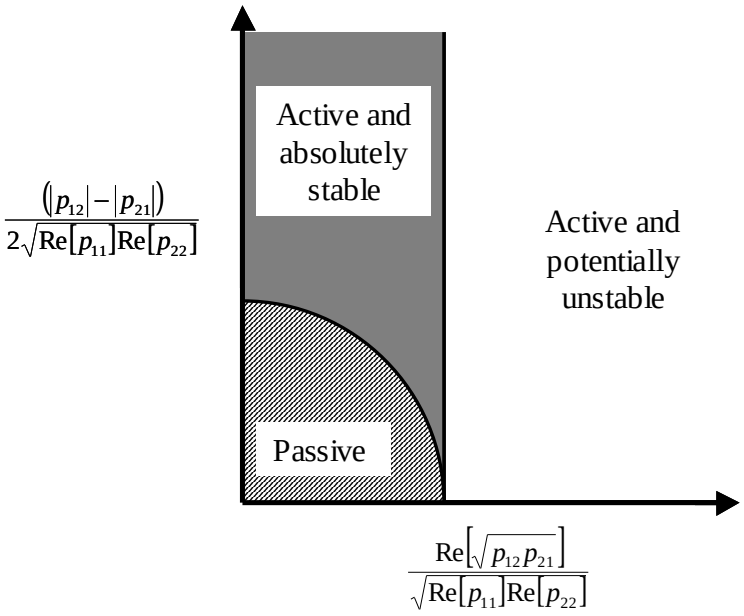

Figure 16: Comparison of Passivity with Llewelyn Stability (only positive quadrant shown)

and force directly map between the two, then the terms p_{12} and p_{21} will be approximately equivalent in magnitude. In this case, passivity and Llewelyn stability are comparable, as can be seen by inspecting figure 16. Alternatively, if the environment / slave and the haptic device are not comparably scaled so that the control system must scale the communicated velocity and force measurements, the off diagonal terms will be modified by some scaling factor. If such a scaling factor were to be taken as "$n(j\omega)$", equation (19) becomes

$$\begin{bmatrix} u_1(j\omega) \\ -\hat{v}_2(j\omega) \end{bmatrix} = \begin{bmatrix} p_{11}(j\omega) & n(j\omega)^{-1}p_{12}(j\omega) \\ n(j\omega)p_{21}(j\omega) & p_{22}(j\omega) \end{bmatrix} \begin{bmatrix} v_1(j\omega) \\ u_2(j\omega) \end{bmatrix} = P(j\omega) \begin{bmatrix} v_1(j\omega) \\ u_2(j\omega) \end{bmatrix} \tag{28}$$

In such a case it is easy to see that the scaling factor cancels when considering the third condition of Llewelyn's stability criterion, but not when considering the third condition for passivity. Because the off diagonal terms are no longer equivalent there is now a potential of leaving the unit circle in figure 16, potentially violating the passivity constraint. It is not difficult to illustrate an example of when scaling the workspace causes the system to become active. If it is assumed the two–port haptic network has perfect transparency with

constant workspace transformation "n", equation (28) will take the following form.

$$\begin{bmatrix} u_1(j\omega) \\ -\hat{v}_2(j\omega) \end{bmatrix} = \begin{bmatrix} 0 & n^{-1} \\ -n & 0 \end{bmatrix} \begin{bmatrix} v_1(j\omega) \\ u_2(j\omega) \end{bmatrix} = P(j\omega) \begin{bmatrix} v_1(j\omega) \\ u_2(j\omega) \end{bmatrix} \tag{29}$$

Assuming zero initial energy, the required energy balance for passivity is

$$\int_{t_0}^{t} \left(u_1^T v_1 - u_2^T \hat{v}_2 \right) d\tau = \int_{t_0}^{t} \left(u_1^T v_1 - u_1^T n^T n v_1 \right) d\tau = \int_{t_0}^{t} \left(u_1^T \left(I - n^T n \right) v_1 \right) d\tau \geq 0 \tag{30}$$

It is evident "$n^T n$" must be less than or equal to identity to preserve passivity for any arbitrary combination of input and output, otherwise the system is required to generate energy for one of its two–ports. Again, the workspace transformation cancels when using the third condition of Llewelyn's stability criterion.

Unconditional stability or passivity can be tested once the haptic system, incorporating the effects of discrete sampling, virtual coupling, and the haptic device's dynamic equations, is formulated to fit in the two–port structure. Adams and Hannaford propose using this criterion to tune the virtual coupling so as to maximize both the system's transparency (maximum admittance) and stiffness (maximum impedance). Their insight on stability regarding the effects of the system's physical damping or sampling rate paralleled the findings of Colgate.[24, 2] Though they did not do it, Colgate's impedance virtual coupling stability criterion (equation (4)) can be recreated through a specif application of Llewelyn stability criterion to an impedance based haptic two–port network. The added benefit of Adams and Hannaford's work is that their results are not limited to a specific form of haptic interface or environment and their method can be applied to any linear, non-time varying haptic device. It is shown that the two–port network can be used to investigate all four implementation permutations, admittance / impedance interface with admittance / impedance environment.

3.3 Elements in Nonlinear Two–Port Networks

How does non-linearity affect the stability of the two–port network? Is there an equivalent stability condition to Llewelyn's, but incorporating provisions for nonlinear elements within

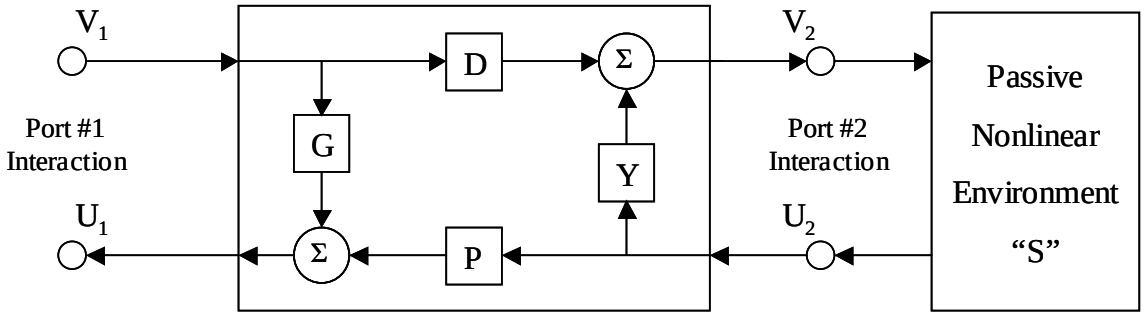

Figure 17: General Two–Port Impedance Device / Impedance Environment Network

the two–port network? Alternatively, what if the elements within the two–port network were linearized and then Llewelyn criterion applied?

Although equation (16) expressed a more general nonlinear two–port network, figure 17 shows a specific form of the two–port network for an impedance device and admittance environment. For the linear case, all of the internal elements G, D, P, and Y are linear dynamic mappings whose frequency transfer functions can be used with equation (19). Before considering non-linearity a brief explanation of each element and its physical meaning needs to be given. Element "D" represents the communication of measured velocity from the haptic device to the environment or slave device. Barring any saturation or dead zone, this element should remain fairly linear. Element "P" represents the communicated force from the slave device or environment to the haptic device and contains any force feedback servo control or actuator dynamics. Assuming the actuators are linear and that the force control structure set up by the designer is based on linear control theory, this element should remain linear. Element "G" represents the final closed loop, with respect to any force feedback servo control, impedance of the haptic device to the users velocity input. This element contains dynamics of the haptic device, which may contain non-linear components such as position dependent inertia properties, coriolis forces, and friction. Element "Y" represents the virtual coupling added by the system designer. Although this element may contain non-linear components if desired, the system designer can restrict its form to be linear. The remote device or virtual environment "S" may contain nonlinear components and is only

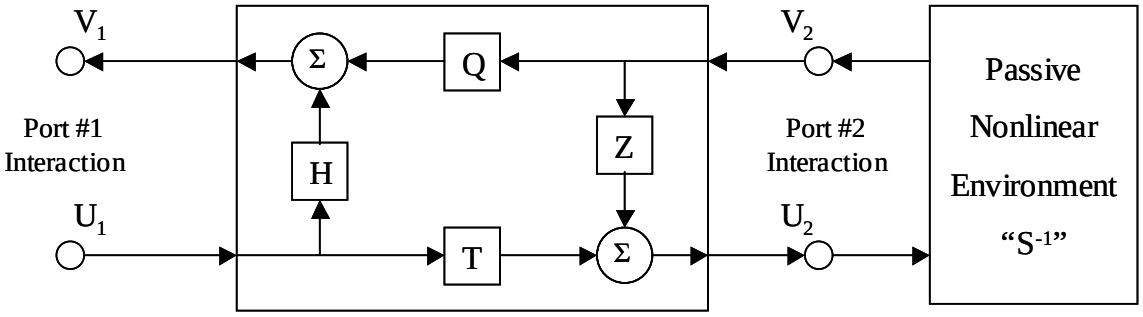

Figure 18: General Two–Port Admittance Device / Admittance Environment Network

assumed to be passive.

Similar to figure 17, the same can be done for the admittance device with an admittance environment as shown in figure 18. Like element "Y", element "Z" represents the virtual coupling and may contain non-linear elements if desired, though the system designer can restrict its form to be linear. Element "T" represents the communication of measured force to the remote environment / slave. Element "Q" represents the velocity feedback servo control on the haptic device. This element contains general dynamics associated with the haptic device's kinematics and inertia, which may contain non-linear components. Similarly, element "H" represents the final closed loop, with respect to any velocity feedback servo control, admittance of the haptic device to the users input force. Like element "Q", element "H" contains non-linearity's associated with the haptic devices dynamics. Again, the remote device or virtual environment "S^{-1}" may contain nonlinear components and is only assumed to be passive.

3.4 Linearization of Nonlinear Two–Port Networks

As previously mentioned, it is not uncommon for real robotic systems to incorporate non-linear elements, whether it is from the dynamics of the physical system or the control components. Assumption of linearity, though a convenient assumption, is not always a practical assumption. However, if a specific class of nonlinear passive systems are linearized it can be shown that the resulting linear system is also passive.[51]

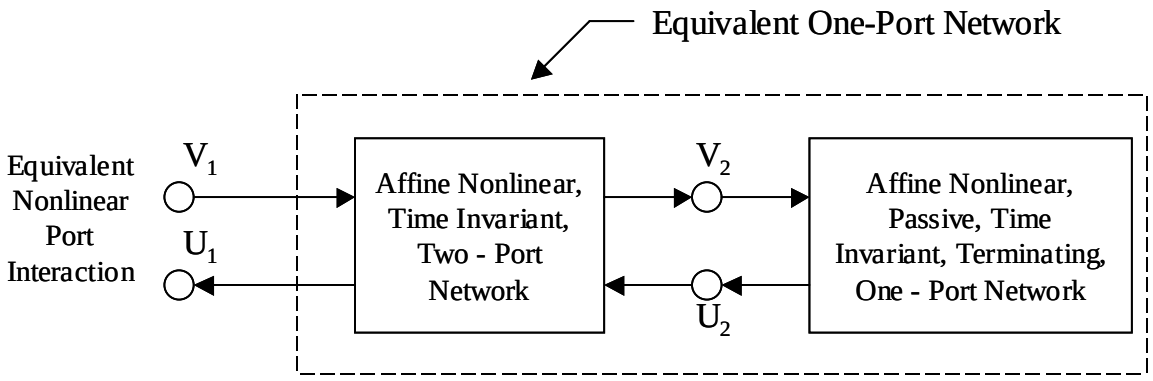

Figure 19: General Nonlinear Network

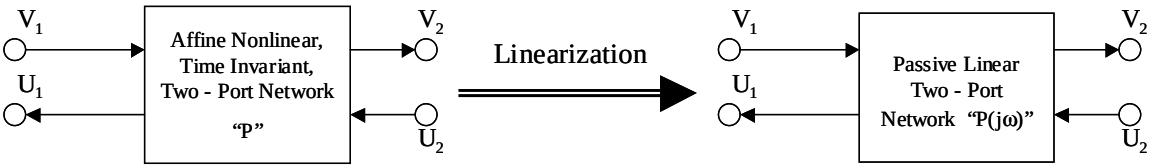

Figure 20: Linearization of an Affine Nonlinear Two–Port Network

For this to hold the nonlinear system must be affine with respect to the input and completely reachable. Using an impedance master with an admittance slave / environment, this requires the nonlinear two–port network to take the following form

$$\dot{X} = f(X) + G(X) \begin{bmatrix} V_1 \\ U_2 \end{bmatrix} \quad , \quad \begin{bmatrix} U_1 \\ V_2 \end{bmatrix} = d(X) + J(X) \begin{bmatrix} V_1 \\ U_2 \end{bmatrix} \tag{31}$$

with $f(\cdot)$, $G(\cdot)$, $d(\cdot)$, and $J(\cdot)$ being C^1 and the properties for existence and uniqueness of solutions are satisfied. Furthermore, it is assumed that $f(\cdot)$ has at least one equilibrium point $\bar{X}$ so that without loss of generality it can be assumed $f(\bar{X}) = 0$ and $d(\bar{X}) = 0$. This powerful property allows linear passivity conditions to be applied to the linearzed version of nonlinear models so as to guarantee passivity of the linearized model.

For the following discussion let H(s) be analogous to the following linear system

$$\begin{aligned} \dot{\tilde{X}} &= A\tilde{X} + B\tilde{U} \quad , \quad Y = C\tilde{X} + D\tilde{U} \\ \tilde{X} &= X - \bar{X} \quad , \quad \tilde{U} = U - \bar{U} \end{aligned} \tag{32}$$

where X, U, and Y are the general state, input, and output vectors respectively. For the

linearization of system (31), define

$$A = \frac{\partial f(X)}{\partial X}_{X=\bar{X}} \quad , \quad B = G(X)_{X=\bar{X}}$$
$$C = \frac{\partial d(X)}{\partial X}_{X=\bar{X}} \quad , \quad D = J(X)_{X=\bar{X}} \tag{33}$$

For example, the general nonlinear system shown in figure 19 characterized by system (31) can be linearized into the system shown in figure 15 and characterized by system (33). Of course, the linearized models are only valid with respect to a region near the equilibrium point, or within the region $f(\cdot)$ and $d(\cdot)$ are continuously differentiable (C^1), and may change as the system elements move around their workspace.

Furthermore, if the linearized system can be proven to be strictly positive real, or exponentially passive, then the linear system is also known to be asymptotically Lyapunov stable.[51] Asymptotic stability is synonymous with exponential stability for linear systems, which allows use of Lyapunov's indirect method to guarantee exponential stability of the nonlinear system within an operating range of its linearized equilibrium point. The only missing link is to relate Llewelyn's stability criterion with linear exponential passivity or strictly positive real (SPR) transfer functions. To do this the conditions, or frequency based criteria, for PR and SPR systems need to be touched upon.

Positive real, a condition for normal passivity of a linear system requires the linear transfer function H(s) to satisfy the following frequency based conditions.[51]

1. No element of $H(s)$ has a pole in $Re[s] > 0$
2. Hermition $He(H(j\omega)) \geq 0$ for all real ω, with $j\omega$ not a pole of any element of $H(s)$
3. If $j\hat{\omega}$ is a pole of any element of $H(s)$, it is at most a simple pole with a nonnegative definite Hermitian residue matrix $H_0 = \lim_{s \to j\hat{\omega}}(s - j\hat{\omega})H(s)$ when $\hat{\omega}$ is finite or $H_\infty = \lim_{\omega \to \infty} H(j\omega)/j\omega$ when $\hat{\omega}$ is infinite

Strictly positive real requires the existence of $\epsilon > 0$ such that $H(s - \epsilon)$ is positive real.

Strictly positive real is synonymous with exponential passivity or

$$\int_0^T e^{\varepsilon t} V^T(t) U(t) dt \geq 0 \quad , \qquad T = 0 \quad \& \quad \epsilon \geq 0 \tag{34}$$

Alternatively, H(s)is guaranteed to be SPR if it satisfies the following frequency based criterion.[51]

1. No element of $H(s)$ has a pole in $Re[s] > 0$
2. Hermition $He(H(j\omega)) > 0$ for all real ω
3. $D+D^T > 0$ or $D+D^T \geq 0$ and $\lim_{\omega \to \infty} \omega^2 Q^T He(H(j\omega))Q > 0$ for any $Q \in R^{m \times (m-q)}$ where $q = rank(D + D^T)$, such that $Q^T(D + D^T)Q = 0$

If $D + D^T = 0$ when testing condition 3 of the SPR criterion then one can set $Q = I_m$. The development of these PR and SPR conditions are fairly common and can be reviewed in many nonlinear texts, though the above supplied definitions came from Haddad and Chellaboina. Alternatively another way of stating condition 3 of the SPR criterion can be seen in Khalil to be the following[69]

3. Either $H(\infty)+H(\infty)^T > 0$ or $H(\infty)+H(\infty)^T \geq 0$ and $\lim_{\omega \to \infty} \omega^2 Q^T He(H(j\omega))Q > 0$ for any full rank $Q \in R^{m \times (m-q)}$ where $q = rank(H(\infty) + H(\infty)^T)$, such that $Q^T(H(\infty) + H(\infty)T)Q = 0$

Notice the second condition of the PR criterion, $He(H(j\omega)) \geq 0$, can not just simply be set as a strict inequality to show SPR of a continuous system. Although some nonlinear texts show this strict inequality as a sufficient condition, an example can easily be fabricated satisfying the strict inequality, but which is not SPR. The reason for this lies in the non finite range of ω, which can cause $He(H(j\omega))$ to approach, but not equal, "0" such that any $\epsilon > 0$ would cause $He(H(j\omega - \epsilon))$ to no longer be positive semi definite. Interesting enough, for a discrete system $G(z)$ the SPR condition can be simplified to the following two part criterion.[51]

1. No element of $G(z)$ has a pole in $|z| \geq 1$

2. Hermition $He(G(e^{j\omega})) > 0$ for all $\omega \in [0, 2\pi]$

It's worth noting that a strict inequality condition is a sufficient condition for the hermitian of a discrete system's frequency response. This can be attributed to discrete system SPR conditions being based on testing for positive realness of $G(z/\rho)$ with $\rho > 1$, which is a scaling of the complex variable "z", as opposed to continuous systems that test positive realness of $H(s - \varepsilon)$ with $\varepsilon > 0$, a shift of the the complex variable "s". Furthermore, discrete system's frequency response is defined only over a finite frequency range $[0, 2\pi]$, which adds bounds to the frequency range tested.

3.5 Application of Llewelyn's Stability Criterion to Nonlinear Two–Port Networks

In order to use Llewelyn's stability criterion to guarantee passivity of the nonlinear system, extra SPR conditions must be applied. The first step is to linearize the non linear two–port network so that it may be represented near an equilibrium point with the form illustrated in equation (19). While the first modification to the Llewelyn stability criterion (equation (24)) is to require $p_{11}(j\omega)$ and $p_{22}(j\omega)$ to be SPR through testing of the aforementioned SPR conditions, satisfying the third Llewelyn stability condition with a strict inequality does not guarantee a continuous network is SPR when interfaced with any passive terminating one–port. Alternatively, if the two–port network is discrete and does not contain any poles outside the unit circle, then the Llewelyn stability criterion can be used to test for SPR behavior when interfaced with any passive terminating one–port by simply applying strict inequalities to the stability conditions and testing over the discrete networks applicable frequency range, as illustrated by

$$\begin{aligned} \mathrm{Re}(p_{11}) > 0 \quad &, \quad \mathrm{Re}(p_{22}) > 0 \\ 2\mathrm{Re}(p_{11})\mathrm{Re}(p_{22}) \quad &> \quad |p_{12}p_{21}| + \mathrm{Re}(p_{12}p_{21}), \quad \omega \in [0, 2\pi] \end{aligned} \tag{35}$$

Reviewing the physical meaning of SPR and what SPR conditions represent lends an intuitive approach for using Llewelyn's stability criterion to test for SPR properties when

interfacing linearized continuous two–port networks with passive terminating one–port networks. Conditions for SPR confirm allowable model offset ($\epsilon > 0$) for a system to remain PR, guaranteeing the system is dissipative. This breadth is what allows use of Lyapunov's indirect method to infer nonlinear stability from the linearized models stability properties; alowing leeway for the effects of higher order terms dropped in linearization. Though not as eloquent, a practical implementation for continuous systems is to satisfy the soft inequalities of Llewelyn's stability criterion against predefined positive offset constants.

$$\begin{aligned} \mathrm{Re}(p_{11}) \geq \varepsilon_1 \quad &, \quad \mathrm{Re}(p_{22}) \geq \varepsilon_2 \\ 2\mathrm{Re}(p_{11})\mathrm{Re}(p_{22}) \quad &\geq \quad |p_{12}p_{21}| + \mathrm{Re}(p_{12}p_{21}) + \varepsilon_3 \\ \text{for real constants } \varepsilon_i > 0 \quad &\& \quad \forall \omega \geq 0 \end{aligned} \tag{36}$$

This ad hoc method could be thought of as a predefined "positive real margin".

As noted earlier, linearization is only valid within an operating range of the equilibrium point and the system parameters are likely to change as the system moves about its workspace. For this reason it may be necessary to look at various configurations of the nonlinear two–port network and tune the control system properties for various equilibrium points to satisfy the SPR Llewelyn based stability criterion being used. Another important property of the system mentioned earlier is that $f(\cdot)$ is continuously differentiable (C^1).

CHAPTER 4

FORMULATION OF HAPTIC TWO-PORTS

As previously outlined, two–port networks provide a convenient compact way to modularly package haptic systems and their control architecture. This chapter outlines how to construct such networks for a force controlled, back–drivable haptic device. Stability conditions based on Llewelyn's criterion and the passivity criterion for the specific haptic networks is presented. Equations for impedance and admittance limits for these networks are presented so as to better understand the effects of the individual network components. For future discussion the nomenclature outlined in table 3 will be used for naming the two–port networks. It's worth noting that the A/I network is the traditional admittance causal two–port network while the I/A network is the traditional impedance causal two–port network.

4.1 Frequency Analysis of Hybrid Continuous & Discrete Networks

Traditional discrete closed loop control system analysis only considers the analog component's response to the digital controller's action, allowing discrete equivalents of the analog system to be used in discrete controller design. Haptic two–port networks contain both discrete and analog loops / signal flows in its structure, including signal loops that are purely

Table 3: Haptic Two–Port Naming Nomenclature

Two-Port Name	Causality Seen by the User	Causality Seen by the Environment
I / A	Impedance	Admittance
A / I	Admittance	Impedance
I / I	Impedance	Impedance
A / A	Admittance	Admittance

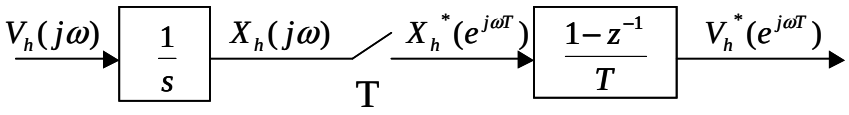

Figure 21: Block Diagram for Discrete Estimation of Velocity

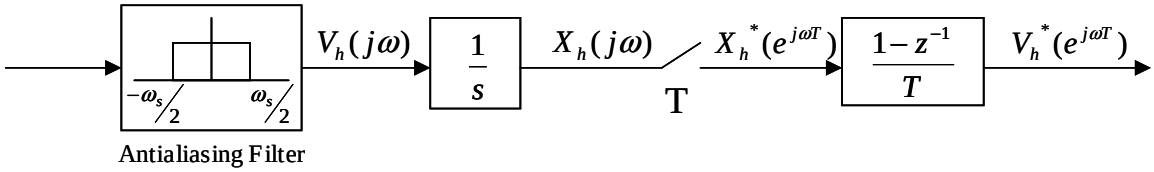

Figure 22: Block Diagram for Discrete Estimation of Velocity (with antialiasing filter)

analog. Estimating the analog loop's input/output transfer functions with discrete approximations, such as bilinear transformation or backwards difference transformation, will distort their modeled frequency response. Distorting the frequency response of the analog signal paths will lead to improper model estimation, distorting the two–port network's frequency response which passivity design and Llewelyn's stability criterion rely on. Furthermore, many analog elements in a haptic network are subject to both analog signals and signals from the discrete controller's zero–order hold, therefore their frequency transfer function is required for both analog and discrete loops. Assuming limited analog signal bandwidth and sufficient sampling rate allows the analysis to be completed in the continuous frequency domain with both original analog frequency functions and the proper frequency equations for discrete components, preserving the frequency response of the analog and discrete signal paths. These assumptions are not trivial and their validity needs to be considered when initially structuring the haptic network.

The system in figure 21 will be used to demonstrate the assumptions required to analyze discrete and analog components together in the frequency domain while developing one of the components used in the following haptic two–port networks. Formulation of the haptic two–port networks utilize velocity and force, the physical power variables, as the communicated parameters through its ports, but most digitally controlled devices measure position and discretely calculate velocity. Figure 21 represents analog integration of the device's velocity to get analog position, sampling the position with sampling period T, and then

numerically differentiating the sampled position with a backwards difference differentiator. The Fourier transform of the discretely calculated velocity can be represented as

$$V_h^*(e^{j\omega T}) = \frac{1}{j\omega}\left(\frac{e^{j\omega T}-1}{e^{j\omega T}}\right)\left(\sum_{n=-\infty}^{\infty} V_h(j(\omega - n\omega_s))\right) \tag{37}$$

where $s = j\omega$, $z = e^{j\omega T}$, the discrete system's sampling period is T, and ω_s is the sampling frequency $2\pi/T$. The traditional $1/T$ scaling factor was removed from equation (37) and included in the zero–order hold's equation (41) so that both the sampler and zero–order hold each have normalized gains. Discretely sampling an analog signal causes aliasing of its components above the Nyquist frequency, as represented by the summation in equation (37). If, as illustrated in figure 22, an antialiasing filter is added to the diagram so that the analog velocity entering the haptic network's port does not contain components above the Nyquist frequency, then

$$V_h(j\omega) = 0 \quad , \quad \forall\omega > {}^{\omega_s}\!/_2 \tag{38}$$

and equation 37 can be simplified to

$$\frac{V_h^*(e^{j\omega T})}{V_h(j\omega)} = D(j\omega) = \frac{e^{j\omega T}-1}{(j\omega T)e^{j\omega T}} \quad , \quad \forall\omega < {}^{\omega_s}\!/_2 \tag{39}$$

Adding an antialiasing filter allows derivation of the frequency transfer function $D(j\omega)$ for modeling signal distortion caused by discretely estimating device velocity through sampling device position and discretely differentiating. Physically adding ideal antialiasing filters isn't practical because the ideal antialiasing filter is a non causal function. Rather, the antialiasing filter represents the assumption that signals entering the haptic network do not contain prominent components above the Nyquist frequency, which is a fundamental consideration when selecting sampling rate. Considering the sampling rate capabilities of modern digital control systems and that haptic device velocities and human applied forces are physically band limited, it is safe to assume a sufficient sampling frequency can be chosen for haptic systems control. Even with high sampling rates it is advisable to condition analog signals with analog low pass filters to minimize noise and prevent signal aliasing, but such filters need to be included in the haptic network construction so as to account for their phase distortion on the signal.

4.2 General Elements of Haptic Two–Port Networks

All of the networks use programmed virtual coupling to modify the interaction of the haptic device with the virtual or slave environment. Said virtual coupling's primary purpose is to design stability into the network for when interfaced with arbitrary passive environments. Future sections will outline how virtual coupling is used to do this, while future chapters will go into more detail on models for virtual coupling and methods for selecting actual virtual coupling. In Adams and Hannaford's work they too assume a haptic device that is fundamentally controlled by force generated from actuators. Besides virtual coupling, when formulating the A/I two–port network digital velocity feedback control is used to turn the haptic device into a velocity source, which gives an additional control parameter to manipulate in the two–port system. Having two parameters to manipulate, the velocity feedback controller and virtual coupling, the A/I network is more flexible to tune than the I/A network; which only allows manipulation of virtual coupling. If the I/A network is to be a true dual of the A/I structure, there should be two parameters in the impedance formulation for the designer to manipulate. By utilizing force feedback in the I/A formulation, providing an additional control loop in the structure, this second parameter is provided. Although Salcudean and Hastrudi-Zaad consider local force feedback in their two–port teleoperation network, they do not consider the effects of digital control and they limit all force gains to scalar values, which limits the control structure.[58]

Two–port network formulated in the following sections contain a few common elements. Unlike continuous systems, implementation of a digital control algorithm is a sequential operation; control outputs can not be calculated from simultaneous measurements without a small delay. The control algorithm may execute in the following order; output the new (stored) command signal, read the sensors, calculate the new command signal, and store the new command signal until it is implemented at the beginning of the next control iteration. Alternatively the control algorithm can read the sensors, calculate the new command signal, output the new command signal, then wait for the next control iteration. The first method guarantees a hard-set interval between command signal updates, but introduces a pure time

delay of one sample period. The second method allows for slight variance in the period between command signal updates, depending on the time it takes to measure, calculated, and send; but this delay will be less than a full sample period. This delay, whether it is a full sample period or shorter, will be referred to as inter-control delay. In construction of the two–port networks the inter-control delay will be characterized by "N", the ratio factor of sampling period "T" to inter-control delay, through the use of the transfer function

$$\text{Delay} = e^{-Ts/N} \tag{40}$$

Furthermore, dynamic terms representing the dynamics of the force actuator's amplifier / power supply ($L(S)$) are added to the models. In an experimental system these dynamics may be found to be negligible and assumed to approach unity, but this will be discussed later. Often force sensing hardware incorporates low pass filters to eliminate unwanted noise and prevent aliasing of signals. Such a filter will be represented by $M(s)$ in the following block diagrams. Based on these points and utilizing the following continuous definition for the Zero Order Hold,

$$ZOH(s) = \frac{1 - e^{-Ts}}{Ts} \tag{41}$$

the impedance and admittance networks can be formed in the following sections. Discrete signals are represented by "*" while F_h & V_h represent the human's hand's force & velocity respectively and Fe^* & Ve^* represent the simulated or discretely measured (sampled) environment's force & velocity respectively. Dynamics of the physical haptic device are represented by its admittance $Y_d(s)$ or its impedance $Z_d(s)$.

4.3 Admittance / Impedance Two–Port Network

Figure 23 represents the two–port haptic A/I network for a force controlled haptic device. The network accepts force input from the operator and discretely communicates this force to the interfaced (simulated) environment. Velocities reflected back to the operator are based on velocities generated by the environment and the velocity feedback controller. Virtual

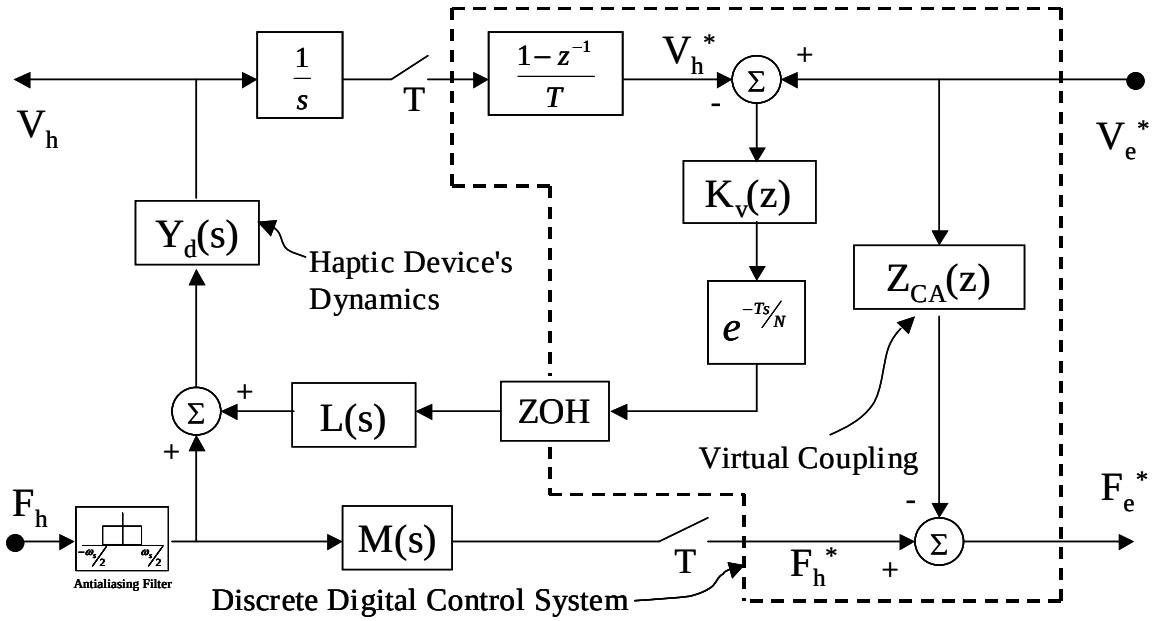

Figure 23: A/I Two–Port Network Block Diagram

coupling is used to modify the force sent to the environment based on sampled environment velocities, while dynamics of the haptic device are compensated through the velocity feedback controller. The two–port admittance network can be described by the following frequency domain response.

$$\begin{bmatrix} V_h(j\omega) \\ F_e^*(e^{j\omega T}) \end{bmatrix} = \begin{bmatrix} H(j\omega) & -Q(j\omega) \\ M(j\omega) & Z_{CA}(e^{j\omega T}) \end{bmatrix} \begin{bmatrix} F_h(j\omega) \\ -V_e^*(e^{j\omega T}) \end{bmatrix} \quad , \quad 0 \leq \omega \leq {}^{\omega_s}/_2 \tag{42}$$

Where,

$$H(j\omega) = \frac{1}{Z_d(j\omega) + D(j\omega)K_v(e^{j\omega T})e^{-j\omega T/N}ZOH(j\omega)L(j\omega)} \tag{43}$$

$$Q(j\omega) = \frac{K_v(e^{j\omega T})e^{-j\omega T/N}ZOH(j\omega)L(j\omega)}{Z_d(j\omega) + D(j\omega)K_v(e^{j\omega T})e^{-j\omega T/N}ZOH(j\omega)L(j\omega)} \tag{44}$$

Llewelyn's stability condition results in the following condition for the A/I network.

$$\mathrm{Re}\left(Z_{CA}(e^{j\omega T})\right) \geq \left[\frac{1-\cos\left(\angle\left[Q(j\omega)M(j\omega)\right]\right)}{2\mathrm{Re}\left(H(j\omega)\right)}\right]\left|Q(j\omega)M(j\omega)\right| \quad , \quad 0 \leq \omega \leq {}^{\omega_s}/_2 \tag{45}$$

Effects of numerically differentiating to derive velocity, dynamics of the power supply / amplifiers, inter-control delay, and zero order hold are now internal to $Q(j\omega)$ and $H(j\omega)$. Once the velocity feedback parameters are chosen, the network designer must tune the virtual coupling to satisfy equation (45). By formulating the haptic network into the A/I form, the stability condition is independent of the virtual coupling; that is the values which the real part of the virtual coupling must be greater than do not change when the coupling itself is changed. In contrast to equation (45), in order for the network to be passive it must satisfy the following condition.

$$\mathrm{Re}\left(Z_{CA}(e^{j\omega T})\right) \geq \frac{|M(j\omega) - Q(j\omega)^*|^2}{2\mathrm{Re}\left(H(j\omega)\right)} \tag{46}$$

To investigate the admittance range of the device, one can consider that the environment has a linear velocity / force relationship defined by

$$V_e^*(e^{j\omega T}) = Y_e(e^{j\omega T})F_e^*(e^{j\omega T}) \tag{47}$$

where Y_e is the environment's admittance and its inverse Z_e is the environment's equivalent impedance. Using this relationship with the previous two–port model results in the following equivalent admittance relationship as experienced by the human.

$$V_h(j\omega) = \left[H(j\omega) + \frac{Q(j\omega)M(j\omega)}{Z_e(e^{j\omega T}) + Z_{CA}(e^{j\omega T})}\right] F_h(j\omega) \tag{48}$$

To consider the haptic system's transparency $|Y_e|$ should be set to ∞ ($|Z_e|$ set to zero), simplifying equation (48) into the following maximum admittance relationships

$$V_h(j\omega) = \left[H(j\omega) + \frac{Q(j\omega)M(j\omega)}{Z_{CA}(e^{j\omega T})}\right] F_h(j\omega) \tag{49}$$

Alternatively, to consider the system's maximum stiffness, or minimum admittance, $|Y_e|$ should be assumed to be zero ($|Z_e|$ assumed to be ∞), simplifying equation (48) into the following minimum admittance relationships

$$V_h(j\omega) = \left[H(j\omega)\right] F_h(j\omega) \tag{50}$$

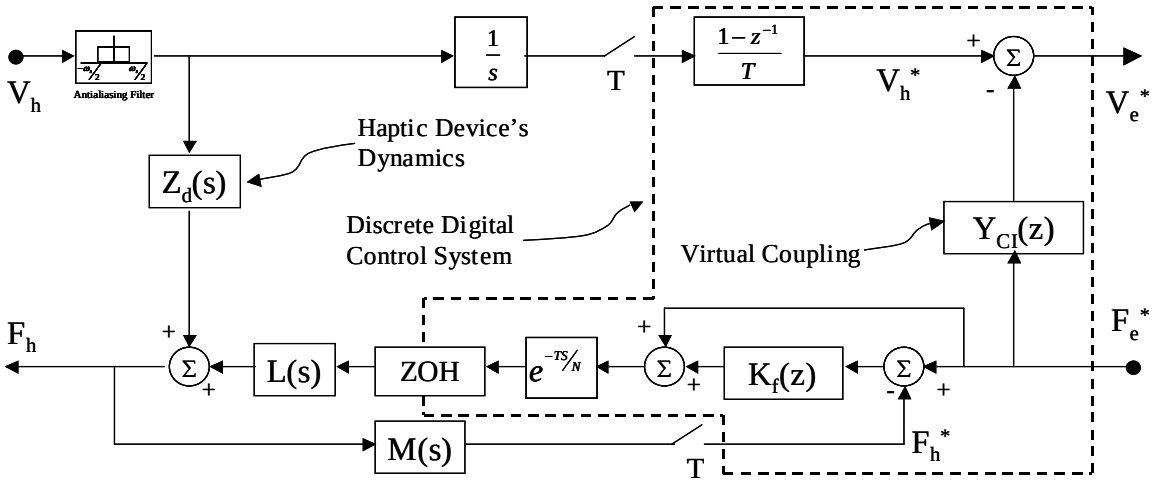

Figure 24: I/A Two–Port Network Block Diagram

From these relationships it can be seen that the minimum admittance and admittance width (Y width) can be characterized by

$$Y_{\min} = H(j\omega) \quad , \quad Y_{width} = \frac{Q(j\omega)M(j\omega)}{Z_{CA}(e^{j\omega T})} \tag{51}$$

From these relationships it is apparent that the admittance width (Y width) of the network is maximized by maximizing $Q(j\omega)$ and minimizing $Z_{CA}(e^{j\omega T})$ and that $Q(j\omega)$ is maximized, or driven closer to unity, by maximizing $K_v(e^{j\omega T})$. On the other end of the spectrum, minimum admittance is achieved by minimizing $H(j\omega)$; which is achieved through maximizing $Z_d(j\omega)$ and $K_v(e^{j\omega T})$. Referring to equation (45), increasing $K_v(e^{j\omega T})$ to lower the minimum achievable admittance and provide stronger feedback control of the haptic device's output to the human results in an increased required $\mathrm{Re}(Z_{CA}(e^{j\omega T}))$; which in return lowers the Y width. This presents the network designer with a two-parameter trade off design problem that must be balanced.

4.4 Impedance / Admittance Two–Port Network

Figure 24 represents the two–port haptic I/A network. The network accepts velocity input from the operator and discretely communicates this velocity to the interfaced (or simulated)

environment. Forces reflected back to the operator should be those generated by the environment, while velocities sent to the environment are a combination of the haptic device's calculated velocity and the compliance effects of the virtual coupling. Dynamics of the haptic device show up as additional reflected force to the operator, over that commanded by the environment. The two–port impedance network can be described by the following frequency mapping

$$\begin{bmatrix} F_h(j\omega) \\ -V_e^*(e^{j\omega T}) \end{bmatrix} = \begin{bmatrix} G(j\omega) & P(j\omega) \\ -D(j\omega) & Y_{CI}(e^{j\omega T}) \end{bmatrix} \begin{bmatrix} V_h(j\omega) \\ F_e^*(e^{j\omega T}) \end{bmatrix} \quad , \quad 0 \leq \omega \leq \omega_s/2 \tag{52}$$

where,

$$G(j\omega) = \frac{Z_d(j\omega)}{1 + K_f(e^{j\omega T})e^{-j\omega T/N} ZOH(j\omega)L(j\omega)M(j\omega)} \tag{53}$$

$$P(j\omega) = \frac{\left(1 + K_f(e^{j\omega T})\right) e^{-j\omega T/N} ZOH(j\omega)L(j\omega)}{1 + K_f(e^{j\omega T})e^{-j\omega T/N} ZOH(j\omega)L(j\omega)M(j\omega)} \tag{54}$$

To better understand the effect of each term in the two–port mapping when trying to satisfy Llewelyn's stability criterion, the following conditions for absolute stability of the I/A network can be formulated.

$$\mathrm{Re}\left(Y_{CI}(e^{j\omega T})\right) \geq \left[\frac{1 - \cos\left(\angle\left[D(j\omega)P(j\omega)\right]\right)}{2\mathrm{Re}\left(G(j\omega)\right)}\right] |D(j\omega)P(j\omega)| \tag{55}$$

This relationship shows that numerically differentiating position adds to the effect of the cosine term, or increases the phase loss, requiring greater values for $\mathrm{Re}(Y_{CI}(e^{j\omega T}))$ than without the effects of numerically differentiating. It will be shown later that the trade off between stiffening the force feedback control loop, increasing transparency and Z width, and having to relax the virtual coupling, decreasing Z width, is something the designer must balance. Similar to the A/I network, by formulating the haptic network into the I/A form, the stability condition is independent of the virtual coupling; that is the values which the real part of the virtual coupling must be greater than do not change when the coupling itself is changed. In contrast to equation (55), in order for the network to be passive, it

must satisfy the following condition.

$$\mathrm{Re}\left(Y_{CI}(e^{j\omega T})\right) \geq \frac{|P(j\omega) - D(j\omega)^*|^2}{2\mathrm{Re}\left(G(j\omega)\right)} \tag{56}$$

Similarly to what was previously done with the A/I network, to investigate the impedance range of the device one can consider that if the environment has a linear force / velocity relationship defined by

$$F_e^*(e^{j\omega T}) = Z_e(e^{j\omega T})V_e^*(e^{j\omega T}) \tag{57}$$

where Z_e and Y_e are reciprocals of each other, then the I/A two–port model results in the following equivalent impedance relationship to the human.

$$F_h(j\omega) = \left[G(j\omega) + \frac{P(j\omega)D(j\omega)}{Y_e(e^{j\omega T}) + Y_{CI}(e^{j\omega T})}\right] V_h(j\omega) \tag{58}$$

To determine the haptic system's transparency, $|Z_e|$ should be set to 0 ($|Y_e|$ set to ∞); simplifying equation (58)into the following minimum impedance relationship

$$F_h(j\omega) = \left[G(j\omega)\right] V_h(j\omega) \tag{59}$$

Alternatively, to find the system's maximum stiffness $|Z_e|$ should be set to ∞ ($|Y_e|$ set to 0); simplifying equations (58) into the following maximum impedance relationship

$$F_h(j\omega) = \left[G(j\omega) + \frac{P(j\omega)D(j\omega)}{Y_{CI}(e^{j\omega T})}\right] V_h(j\omega) \tag{60}$$

From these relationships it can be seen that the minimum impedance and impedance width (Z width) for the impedance structure is

$$Z_{\min} = G(j\omega) \quad , \quad Z_{width} = \frac{P(j\omega)D(j\omega)}{Y_{CI}(e^{j\omega T})} \tag{61}$$

As expected, the Z width in the impedance network is maximized by maximizing $P(j\omega)$ and minimizing $Y_{CI}(e^{j\omega T})$. To maximize $P(j\omega)$, or drive it closer to unity, the force control

loop $K_f(e^{j\omega T})$ needs to be maximized. Transparency of the device can be minimized by minimizing $G(j\omega)$, which is minimized by either minimizing $Z_d(j\omega)$ or maximizing $K_f(e^{j\omega T})$. Another relationship that can be deduced is that larger values of $K_f(e^{j\omega T})$, providing stiffer feedback control of the haptic device's output to the human, results in driving the magnitude of $P(j\omega)$ closer to unity and the magnitude of $G(j\omega)$ to zero; which requires larger values of $\mathrm{Re}(Y_{CI}(e^{j\omega T}))$. As with the A/I network, this presents the network designer with a two-parameter design problem that must be balanced based on the objective at hand.

4.5 Scaling for Mismatched Workspaces

Often the input and output of a haptic device must be scaled appropriately to match the virtual environment model or slave robot's workspace. As outlined in a previous chapter, if this scaling is done within the two–port network it will cause an otherwise passive network to become non-passive, or active. This should come as no surprise; energy must be generated in order to amplify the signals. For example, assume the environment variables are scaled by "n" such that

$$F_e = n\hat{F}_e \quad , \quad V_e = n\hat{V}_e \tag{62}$$

then the A/I and I/A two–port networks respectively become

$$\begin{bmatrix} V_h(j\omega) \\ \hat{F}_e^*(e^{j\omega T}) \end{bmatrix} = \begin{bmatrix} H(j\omega) & -Q(j\omega)/n \\ nM(j\omega) & Z_{ca}(e^{j\omega T}) \end{bmatrix} \begin{bmatrix} F_h(j\omega) \\ -\hat{V}_e^*(e^{j\omega T}) \end{bmatrix} \tag{63}$$

$$\begin{bmatrix} F_h(j\omega) \\ -\hat{V}_e^*(e^{j\omega T}) \end{bmatrix} = \begin{bmatrix} G(j\omega) & P(j\omega)/n \\ -nD(j\omega) & Y_{ci}(e^{j\omega T}) \end{bmatrix} \begin{bmatrix} V_h(j\omega) \\ \hat{F}_e^*(e^{j\omega T}) \end{bmatrix} \tag{64}$$

As expected, the scaling term "n" cancels itself in the Llewelyn Stability criterion (equation (45) & (55)), but not in the passivity criterion (equation (46) & (56)). Using the Llewelyn stability criterion instead of the passivity condition allows the haptic two–port to be independently tuned and universally used with environments or slaves of arbitrary size.

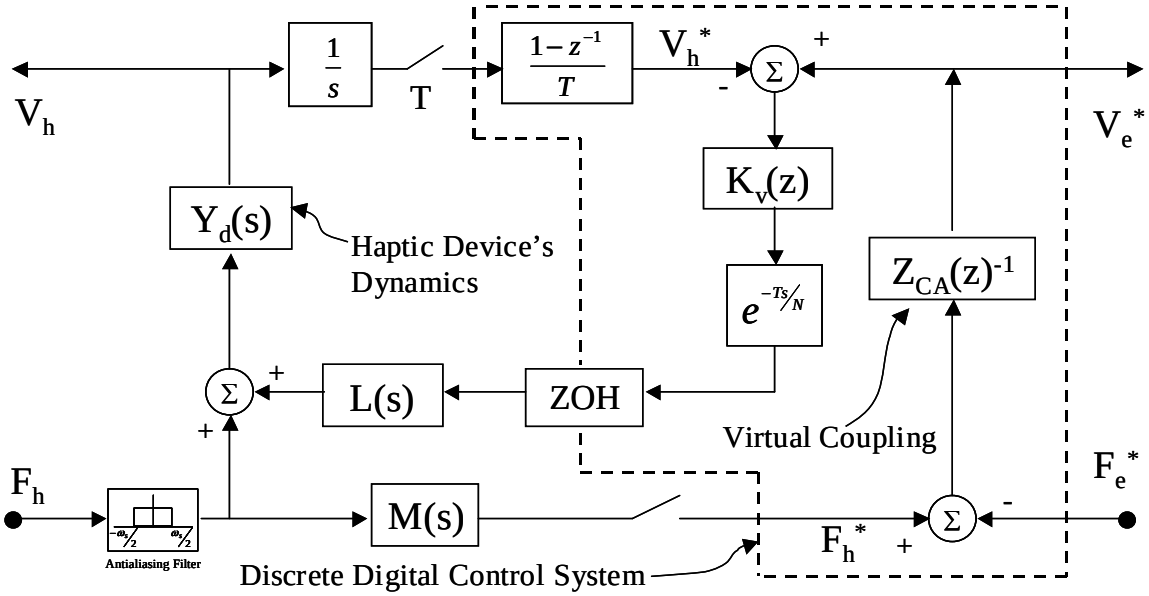

Figure 25: A/A Two–Port Network Block Diagram

4.6 A/A and I/I Haptic Two–Port Networks

Until now only A/I and I/A versions of the two–port haptic networks have been addressed. As mentioned previously, the attraction of two–port networks is that they can be used to implement any causality combination of the input / output variables. Up until now the networks' ports have served to match compatible terminating one–port networks, that is to interface an impedance human with an admittance environment or visa versa. Haptic networks may also be used to connect two one–port terminating ports with the same impedance or admittance causality, such as an impedance acting human with an impedance environment or an admittance acting human with an admittance environment. Two such forms are the I/I and A/A two–port networks. When forming these networks it can be seen that properties and virtual couplings from previous I/A and A/I networks apply. Figure 25 illustrates the A/I haptic network modified to be a A/A network.

As expected the A/A network highly resembles the A/I model, except the virtual coupling flow is reversed. If the same parameters are applied to the A/A network as used in

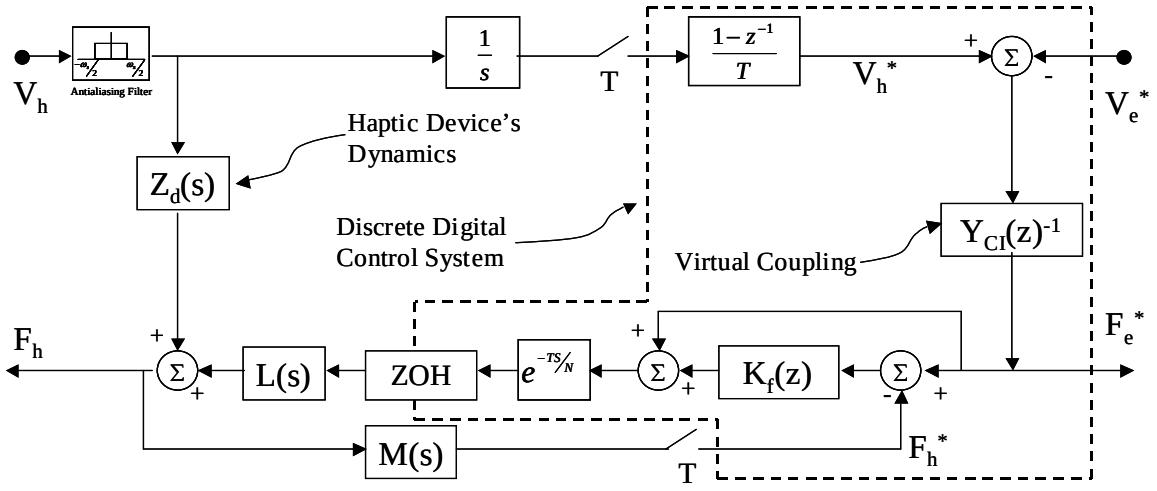

Figure 26: I/I Two–Port Network Block Diagram

the A/I network, the two–port mapping is

$$\begin{bmatrix} V_h(j\omega) \\ -V_e^*(e^{j\omega T}) \end{bmatrix} = \begin{bmatrix} H(j\omega) + \frac{Q(j\omega)M(j\omega)}{Z_{CA}(e^{j\omega T})} & -\frac{Q(j\omega)}{Z_{CA}(e^{j\omega T})} \\ -\frac{M(j\omega)}{Z_{CA}(e^{j\omega T})} & \frac{1}{Z_{CA}(e^{j\omega T})} \end{bmatrix} \begin{bmatrix} F_h(j\omega) \\ F_e^*(e^{j\omega T}) \end{bmatrix} \tag{65}$$

Much as the A/A model highly resembles the A/I model with the virtual coupling flow reversed, the I/I network can be formed by reversing the flow through the I/A network's virtual coupling. Again, if the same parameters used in the I/A network are used in the I/I network the two–port mapping is

$$\begin{bmatrix} F_h(j\omega) \\ F_e^*(e^{j\omega T}) \end{bmatrix} = \begin{bmatrix} G(j\omega) + \frac{D(j\omega)P(j\omega)}{Y_{CI}(e^{j\omega T})} & \frac{P(j\omega)}{Y_{CI}(e^{j\omega T})} \\ \frac{D(j\omega)}{Y_{CI}(e^{j\omega T})} & \frac{P(j\omega)}{Y_{CI}(e^{j\omega T})} \end{bmatrix} \begin{bmatrix} V_h(j\omega) \\ -V_e^*(e^{j\omega T}) \end{bmatrix} \tag{66}$$

Forming the Llewelyn stability conditions from equations (65) and (66) result in inequality limits that change with virtual coupling, unlike conditions for the A/I and I/A networks that have limits which are invariant to changing the virtual coupling. Having the inequality limit independent of the parameter being tuned is a more convenient form. It can be easily shown that if the A/I network satisfies Llewelyn's stability, so will the A/A network that utilizes the same parameters. Similarly, if the I/A network satisfies Llewelyn

stability criterion, the I/I network using the same parameters will as well. This allows the control problem to be formulated into the more convenient A/I or I/A form, even if it is implemented in the A/A or I/I form (respectively).

Future sections dealing with network tuning, effects of models for human dynamic limits, and varying device parameters will be with respect to the A/I and I/A networks. Because the tuning of the A/A and I/I networks can be reformulated into the A/I and I/A tuning problem, conclusions and results based on the A/I and I/A analysis may be applied.

CHAPTER 5

TUNING OF VIRTUAL COUPLING

As previously outlined, construction of haptic two–port networks requires tuning of two transfer functions, the force controller and virtual coupling for the I/A networks and the velocity controller and virtual coupling for the A/I networks. How should these two transfer functions of a network be tuned? Ideally the virtual coupling, Y_{CI} and Z_{CA}, should be as small as possible and the feedback controllers, K_v and K_f, should be as stiff as allowable. Furthermore, these transfer functions must be chosen so as to satisfy the stability criteria. It was also previously commented that stiffer K_v and K_f lead to larger required couplings.

The following discussion will show some insight on how to select these transfer functions through selection of virtual coupling models and utilizing the duality between the A/I and I/A networks. Human limit models previously touched upon in chapter 2 will also be incorporated into the two–port networks to show how tuning is affected. Finally, the two parameter tuning problem, virtual coupling and feedback controller, will be presented as a nonlinear constrained optimal tuning problem.

5.1 Selection of Virtual Coupling Form

Tuning of the two–port networks, specifically the virtual coupling, is not necessarily straightforward. What form should the virtual coupling take and what parameters should be used are questions critical to the performance of the haptic network. In the past most have picked specific intuitive physical models for the virtual coupling, but is there any benefit to extending the models into less intuitive forms?

In the past others have chosen virtual coupling for the A/I network to mimic a virtual

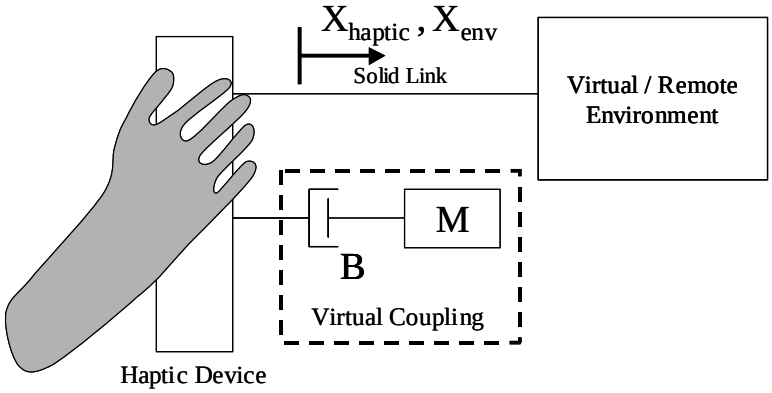

Figure 27: A/I Network Virtual Coupling

damper and mass in parallel with the device's handle, as illustrated in figure 27. If M_c and B_c were defined as M/T and B respectively, with T being the discrete controllers sample period, such coupling can be modeled discretely with backwards difference differentiation as

$$F_h^* - F_e^* = Z_{CA} V_e^* = \left(\frac{M_c B_c (z-1)}{(M_c + B_c)z - M_c} \right) V_e^* \tag{67}$$

or

$$F_h^* - F_e^* = Z_{CA} V_e^* = \left(\frac{z-1}{K_{cc}(z - \alpha_c)} \right) V_e^* \tag{68}$$

If a spring were included in the virtual coupling and K_c was defined as $K \times T$, the relationship would take the form of

$$F_h^* - F_e^* = Z_{CA} V_e^* = \left(\frac{M_c((B_c + K_c)z - B_c)(z-1)}{(M_c + B_c + K_c)z^2 - (2M_c + B_c)z + M_c} \right) V_e^* \tag{69}$$

or if the the coupling's zero was placed independent of the poles

$$F_h^* - F_e^* = Z_{CA} V_e^* = \left(\frac{(z - x_4)(z-1)}{x_1(z^2 - x_2 z + x_3)} \right) V_e^* \tag{70}$$

This second order form of virtual coupling may be extended into an even more universal form, such as

$$F_h^* - F_e^* = Z_{CA} V_e^* = \left(\frac{z^2 - x_4 z + x_5}{x_1(z^2 - x_2 z + x_3)} \right) V_e^* \tag{71}$$

Alternatively, if bilinear, or Tustin, conversion was used to convert the virtual coupling into discrete form it would take the following forms

$$F_h^* - F_e^* = Z_{CA} V_e^* = \left(\frac{2M_c B_c (z-1)}{(2M_c + B_c)z - (2M_c - B_c)} \right) V_e^* \tag{72}$$

or with a virtual spring,

$$Z_{CA} V_e^* = \left(\frac{2M_c((2B_c + K_c)z - (2B_c - K))(z-1)}{(4M_c + 2B_c + K_c)z^2 - (8M_c - 2K_c)z + (4M_c - 2B_c + K_c)} \right) V_e^* \tag{73}$$

Bilinear transformation leads to the same effective form for the mass-damper model as backwards difference transformation (equations (67), (72), & (68)), but leads to a slightly different form for the mass-spring-damper model (equations (69) & (73)); although both mass-spring-damper models can be described by the more general forms of equation (70) and (71) These more general forms relax the association between placement of the poles and zeros, though (70) still requires a zero at $z = 1$.

When used in the A/I network this virtual coupling essentially acts to detract from the force applied to the environment by the human. Alternatively when used in an A/A environment it serves to translate a difference in haptic force and environment force to a common applied haptic & desired environment velocity. Increasing M_c and B_c will increase the perceived inertia by the user and decrease the kick of the device when subjected to an "impulse" from the environment. This corresponds to the effects of coupling on admittance limits as outlined in chapter 4.

Similarly, virtual coupling for the I/A network has primarily taken the form of a spring and damper, as illustrated in Figure 28. If K_c and B_c were defined as $K \times T$ and B respectively, with T being the discrete controllers sample period, such coupling can be modeled discretely with backwards difference differentiation as

$$V_h^* - V_e^* = Y_{CI} F_e^* = \left(\frac{1}{B_c + {}^{K_c}/_{1 - z^{-1}}} \right) F_e^* = \left(\frac{z-1}{(B_c + K_c)z - B_c} \right) F_e^* \tag{74}$$

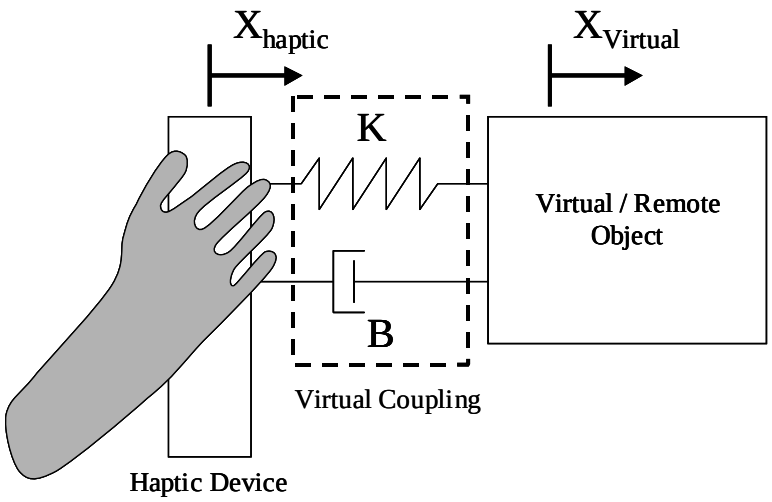

Figure 28: I/A Network Virtual Coupling

or

$$V_h^* - V_e^* = Y_{CI}F_e^* = \left(\frac{z-1}{K_{cc}(z-\alpha_c)}\right)F_e^* \tag{75}$$

Alternatively, if a pseudo virtual mass were included in the virtual coupling and M_c was defined as M/T, it may take the form of

$$V_h^* - V_e^* = Y_{CI}F_e^* = \left(\frac{z(z-1)}{(M_c+B_c+K_c)z^2-(2M_c+B_c)z+M_c}\right)F_e^* \tag{76}$$

or

$$V_h^* - V_e^* = Y_{CI}F_e^* = \left(\frac{z(z-1)}{x_1(z^2-x_2z+x_3)}\right)F_e^* \tag{77}$$

Like before, this second order form of virtual coupling may be extended into a more universal form, such as

$$V_h^* - V_e^* = Y_{CI}F_e^* = \left(\frac{z^2-x_4z+x_5}{x_1(z^2-x_2z+x_3)}\right)F_e^* \tag{78}$$

Alternatively, if bilinear, or Tustin, conversion were used to convert the virtual coupling it would take the following forms

$$V_h^* - V_e^* = Y_{CI}F_e^* = \left(\frac{2(z-1)}{(2B_c+K_c)z-(2B_c-K_c)}\right)F_e^* \tag{79}$$

or with a pseudo virtual mass,

$$Y_{CI}F_e^* = \left(\frac{2(z+1)(z-1)}{(4M_c+2B_c+K_c)z^2-(8M_c-2K_c)z+(4M_c-2B_c+K_c)}\right)F_e^* \tag{80}$$

or

$$Y_{CI}F_e^* = \left(\frac{(z+1)(z-1)}{x_1(z^2 - x_2 z + x_3)}\right) F_e^* \tag{81}$$

Bilinear transformation leads to the same effective form for the spring-damper model as backwards difference transformation (equations (74), (79), & (75)), but leads to a slightly different form for the mass, spring, damper model (equations (76) & (80) or (77) & (81)). Again, the general pole / zero form, allowing independent tuning of the coupling's zeros from the poles, as outlined by equation (78), can reproduce the backwards difference or the bilinear model.

When used in the I/A network these virtual couplings serve to limit transferred velocities from the haptic device to the remote environment, or similarly limit the transmission of an impulse from the environment to the haptic device. This is done by regulating the velocity sent to the environment through feedback of force applied by the environment. Alternatively, when used in an I/I network it serves to generate the desired haptic device and applied environment force. Though often not posed as a two–port network, the I/I network with (74) as virtual coupling and without force feedback is merely the traditional haptic network which utilizes PD position control to link the master with the slave / environment.

Future chapters will compare and contrast these various virtual coupling models when applied to a theoretical test case and a real world experimental system. Do the higher order models add to the performance? Does their increased complexity create implementation issues? These questions, and others like them, will be addressed in future chapters.

5.2 Dualality Between Impedance and Admittance Networks

Adams and Hannaford found a relationship between tuning the A/I velocity servo controller and tuning the I/A network's virtual coupling. Likewise, there is a similar correlation for

tuning the force feedback controller. To show this relationship the previous A/I and I/A two–port network models presented in past chapters will be used. First, the A/I network can be expressed as an I/A network by taking its inverse

$$\begin{bmatrix} F_h(j\omega) \\ -V_e^*(e^{j\omega T}) \end{bmatrix} = \begin{bmatrix} H(j\omega) & -Q(j\omega) \\ M(j\omega) & Z_{CA}(e^{j\omega T}) \end{bmatrix}^{-1} \begin{bmatrix} V_h(j\omega) \\ F_e^*(e^{j\omega T}) \end{bmatrix} \tag{82}$$

Similarly the I/A network can be expressed as an A/I network by taking its inverse

$$\begin{bmatrix} V_h(j\omega) \\ F_e^*(e^{j\omega T}) \end{bmatrix} = \begin{bmatrix} G(j\omega) & P(j\omega) \\ -D(j\omega) & Y_{CI}(e^{j\omega T}) \end{bmatrix}^{-1} \begin{bmatrix} F_h(j\omega) \\ -V_e^*(e^{j\omega T}) \end{bmatrix} \tag{83}$$

Through simple matrix algebra it is easy to see that the inverse transfer functions in equations (82) and (83) can be manipulated into

$$\begin{bmatrix} H(j\omega) & -Q(j\omega) \\ M(j\omega) & Z_{CA}(e^{j\omega T}) \end{bmatrix}^{-1} = \frac{1}{H(j\omega)Z_{CA}(e^{j\omega T}) + Q(j\omega)M(j\omega)} \begin{bmatrix} Z_{CA}(e^{j\omega T}) & Q(j\omega) \\ -M(j\omega) & H(j\omega) \end{bmatrix} \tag{84}$$

$$\begin{bmatrix} G(j\omega) & P(j\omega) \\ -D(j\omega) & Y_{CI}(e^{j\omega T}) \end{bmatrix}^{-1} = \frac{1}{G(j\omega)Y_{CI}(e^{j\omega T}) + P(j\omega)D(j\omega)} \begin{bmatrix} Y_{CI}(e^{j\omega T}) & -P(j\omega) \\ D(j\omega) & G(j\omega) \end{bmatrix} \tag{85}$$

In linear two–port analysis, passivity based stability properties of a network are held for the network's inverse. Therefore, if the two–port network satisfies passivity or Llewelyn stability, so will its inverse. Since the diagonal terms of a Llewelyn stable two–port network are passive, so will the diagonal terms of its inverse; therefore the terms of most interest in (84) and (85) are the upper left diagonal terms, specifically

$$\frac{Z_{CA}(e^{j\omega T})}{H(j\omega)Z_{CA}(e^{j\omega T}) + \hat{Q}(j\omega)M(j\omega)} \tag{86}$$

and

$$\frac{Y_{CI}(e^{j\omega T})}{G(j\omega)Y_{CI}(e^{j\omega T}) + P(j\omega)D(j\omega)} \tag{87}$$

If equations (53), (54), and (43) are used for $G(j\omega)$, $P(j\omega)$, and $H(j\omega)$ respectively, along with

$$\hat{Q}(j\omega) = \frac{\left(1 + K_v(e^{j\omega T})\right) e^{-j\omega T/N} ZOH(j\omega)L(j\omega)}{Z_d(j\omega) + D(j\omega)K_v(e^{j\omega T})e^{-j\omega T/N} ZOH(j\omega)L(j\omega)} \tag{88}$$

for $Q(j\omega)$, equation (86) becomes

$$\frac{Z_{CA}(e^{j\omega T})\left(Z_d(j\omega)+D(j\omega)K_v(e^{j\omega T})e^{-j\omega T/N}ZOH(j\omega)L(j\omega)\right)}{Z_{CA}(e^{j\omega T})+\left(1+K_v(e^{j\omega T})\right)e^{-j\omega T/N}ZOH(j\omega)L(j\omega)M(j\omega)} \tag{89}$$

and equation (87) becomes

$$\frac{Y_{CI}(e^{j\omega T})\left(1+K_f(e^{j\omega T})e^{-j\omega T/N}ZOH(j\omega)L(j\omega)M(j\omega)\right)}{Y_{CI}(e^{j\omega T})Z_d(j\omega)+\left(1+K_f(e^{j\omega T})\right)D(j\omega)e^{-j\omega T/N}ZOH(j\omega)L(j\omega)} \tag{90}$$

Slightly differing from the previous definition of $Q(j\omega)$, equation (44), equation (88) has a unity feed forward component in the numerator. Though this unity feed forward term is not physically intuitive when thinking of velocity feedback control with a force actuated device, it results in equation (89) having an insightful form. Specifically if $K_v(e^{j\omega T})$ and $K_f(e^{j\omega T})$ are set to zero, equations (89) and (90) become

$$\frac{Z_d(j\omega)}{1+Z_{CA}^{-1}(e^{j\omega T})e^{-j\omega T/N}ZOH(j\omega)L(j\omega)M(j\omega)} \tag{91}$$

and

$$\frac{1}{Z_d(j\omega)+D(j\omega)Y_{CI}^{-1}(e^{j\omega T})e^{-j\omega T/N}ZOH(j\omega)L(j\omega)} \tag{92}$$

As already noted, if the A/I and I/A networks satisfy the Llewelyn stability criterion, their two–port transfer function's upper left diagonal term, $H(j\omega)$ and $G(j\omega)$ respectively, will be passive. Furthermore, the networks' inverse two–port transfer function upper left diagonal terms, (91) and (92) must also be passive. Closer inspection of (91) reveals it highly resembles $G(j\omega)$, being identical if $Z_{CA}^{-1}(e^{j\omega T}) \equiv K_f(e^{j\omega T})$; similarly (92) highly resembles $H(j\omega)$, being identical if $Y_{CI}^{-1}(e^{j\omega T}) \equiv K_v(e^{j\omega T})$.

This alludes to the notion that if the I/A network's virtual coupling were inverted and used for the velocity feedback controller, $H(j\omega)$ would be passive. Likewise, if the A/I network's virtual coupling were inverted and used for the force feedback controller, $G(j\omega)$ would be passive. Following this logic one can use the A/I version of the network without a velocity feedback controller, only using the unity feed-forward controller, and tune the admittance coupling; guaranteeing that (91) is passive. Next, this coupling's inverse can be used as the force controller in the I/A network; guaranteeing that $G(j\omega)$ is passive. After

this the I/A network with force feedback control can be completed through tuning its virtual coupling. Likewise, a similar process can be performed to tune the admittance network's velocity controller through tuning the virtual coupling for the I/A network without a force feedback controller, using the inverse of this virtual coupling as the velocity controller, and then completing the A/I network through tuning of its virtual coupling. This shows the true duality between the A/I and I/A networks.

It is also interesting to note the form of the feedback controller for the A/I and I/A networks given the previously presented virtual coupling forms. If the inverse of equation (74) were used as the velocity controller, K_v would take the form of a PI controller with $K_P \equiv B_C$ and $K_I \equiv K_C$; which is also equivalent to a PD controller acting on position instead of velocity. Similarly, if the inverse of (67) were used as the force controller, K_f would take the form of a PI controller with $K_P \equiv 1/B_C$ and $K_I \equiv 1/M_C$.

5.3 "Optimal" Tuning of Two–Port Network Parameters

Tuning of the virtual coupling can be set up as a nonlinear optimization problem. Tuning should minimize virtual coupling while keeping it both passive and it's real part greater than the stability condition. Furthermore, $G(j\omega)$ and $H(j\omega)$ must remain passive. This optimal problem encompasses minimizing a cost function while satisfying several constraints for a sweep of applicable frequencies. One such structure for the problem utilizes a cost function that is based on both the magnitude of the virtual coupling

$$\text{Error}_1 = \sqrt{\frac{1}{n}\sum_{i=1}^{n}\left[\left(\frac{1}{\sqrt{(\tau\omega_i)^2+1}}\right)|Virtual\_Coupling(e^{j\omega_i T})|\right]^2} \tag{93}$$

and a normalized difference between the stability criterion and the real part of the virtual coupling

$$\text{Error}_2 = \sqrt{\frac{1}{n}\sum_{i=1}^{n}\left[\left(\frac{1}{\sqrt{(\tau\omega_i)^2+1}}\right)\left(\frac{\text{Re}\left[Virtual\_Coupling(e^{j\omega_i T})\right]}{Stability\_Condition(j\omega_i)}-1\right)\right]^2} \tag{94}$$

combined to form a total cost of

$$\text{Cost} = \alpha \cdot \text{Error}_1 + \beta \cdot \text{Error}_2 \tag{95}$$

Required inequality constraints can be expressed as

$$\mathrm{Re}\left[Virtual\_Coupling(e^{j\omega_i T})\right] - Stability\_Condition(j\omega_i) > 0 \tag{96}$$

$$\mathrm{Re}\left[G(j\omega_i)\right] > 0 \quad \text{or} \quad \mathrm{Re}\left[H(j\omega_i)\right] > 0$$

$$|\mathrm{Poles}\left[Virtual\_Coupling(z)\right]| - 1 \leq 0$$

$$|\mathrm{Zeros}\left[Virtual\_Coupling(z)\right]| - 1 \leq 0$$

Alternatively, another definition of cost is to use error in db instead of RMS, as outlined by

$$\mathrm{Error}_1 = \frac{1}{n}\sum_{i=1}^{n} 20\log_{10}\left[\left(\frac{1}{\sqrt{(\tau\omega_i)^2+1}}\right)\left|Virtual\_Coupling(e^{j\omega_i T})\right|\right] \tag{97}$$

and

$$\mathrm{Error}_2 = \frac{1}{n}\sum_{i=1}^{n} 20\log_{10}\left[\left(\frac{1}{\sqrt{(\tau\omega_i)^2+1}}\right)\frac{\mathrm{Re}\left[Virtual\_Coupling(e^{j\omega_i T})\right]}{Stability\_Condition(j\omega_i)}\right] \tag{98}$$

Inspection of the cost functions shows the use of a frequency based weighting, or filter. This allows penalty emphasis to be concentrated on low frequency values that are more likely to be perceived by the human. Objective of the tuning should be to minimize virtual coupling compliance (I/A network) or stiffness (A/I network), while satisfying stability constraints. This equates to $\alpha = 1$ and $\beta = 0$ in the suggested cost function (95). Unless otherwise noted, all cost in the following chapters will be reported with $\alpha = 1$ and $\beta = 0$, though due to complexities of the nonlinear optimal problem other forms may have been utilized to tune the reported coupling. Similarly, use of error in db or RMS depends on which results in a more robust optimal tuning algorithm.

Constrained nonlinear optimal algorithms can be used to solve this problem once given specific models for the components of the two–port network. Unfortunately nonlinear optimal algorithms can be highly sensitive to local minimums and initial conditions. Through many trial and errors with various initial conditions and coupling forms it was determined tuning of the networks in the following chapters is an iterative process. It is advantageous to

first start with less complicated forms of virtual coupling to get a baseline. Usually directly tuning stiffness and damping for the I/A coupling or damping and mass for the A/I coupling results in a decent initial solution, then higher order forms can be tuned and compared. If generic initial conditions for the higher order coupling does not result in equivalent or better solutions, the previous lower order solutions can be used as initial conditions. Solutions from the optimal algorithm should be compared through inspection of the network's impedance / admittance limits, bode diagram of the coupling, and how well the stability criterion is satisfied. Occasionally a coupling which has the lowest cost value does not yield the most desirable solution once the completed network's overall characteristics is evaluated through all applicable frequencies.

As outlined in earlier sections, tuning of the two–port networks is a two parameter, or two controller problem. In future chapters the following procedure will be used for "tuning" the haptic two–port networks.

1. Use the inverse causality of the model, that is use I/A model if A/I is the desired final implementation and visa versa. Set the inverse model's feedback controller to zero, but use unity feed forward for the respective controller.

2. Tune the inverse network's virtual coupling through use of constrained nonlinear optimal algorithms. Use this tuned virtual coupling as the feedback controller in the desired final network.

3. After incorporating the feedback controller, tune the final virtual coupling for the completed network.

4. Review Impedance / Admittance limits of the completed network as well as required stability constraints; possibly relaxing the feedback controller to allow more freedom with the virtual coupling tuning.

5.4 General Comments on Tuning

While future chapters will illustrate the outlined tuning procedure for an experimental haptic test bed, considerable time was spent tuning these two–port networks for an initial test case so as to explore tuning of two–port networks and gain insight on selecting coupling or feedback controller form. This test case was structured around a hypothetical haptic device modeled as a simple mass with various damping. Results from these test cases will not be presented, but rather general observations gained from the exercise.

Optimal nonlinear problems are often troublesome to solve. First, such problems can be sensitive to initial guesses. Second, structuring of the problem and specifics of which variables are directly tuned can affect robustness of converging on a solution. Through the initial test case it was often found that tuning the coupling's "physical parameters" normalized by sampling rate (M_cT, K_c/T, & B_c) resulted in quicker convergence than without normalizing. Brief investigation of bilinear transformation based coupling models revealed the resulting coupling discrete transfer function was usually equivalent to when backwards difference based models were used; with bilinear based impedance mass-spring-damper virtual coupling being the only model form that differed from its backwards difference counterpart. Directly tuning coupling's gains, zeros, and poles usually resulted in an equivalent solution to when "physical parameters" are tuned for the equivalently structured coupling model. When expanding the virtual coupling order it was observed quicker and more robust convergence of the optimal algorithm resulted when using a lower order solution as the initial guess. For example, one can use the first order virtual coupling as an initial solution in the expanded models to see if there is any benefit to the increased complexity. One should still attempt to solve the more complex coupling with "generic" initial guesses so as to verify the previous solutions are not trapped in local minimums, but one should not be surprised if "generic" initial guesses lead to less optimal or erroneous solutions.

Unfortunately some of the solutions can be susceptible to numerical round off. Occasionally the stability criterion was not preserved when verifying solutions using finite significant

digits; requiring increased significant digits to properly recreate the tuned virtual coupling. This raises a very practical problem with numerical algorithms that is worth mentioning. When is a result more a function of the precision in which the calculations are performed instead of the physical model? When can values be rounded for practical implementation and when do precise values represent important information? Often numerical roundoff issues can be addressed by simply reparameterizing so as to more accurately capture the solution's numerical relationships. This topic is discussed in in more detail in Chapter 7 where example solutions can be referenced. Furthermore, "optimal solutions" are only optimal for the problem as structured. Changing cost functions (filter, RMS, db, etc.), resolution the simulated model properties are sampled for different operating frequencies (ie varying model data points in different decades to effectively adjust weighting of model results in said decades) can change the results. Therefore "optimal" is not necessarily the "best" solution, but rather a tool for converging tuning parameters based on a structured metric.

Finally, as previously mentioned, tuning of a two–port networks with both feedback and virtual coupling is a two parameter problem. Increasing feedback control stiffness usually requires relaxing virtual coupling. Therefore the stiffest feedback controller is often not the best choice, rather a balance must be made.

CHAPTER 6

EXPERIMENTAL SYSTEM (HURBIRT)

6.1 Description of HuRBiRT

HuRBiRT is a two-dof haptic robot based on a five bar mechanism. For actuators HuRBiRT's original design utilized two DC motors with built in encoders and a strain gage based force sensing handle. Part of this research is to incorporate a passive actuator on at least one of HuRBiRT's axis, providing an axis with hybrid passive / active actuation. Table 4 lists HuRBiRT's actuators, their respective torque ratings, power transmissions, and resultant torque limits available to the links.

Both motors are powered by PMI AXA-180-10-30 PWM amplifiers in current mode and can be considered torque sources, while the magnetic rheological brake provides resistive torque dependent on applied current, independent of rotational speed. Kepco BOP 36-1.5(M) power supply with a current sensing resistor is utilized for supplying the regulated current to the brake. Because the rheological brake's torque is essentially independent of speed, to simulate damping the command signal to the brake system is determined from desired damping and calculated link speed. While the resulting damping is not a true

Table 4: HuRBiRT's Actuators

Axis	**#1**	**#2**	**#2**
Actuator Type	**DC Motor**	**DC Motor**	**Rheological Brake**
Manufacturer	Kollmorgen	Kollmorgen	Lord
Model	JR16M4CH	JR12M4CH	MRB-2107-3
Peak Torque	36.8 N-M	13.3 N-M	N.A.
Continuous Torque	3.3 N-M	1.3 N-M	5.6 N-M
Gear Drive	Harmonic Drive 60:1	Gear Box 20:1	Timing Belt 6:1
Peak Link Torque	2,208 N-M	266 N-M	N.A.
Continuous Link Torque	198 N-M	26 N-M	33.6 N-M

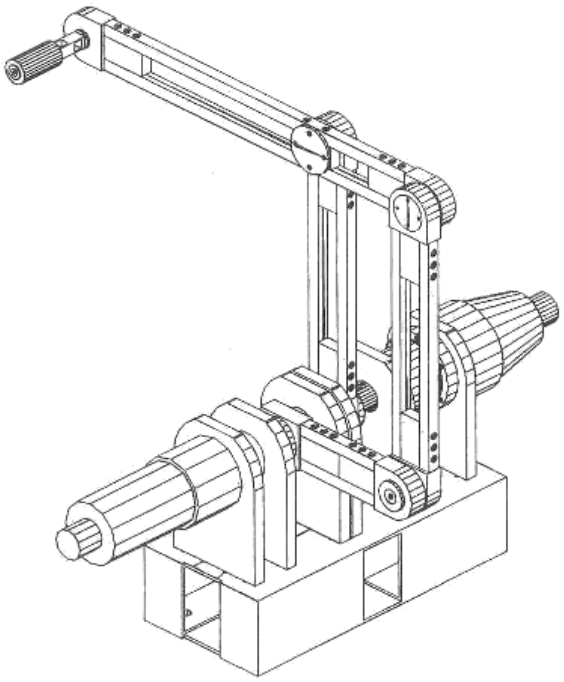

Figure 29: HuRBiRT (Human Robotic Bilateral Research Tool)

physical velocity based damping, that is the resisting torque is subject to quantization and sample and hold of calculated speed, it is guaranteed to be dissipating. In contrast when "simulating" damping with digitally controlled active motors (equation (99)), zero velocity crossings between time samples may cause the applied "resistive torque" to add energy; alternatively the rheological brake can only apply dissipating resistive torque (equation (100)).

$$\tau = b\dot{\theta}_{measured} \tag{99}$$

$$\tau = b\left|\dot{\theta}_{measured}\right|\mathrm{sgn}(\dot{\theta}) \tag{100}$$

6.2 Modeling of HuRBiRT

True modeling of HuRBiRT's dynamics can be complex. In addition to friction, physical damping, and inertial dynamics of the gear train, HuRBiRT's true link dynamics are non-linear. Based on Lagrangian analysis the dynamic equations of motion for HuRBiRT's five bar mechanism with damping and friction can be expressed as

$$\tau_1 = d_{11}\ddot{\theta}_1 + d_{12}\sin(\theta_1+\theta_2)\ddot{\theta}_2 + d_{12}\dot{\theta}_2^2\cos(\theta_1+\theta_2) + b_1\dot{\theta}_1 + f_1\mathrm{sgn}(\dot{\theta}_1) - \phi_1\sin(\theta_1)$$

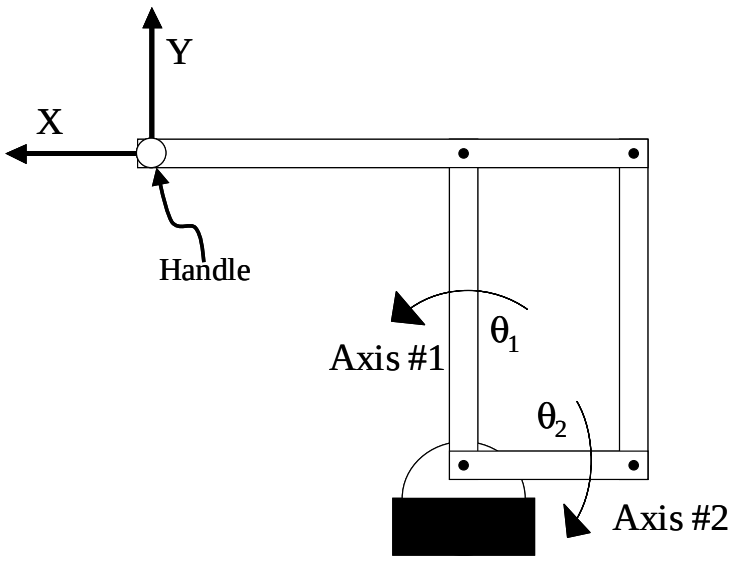

Figure 30: HuRBiRT's Axis Configuration

Table 5: HuRBiRT's Modeling Parameters

Variable	Description
d_{11}, d_{22}	Primary Link Inertia
d_{12}	Links' Cross Inertia
b_1, b_2	Link Viscous Damping
f_1, f_2	Link Coulomb Friction
ϕ_1, ϕ_2	Link Gravitational Imbalance

$$\tau_2 = d_{22}\ddot{\theta}_2 + d_{12}\sin(\theta_1+\theta_2)\ddot{\theta}_1 + d_{12}\dot{\theta}_1^2\cos(\theta_1+\theta_2) + b_2\dot{\theta}_2 + f_2\text{sgn}(\dot{\theta}_2) + \phi_2\cos(\theta_2) \quad (101)$$

It should be noted that system friction and damping guarantee the mechanical system is dissipative. Ignoring all nonlinear terms except for gravity and friction results in the following simplified dynamic equations

$$\begin{aligned} \tau_1 &= d_{11}\ddot{\theta}_1 + b_{1(eq)}\dot{\theta}_1 + f_1\text{sgn}(\dot{\theta}_1) - \phi_1\sin(\theta_1) \\ \tau_2 &= d_{22}\ddot{\theta}_2 + b_{2(eq)}\dot{\theta}_2 + f_2\text{sgn}(\dot{\theta}_2) + \phi_2\cos(\theta_2) \end{aligned} \quad (102)$$

Coefficients of the gravity terms were determined through initial measurement of unbalance and tuned through trial and error while other dynamic properties were determined

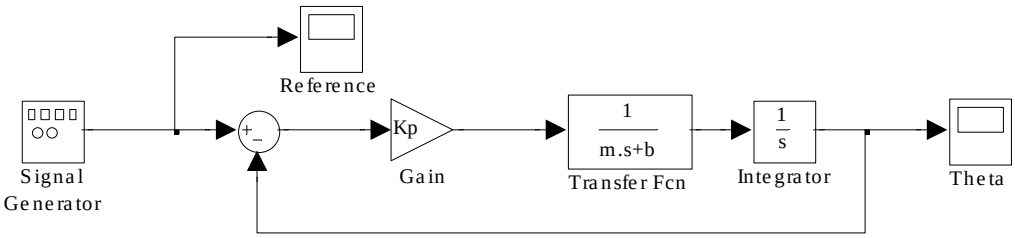

Figure 31: Proportional Feedback Control with Assumed Model

using frequency based input-output data. To experimentally acquire frequency based input-output data for each axis the other axis was locked while simple proportional control with gravity compensation was used to close the loop on the axis in question (see figure 31). Simple proportional control results in a system that can be approximately modeled with frequency based equation (103).

$$\frac{Out_i(\omega_{dr})}{In(\omega_{dr})} = \frac{k_p}{-d_{ii}\omega_{dr}^2 + \left(b_i + \frac{4f_i}{\pi\omega_{dr}Out_i(\omega_{dr})}\right)\omega_{dr}j + k_p} \tag{103}$$

Worth noting is the term

$$\left(\frac{4f_i}{\pi\omega_{dr}Out_i(\omega_{dr})}\right)\omega_{dr}j \tag{104}$$

used to describe the effects of friction on the frequency response. Refer to Appendix A for more information regarding the origin of equation (104). Input amplitudes were adjusted so as to guarantee the motors did not saturate and the device stayed within the allowable workspace limits while fixed frequencies were chosen from ≈0.01 Hz to ≈10Hz. Using frequency based gain and phase experimentally determined through DFT processing, the dynamic properties d_{ii}, b_i, and f_i were solved for by fitting equation (103) to the collected data. (see table 6) Figures 32, 33, and 34 illustrate the experimental frequency data and resulting simplified model. Two sets of data for HuRBiRT's second , the first (Axis #2) corresponds to not using the extra brake actuator for simulating damping and the second (Axis #2 B) corresponds to using the brake actuator to simulate increased damping. Desired damping when using the brake was set close to the maximum so as not to saturate the brake actuator with the resulting velocity response of the axis.

Table 6: HuRBiRT's Dynamic Parameters

Axis	**#1**	**#2**	**#2 B**
k_p $(^{(N-m)}/_{rad})$	750	200	200
d_{ii} $(Kg\text{–}m^2)$	13.5	2.45	2.45
b $(^{(N-m)s}/_{rad})$	33	0	24.5
f $(N\text{–}m)$	37.9	4.26	3.28
ϕ $(N\text{–}m)$	90	-2.0	-2.0

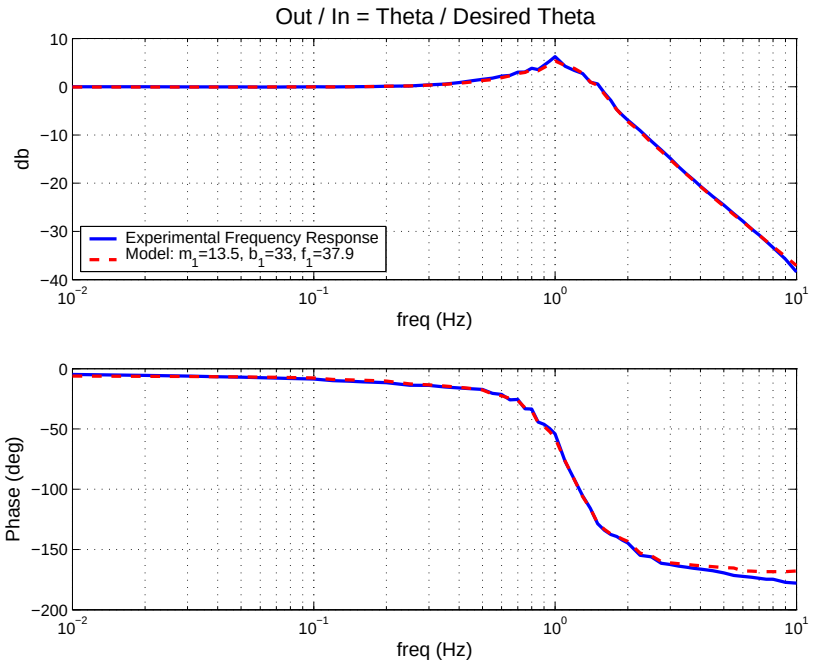

Figure 32: Axis #1 $\theta(s)/\theta_r(s)$ Frequency Response (experimental and model)

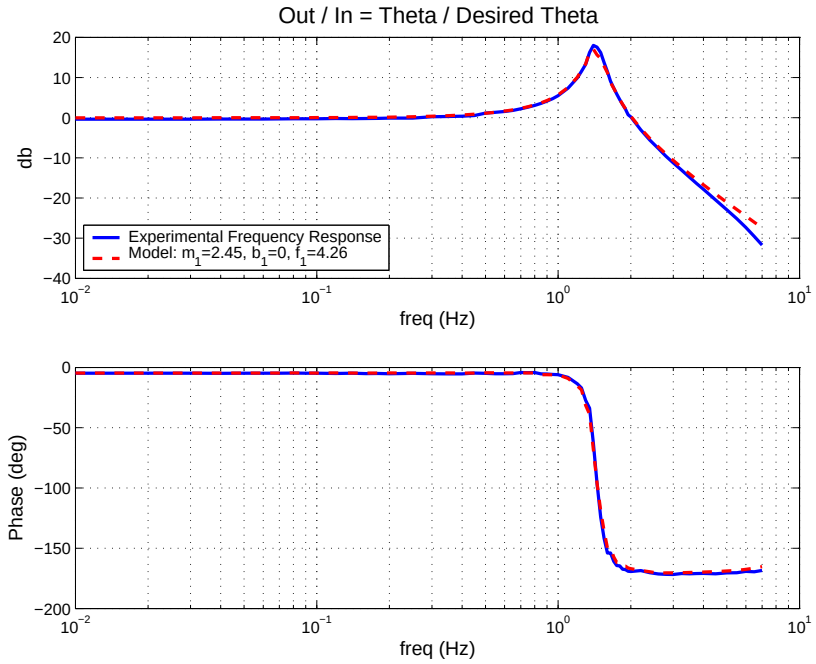

Figure 33: Axis #2 $\theta(s)/\theta_r(s)$ Frequency Response (experimental and model)

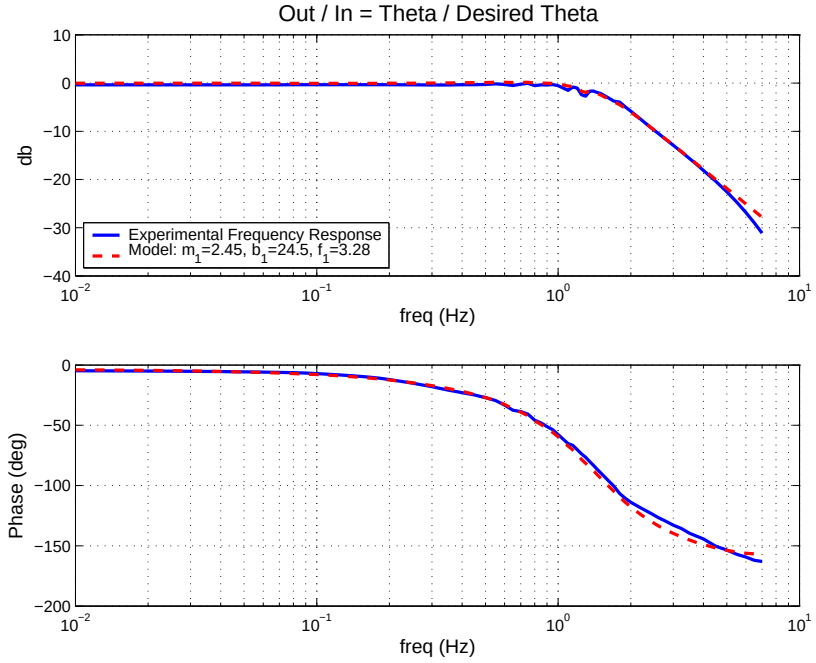

Figure 34: Axis #2 B $\theta(s)/\theta_r(s)$ Frequency Response (experimental and model)

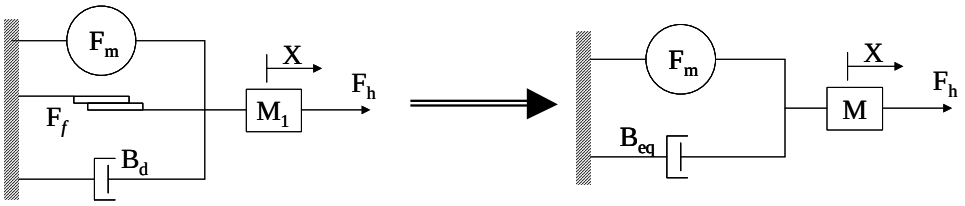

Figure 35: Modeling Friction with Equivalent Damping

Inspection of the open loop transfer functions, with torque as the input and position (figures 36, 37, 38 and 39) or velocity (figures 40, 41, 42, and 43) as the output, show the effects of friction on the response. As outlined in Appendix A, equivalent damping of friction is dependent on both driving frequency and magnitude of the velocity response. Velocity magnitude was low at low frequencies, increasing effective low frequency damping over traditional damping. This results in the frequency response magnitude of output theta vs. input torque to level off at low frequency and for the frequency response magnitude of output angular velocity vs. input torque to decrease ≈ 20 db/decade as frequency decreases.

In order to use previously outlined techniques for tuning the two–port networks, friction needs to be converted into equivalent damping b_{eq} through use of

$$b_{eq} = b_d + \frac{4f}{\pi V} \tag{105}$$

For estimating V the velocity response of the system for the experimental frequency data was inspected to extract the maximum velocity magnitude. Knowing that the experimental frequency response used input values that maximized travel in the workspace while preventing actuator saturation, maximum velocity of the frequency response data can be assumed an estimate of maximum velocity. Regardless, this value was slightly increased to give a conservative estimate of equivalent damping. Table 7 lists said equivalent damping along with the estimate of maximum velocity. Because this is a conservative estimate of damping, there should be more dissipation in the real system than estimated by the model. These models are used in future sections for tuning the virtual coupling across a wide frequency spectrum, while actual experimental data is used to verify resulting networks are stable within actual frequency data range collected.

Table 7: Equivalent Friction Damping

Axis	#1	#2	#2 B
f $(N–m)$	37.9	4.26	3.28
V $(^{rad}/_{s})$	2.70	3.70	2.00
$\approx b_{eq_f}$ $(^{(N-m)s}/_{rad})$	17	1.5	2
b $(^{(N-m)s}/_{rad})$	33	0	24.5
b_{eq} $(^{(N-m)s}/_{rad})$	50	1.5	26.5

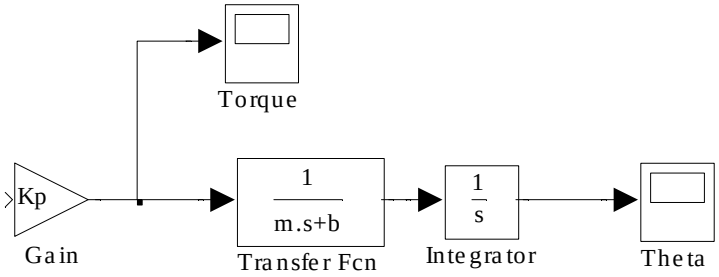

Figure 36: Block Diagram for $\theta(s)/\tau(s)$

6.3 Other Components of HuRBiRT

HuRBiRT incorporates a two axis force sensing handle so that it can be used in either the traditional impedance, admittance, or impedance with force feedback haptic structure. Signals from the handle's full bridge strain gauge circuits are filtered with a 250 Hz analog two pole low pass Butterworth filter. Digital control at 1 KHz is through a DS1102 controller card programed with Mathwork's Real Time Workshop. Link angle measured with the encoders has a resolution of $3.0x10^{-4}$ degrees for axis #1 and $9.0x10^{-4}$ degrees for axis #2; corresponding to a position resolution of 0.183 mm for axis #1 and 0.549 mm for axis #2.

Appendix B outlines implementation of EMF Damping on DC motors. Essentially EMF Damping provides motor current attenuation and increased physical damping at frequencies above the selected EMF damping corner frequency. Selection of the components used in such a system depend on the device's electrical motor characteristics. Table 8 lists the

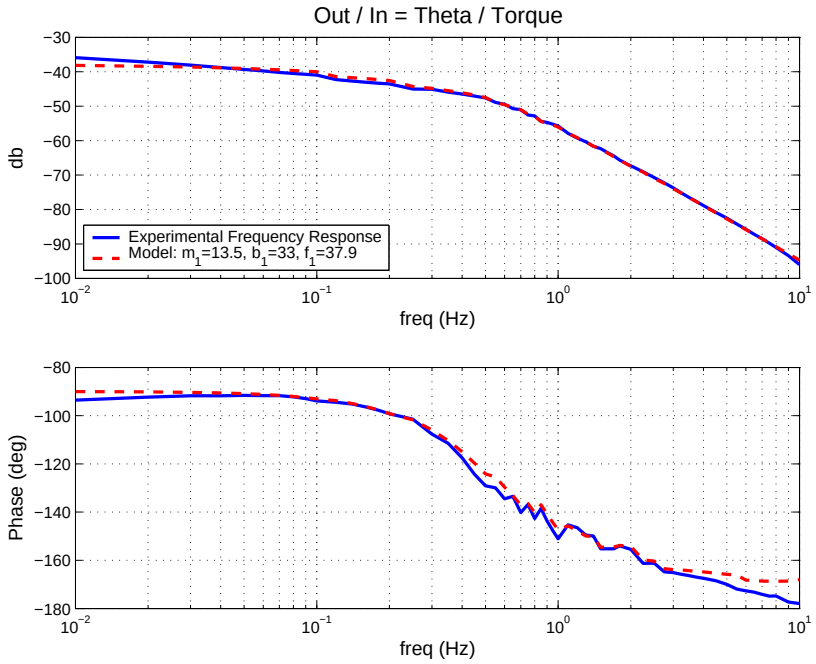

Figure 37: Axis #1 $\theta(s)/\tau(s)$ Frequency Response (experimental and model)

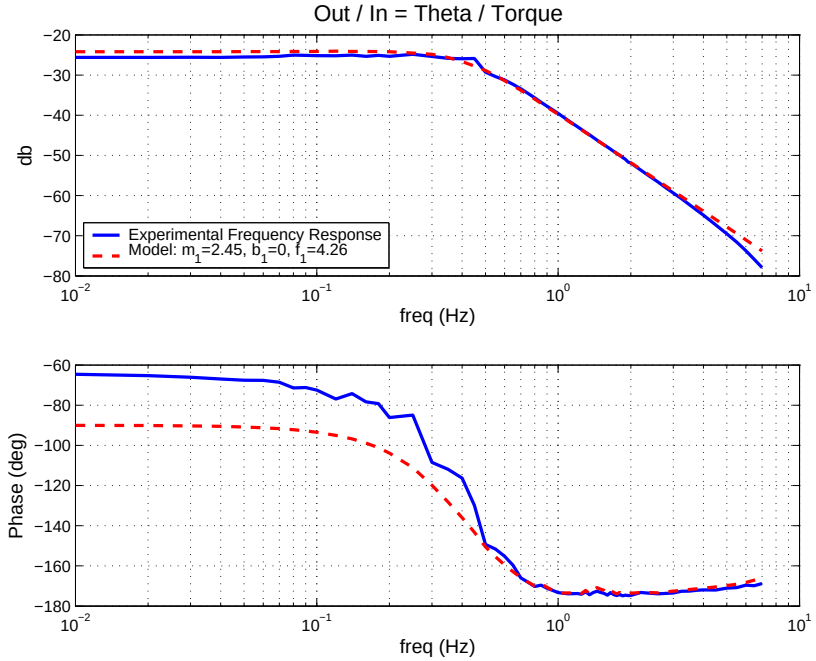

Figure 38: Axis #2 $\theta(s)/\tau(s)$ Frequency Response (experimental and model)

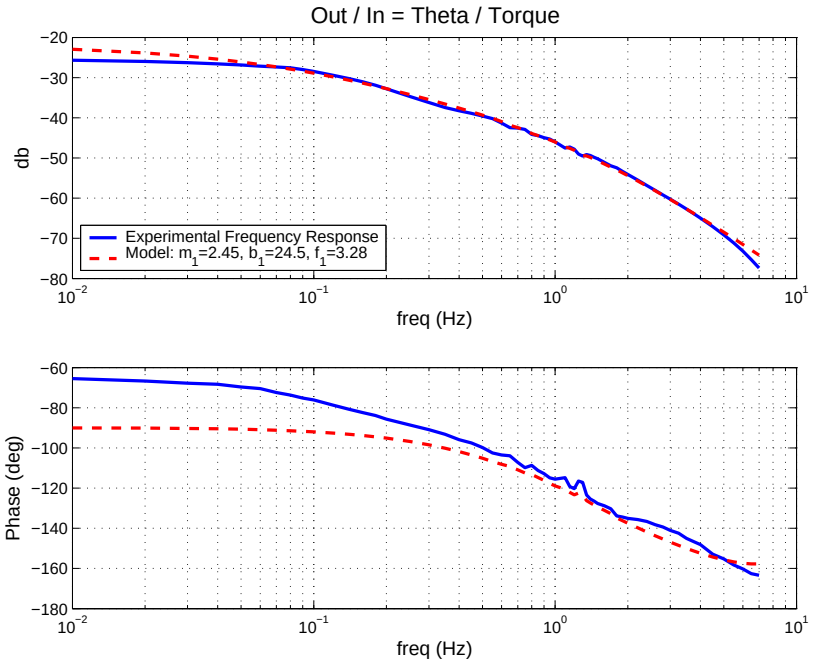

Figure 39: Axis #2 B $\theta(s)/\tau(s)$ Frequency Response (experimental and model)

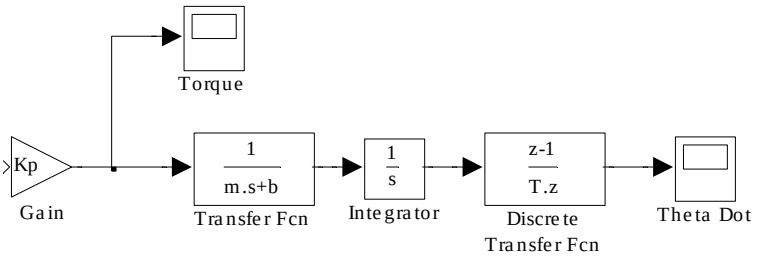

Figure 40: Block Diagram for $\dot{\theta}(s)/\tau(s)$

Table 8: HuRBiRT's Motor's Electrical Characteristics

Axis		**#1**	**#2**
Manufacturer		**Kollmorgen**	**Kollmorgen**
Model		**JR16M4CH**	**JR12M4CH**
Drive Ratio – GR		60:1	20:1
Torque Constant – K_t	N-m/amp	.3728	.1702
Back EMF Constant – K_v	V/KRPM	39	17
Terminal Resistance – R_t	ohms	0.94	0.95
Coil Inductance – L	μH	< 85	< 45

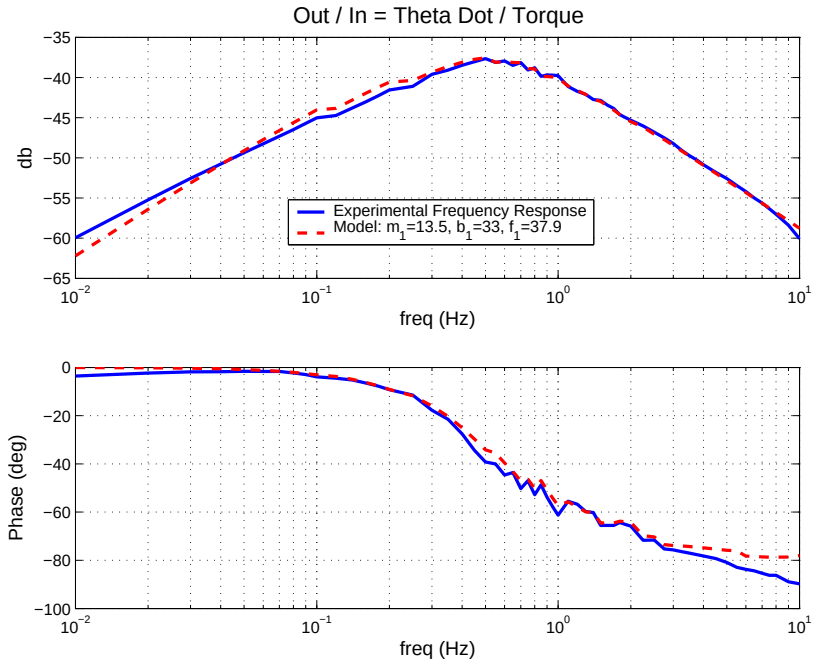

Figure 41: Axis #1 $\dot{\theta}(s)/\tau(s)$ Frequency Response (experimental and model)

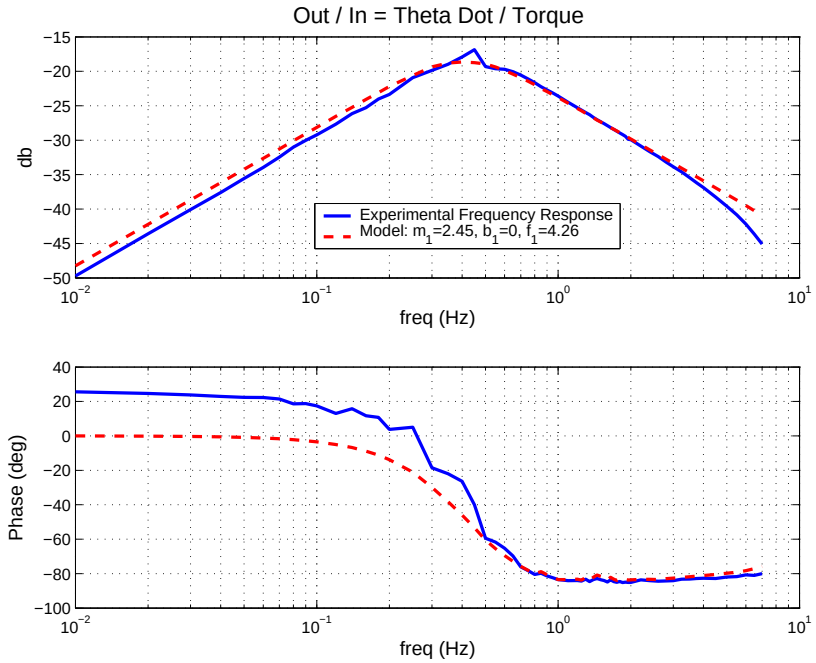

Figure 42: Axis #2 $\dot{\theta}(s)/\tau(s)$ Frequency Response (experimental and model)

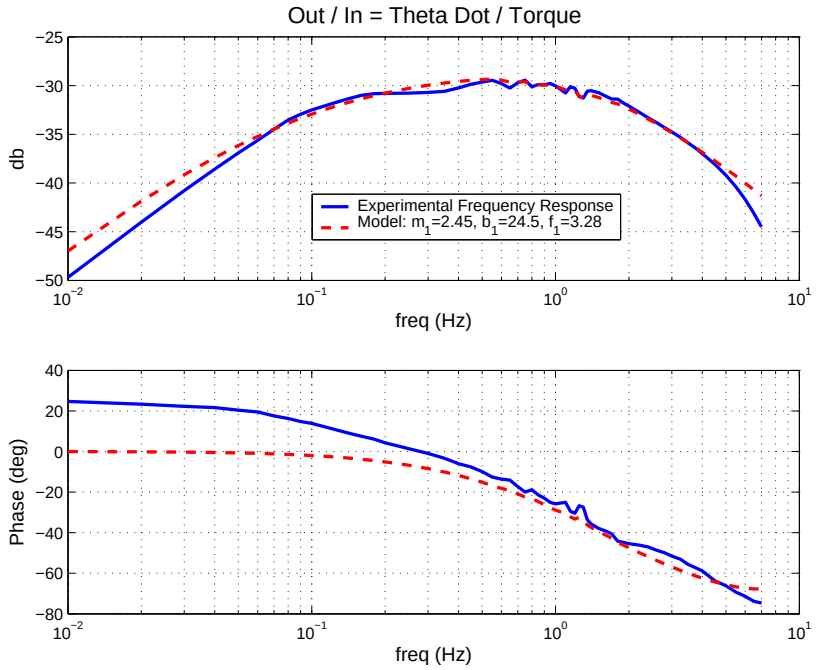

Figure 43: Axis #2 B $\dot{\theta}(s)/\tau(s)$ Frequency Response (experimental and model)

required electrical parameters for both of HuRBiRT's axis. Future sections will explore the use of such EMF damping and it's affects on tuning the haptic two–port networks.

It's also worth noting that HuRBiRT is not a perfect device and exhibits various non-linear qualities besides friction. For example the harmonic drive has a cogging affect as the wave generator rotates and the gear box transmission has slight backlash. Both PWM motor amplifiers have built in over current circuits that limit the time peak current can be delivered to them motors, dropping current to the tuned "constant current" setting. This usually only affects axis #2 because it has a lower torque capability. Lord's rheological brake has some backlash as well as a small dynamic response between resisting torque and applied actuation current. Furthermore the force senosr's strain gage circuits were "zeroed" in a default position of the links. As axis #2 rotated the weight of the handle transfered between orthogonal force circuits. This required compensation in the software through estimate of the handle's weight with position of link #2 as well as a small dead band region in processing of the force sensor signal. Finally, in the previously outlined models it was assumed the gear train acted ideally. At very high frequencies the harmonic drive may have

compliance that causes additional dynamics and the gearbox backlash may allow for high frequency vibration of the motor within the backlash limits. Furthermore, these "compliances" in the gear train may create a non-collocation between applied motor torque and measured handle force. Such non-collocation may create stability issues when implementing force feedback control.

Future sections will explore the application of previously outlined two–port networks on this real world system. Comparison of theoretically tuned network parameters with experimentally derived parameters will be performed for both axis #1 and the hybrid axis #2.

CHAPTER 7

NETWORK TUNING FOR HURBIRT'S AXIS #1

This chapter will use the model previously developed for HuRBiRT's axis #1 to illustrate tuning of the feedback controllers and virtual couplings. Impedance / admittance limits of the resulting two–port networks will be compared so as to gain better insight into selection of which form is most appropriate given a desired task. As previously mentioned, the dSpace / Real-Time Workshop digital controller's sampling rate was set at 1 KHz. Power supply / motor amplifier dynamics are assumed to be negligible and the control loop delay is assumed to be one sample period. Again, the handle's force sensor signal is filtered by a 250 Hz analog two-pole Butterworth filter and the position signal is filtered by a 250 Hz two-pole digital Butterworth filter. Only parameters left to define are those associated with the cost function. Tuning results in this chapter correspond to equations (95), (97) and (98) with $\alpha = 1$, $\beta = 0$, and $\tau = .01$. Matlab's constrained nonlinear optimal algorithm 'fmincon' was used to process the optimal tuning algorithm. Please refer to Matlab's documentation for more information regarding Matlab's algorithm.

7.1 Impedance / Admittance Network – Without Force Feedback

Tuning an I/A network without force feedback is a traditional impedance network. Virtual coupling parameters resulting from tuning such a network for HuRBiRT's axis #1 are listed in table 9. Values which are not in shaded cells of the table were directly derived from the optimal tuning, while values in shaded cells are calculated from said results of the optimal tuning algorithm. Variables Kc, Bc, Mc, and X(1) through X(5) correspond to variables in the various virtual coupling equations outlined in Chapter 4, with all coupling models that

Table 9: Axis #1 I/A Network Virtual Coupling (without force feedback)

	Coupling Solutions				
Coupling Parameters	Yci-1	Yci-2	Yci-3	Yci-4	Yci-5**
Kc / T (N-m)/rad	25,684	25,683	34,193	34,193	39,335
Bc (N-m)/(rad/s)	31.80	31.80	25.74	25.75	56.68
Mc x T kg -m^2	NA	NA	2.97E-02	2.97E-02	3.55E-02
X(1), (Kcc)	57.483	57.482	89.638	89.674	147.403
X(2), (Alpha_c)	0.553	0.553	0.950	0.950	0.697
X(3)	NA	NA	0.331	0.332	0.231
X(4)	NA	NA	NA	NA	-1.000
X(5)	NA	NA	NA	NA	NA
Cost (db)	-63.77	-63.77	-66.87	-66.87	-69.53

**Note: "Physical Parameters" Mc, Bc, & Kc for Yci-5 are calculated from X(1), X(2), and X(3) through Bilinear transformation

correspond to "physical parameters" being converted to transfer functions through backwards difference unless otherwise noted. For the cases were X(i)'s were tuned directly, Mc, Bc, and Kc were calculated based on the couplings poles, or characteristic equation, and do not reflect values of the coupling's zeros. Figures 44 and 45 show the stability criterion and virtual coupling for three different solutions.

Viewing cost functions of various virtual coupling solutions in table 9 shows that higher order coupling results in lower cost functions, which corresponds to stiffer frequency characteristics. Similarly, inspection of figure 44 shows the expanded higher order virtual couplings do a better job at fitting the stability criterion. Inspecting parameters for solutions Yci-1, Yci-2, Yci-3, and Yci-4 shows that both tuning the physical parameters (Yci-1 & Yci-3) returned the same respective models as independently tuning the coupling's poles (Yci-2 & Yci-4). Stiffer impedance virtual coupling provides a stiffer haptic two–port network. Bode diagrams in figure 45 represent the virtual coupling as an admittance, with lower admittance equating to stiffer virtual coupling. Again the higher order virtual couplings prove to provide slightly stiffer coupling while satisfying the stability criterion. Interesting to note that when one of the second order coupling zeros was independently adjusted (X(1), X(2), X(3), X(4)) the solution converged to a Bilinear transformation mass-spring-damper

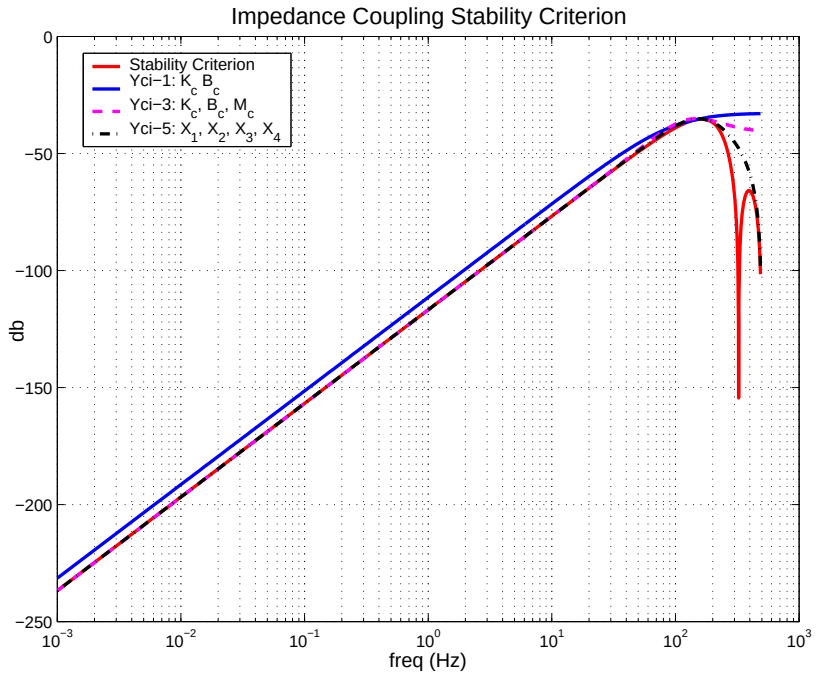

Figure 44: Axis #1 I/A Stability Criterion & Virtual Couplings (without force feedback)

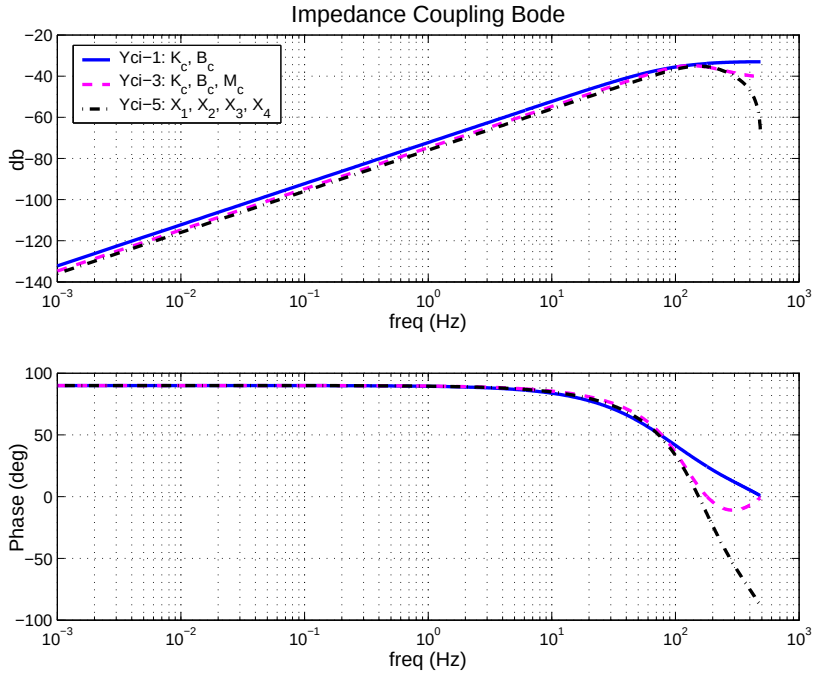

Figure 45: Axis #1 I/A Virtual Coupling Frequency Response (without force feedback)

model (Yci-5). While this solution affords a better cost function, inspection of figure 45 shows both backwards difference and bilinear models are almost equivalent at low frequencies, with bilinear providing slightly stiffer coupling, especially at 300 Hz and above; several orders of magnitude above the human's bandwidth. Independently adjusting both of the coupling's zeros was explored, but it did not result in a better solution.

Remembering that impedance virtual coupling represents the limiting stiffness an impedance network can reflect adds insight to these results. By adding mass to the virtual coupling, mass is added to the limiting impedance and such virtual mass helps increase the allowable stiffness of the maximum impedance while satisfying the stability criterion.

Figure 46 illustrates the network's impedance limits when using the backwards difference based mass-spring-damping virtual coupling model (Yci-3). As expected minimum impedance is equivalent to axis #1's open loop dynamics while maximum impedance is limited by the virtual coupling. Maximum impedance's slope of -20 db/decade signifies the virtual coupling's spring is the dominant dynamics. At approximately 5 Hz the maximum impedance limit crosses over the minimum impedance limit, changes phase, then converges to the minimum impedance limit. This represents a resonance in the haptic controller's maximum stiffness, which is an under damped second order response derived from the combined virtual coupling, actuator dynamics, and device impedance. It will be shown in following sections that this second order response is analogous to the velocity controller's response in the admittance / impedance structure.

7.2 Impedance / Admittance Network – With Force Feedback

By setting the velocity feedback controller, K_v, to zero and only using velocity feed forward in the A/I network, the tuned admittance virtual coupling's inverse can be used as the force controller in the I/A network. In this instance increasing the virtual coupling order beyond

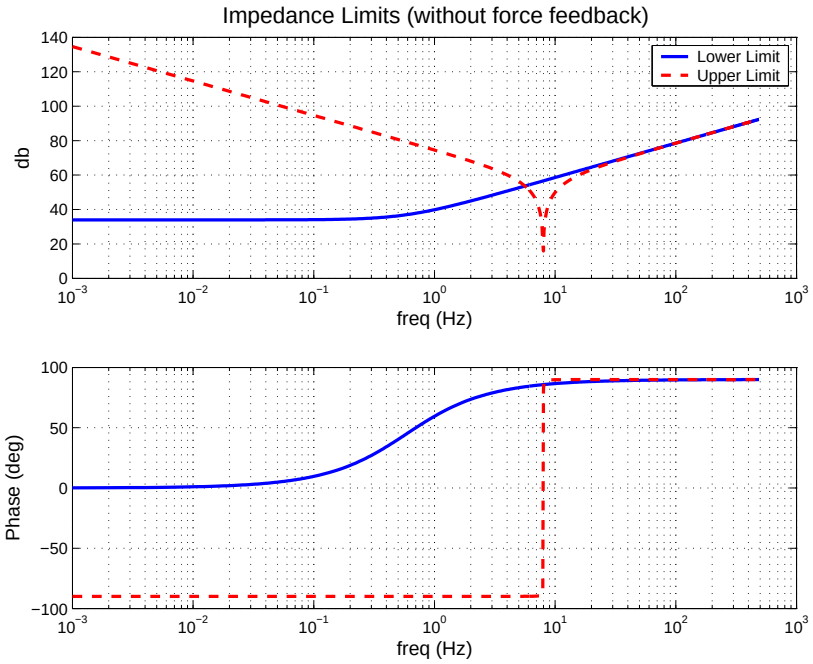

Figure 46: Axis #1 I/A Impedance limits (without force feedback)

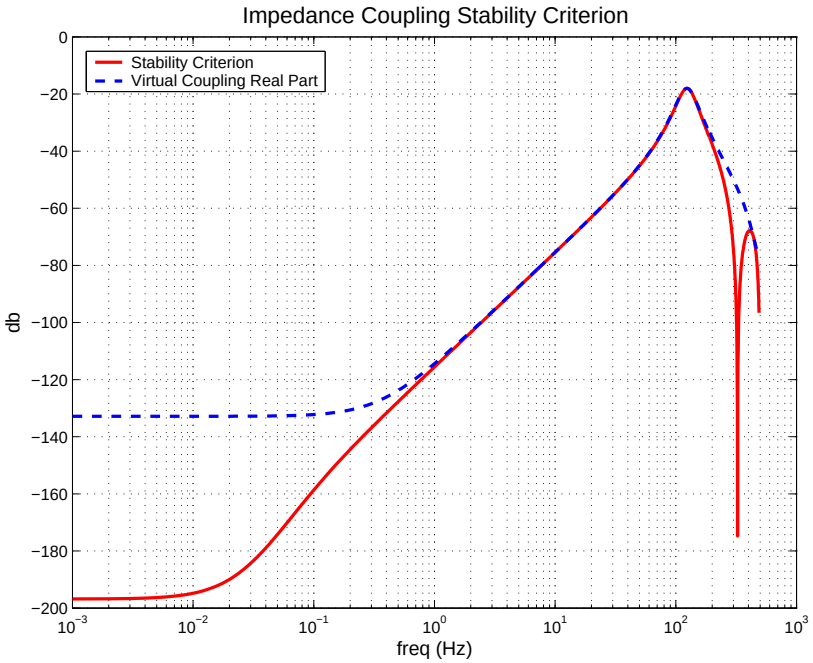

Figure 47: Axis #1 I/A Stability Criterion & Virtual Coupling (with force feedback)

a mass-damper model did not result in a stiffer coupling. In fact solution of higher order coupling models simply reduced to the lower order model. Selected coupling parameters were $M_cT = 1.939$ and $B_c = 213.82$, corresponding to force controller parameters of $K_p = 4.6768x10^{-3}$(N-m)/(N-m) and $K_i = 0.5157$ (N-m)/(N-m-s) (based on backwards difference conversion). Using this force controller in the I/A network results in the virtual coupling stability criterion shown in figure 47. It can be seen that the stability criterion levels off at just above -200 dB ($\approx 10^{-10}$) for low frequencies ($<\approx 10^{-2}Hz$). This can be attributed to the integral action in the force feedback controller and the stability criterion no longer levels out if integral force feedback is removed. Because of this, a low order coupling will not satisfy the stability criterion. Tuning comprised of first fitting a second order coupling for frequencies of approximately 0.1 Hz and above. This model was then added to a real value corresponding to that which the stability criterion converges to at lower frequencies, producing a coupling model which satisfies the stability criterion. This coupling was then used as an initial condition and processed through the tuning algorithm to converge on a better solution for the complete frequency range; resulting in the virtual coupling

$$V_h - V_e^* = Y_{CI}F_e^* = \left(\frac{z^2 - 0.01125z - 0.9887}{54.91(z^2 - 1.221z + 0.7142)}\right)F_e^* \tag{106}$$

that satisfies the stability criterion as illustrated in figure 47. It is interesting to note that though this coupling form is of the most general form, that is the tuning algorithm independently adjusted the zeros and poles, it resembles the second order bilinear transformation model with the zeros slightly adjusted from unity so as to achieve the required lower frequency real part level off. Doing so is equivalent to using a damper, B_S, in series with the virtual coupling stiffness as illustrated in figure 49. Remembering that the force feedback integrator is what caused the stability criterion to level off adds insight to the "optimal" numerical solution. Force relaxation in the virtual coupling is required to compensate for the force controller's low frequency gain and ability to "wind up" with small signals. Allowing the coupling to relax allows it to act like a high pass filter and eliminate static or "DC" force signals that can cause the force integrator's compensation to grow and /or oscillate. While this may be the desired numerical solution, having a damper in series will cause "stress

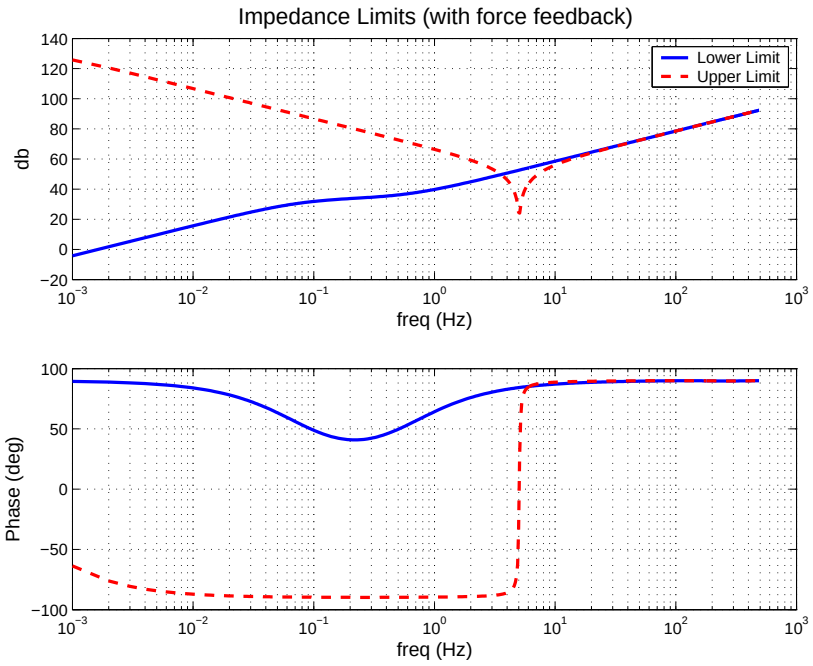

Figure 48: Axis #1 I/A Impedance limits (with force feedback)

relaxation" behavior in the coupling, something that is not desirable when simulating interaction with stiff environments. This coupling form will reappear in I/A two–port network tuning presented in following chapters, while the chapter on experimental implementation will briefly address practicality of having such damping in series with the virtual coupling stiffness.

Using this tuned virtual coupling to complete the impedance / admittance network with a feedback force controller results in the impedance limits illustrated by figure 48. As expected, minimum impedance is no longer limited by the device's open loop dynamics. It appears at low frequencies that the minimum impedance acts like an inertia without damping, signified by the force vs velocity having a phase of +90 degrees and a magnitude slope of +20 db per decade. Again, maximum impedance is limited by the stiffness of the virtual coupling and has a pair of under damped second order zeros near 5 Hz while crossing over the minimum impedance at around 3 Hz. Future sections will directly compare this I/A network utilizing force feedback control with the previous network without force feedback control and with an admittance / impedance network.

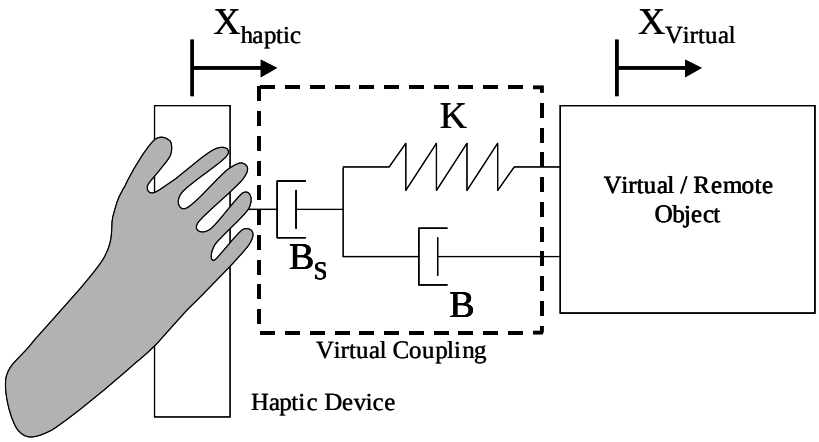

Figure 49: Revised I/A Network Virtual Coupling with B_S

Though the I/A coupling for Axis #1 is not as sensitive, several solutions to the I/A network coupling in proceeding chapters will contain numerator coefficients sensitive to roundoff. As mentioned, this solution model is equivalent to a mass–spring–damper with a second damper converted to it's discrete equivalent through bilinear approximation; with the series damper causing the coupling's zeros to slightly shift from unity. If the required shift is small enough, that is the series damper has very large impedance, then insufficient coupling numerator coefficient significant digits will loose the low frequency leveling effect of the coupling's real part or cause it to level off too high; the first causing the coupling to violate Llewelyn's third stability condition and the latter causing a less desirable performing virtual coupling.

Llewelyn's stability is derived to guarantee passive port interaction when the second port is terminated by any passive one–port. When Llewelyn's third stability condition is violated it does not necessarily mean the network will respond actively when interfaced with all passive environments. In this case the low frequency violation does not cause the network's estimated dynamic impedance limits (Z_{min} & Z_{max}) to be active, but there exists some passive environment impedance that will cause the two–port to have active human–machine interaction at the low frequencies. Range of environment impedance which causes

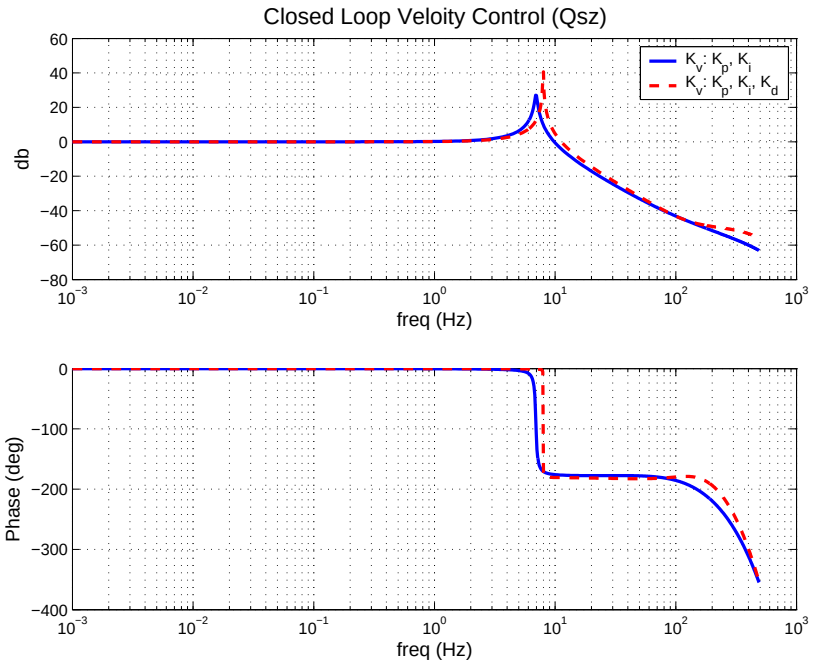

Figure 50: Axis #1 A/I Closed Loop Frequency Response (Q_{sz})

the two–port to interact actively through its human port and the power associated with this active response may be minimal. For example, Axis #1's I/A network's stability criterion levels off at a very low value and at a very low frequency. Magnitude of criterion violation for a coupling that does not level off is minimal in value (less than $\approx 10^{-10}$) and at frequencies with a period greater than $\approx$ 100s. The small violation of Llewelyn's stability criterion will limit the range of environment impedance that causes the network to have an active human–machine interaction. Furthermore, experimental limitations when implementing the two–port networks, such as controller precision, sensor resolution, and non modeled system dynamics, may make such a small violation of Llewelyn's third condition ($<\approx 10^{-10}$) an academic concern and not a practical issue. Future chapters investigating experimental implementation of haptic two–port networks will further discuss this issue.

7.3 Admittance / Impedance Network

As outlined in previous chapters, the virtual coupling of an I/A network without force feedback can be used as the velocity controller in the admittance structure. Therefore, tuning

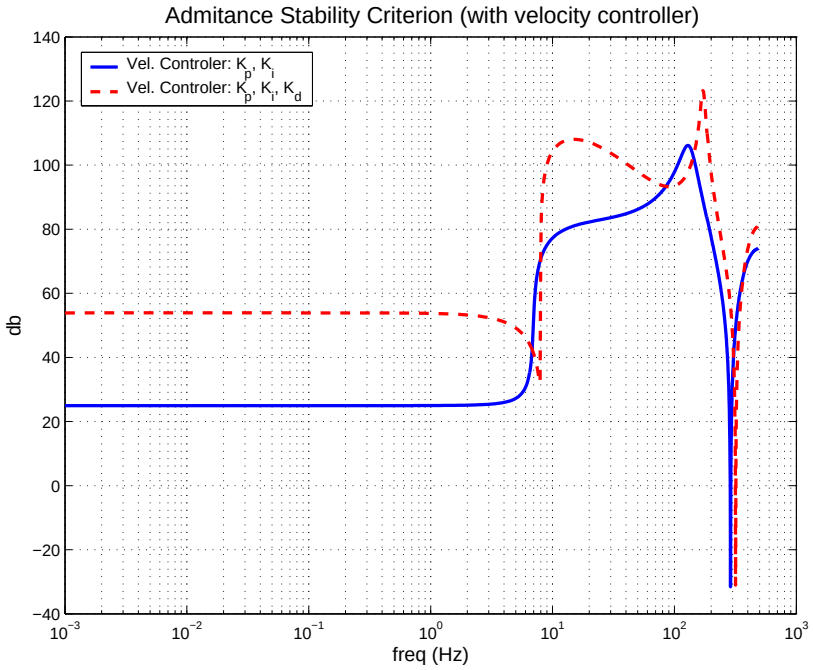

Figure 51: Axis #1 A/I Stability Criterion for Two Velocity Controllers

the virtual coupling for a traditional I/A network that does not utilize force feedback is the equivalent of tuning the A/I network's velocity feedback controller. Hence using the inverse of the virtual couplings shown in table 9 will work for the A/I network's controller. At first one may be inclined to use the inverse of the stiffer virtual coupling because it will afford a stiffer velocity controller, but review of the stiffer higher order impedance virtual couplings in table 9 shows they do not have much more damping than the lower order couplings. Inspecting figure 50 illustrates that using the second order virtual coupling (Yci-3) as the controller results in a less damped closed loop system, with a resonance of ≈ 40 *db* versus a resonance of ≈ 28 *db* for the simple PI velocity controller. Furthermore, inspection of figure 51 shows the stiffer velocity controller causes the stability criterion for the virtual coupling to be higher. Because of this the lower order velocity controller with $K_p = 31.80(N-m)/(\theta/s)$ and $K_i = 25,684(N-m)/\theta$, equivalent to a position controller with gains $K_p = 25,684(N-m)/\theta$ and $K_d = 31.80(N-m)/(\theta/s)$, was chosen.

Inspection of figure 52 shows the stability criterion levels off to approximately 25 db at lower frequencies. As before, coupling was tuned for higher frequencies and then augmented

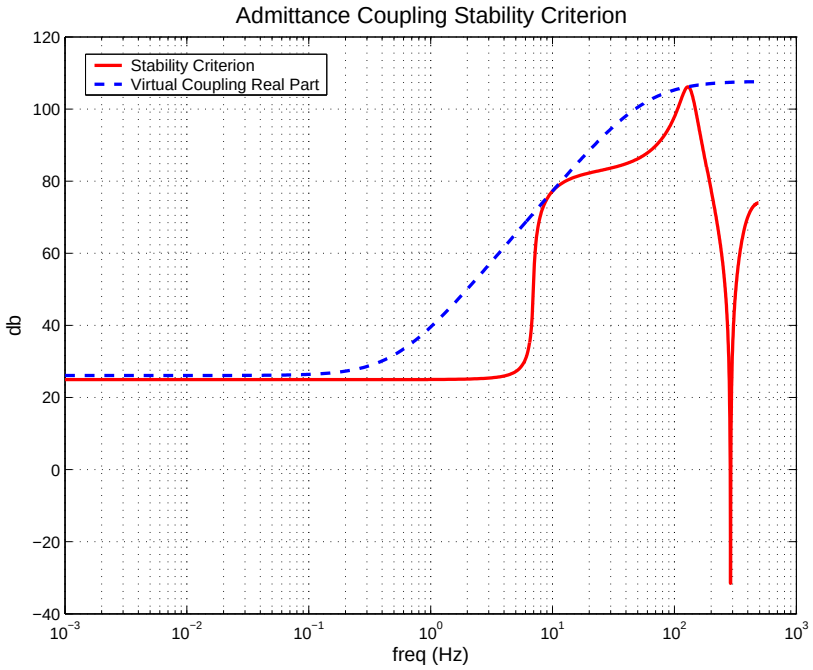

Figure 52: Axis #1 A/I Stability Criterion & Virtual Couplings

by a constant to produce a new estimate to be used as an initial guess in the tuning algorithm, resulting in a virtual coupling of

$$F_h - F_e^* = Z_{CA} V_e^* = \left(\frac{z - 0.99997}{4.9215\text{x}10^{-6}(z - 0.69825)} \right) V_e^* \tag{107}$$

The real part of this virtual coupling can be viewed with the stability criterion in figure 52, while the admittance limits for the completed network can be viewed in figure 53. As expected the minimum admittance exhibits a second order resonance near 6 Hz. Maximum admittance crosses over minimum impedance at approximately 0.7 Hz, changes phase and exhibits an anti–resonant–like dip, then converges to the minimum impedance.

The virtual coupling form of (107) is a reduced form of the most general second order coupling presented in Chapter 5. This specific form of coupling will reappear in the solutions for HuRBiRT's axis #2, #2 B, and #2 EMF A/I networks. Unfortunately this coupling requires considerable significant digits to capture the numerator's effect at leveling out the coupling's real part. Reparameterizing the coupling into its analogous physical form illustrated in figure 54 helps reduce the dependence on significant digits and adds insight

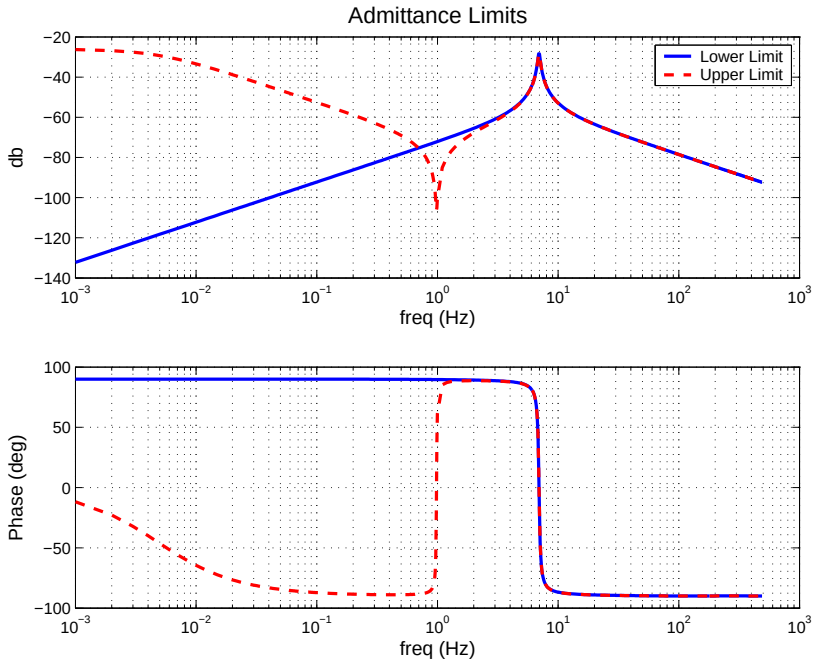

Figure 53: Axis #1 A/I Admittance limits

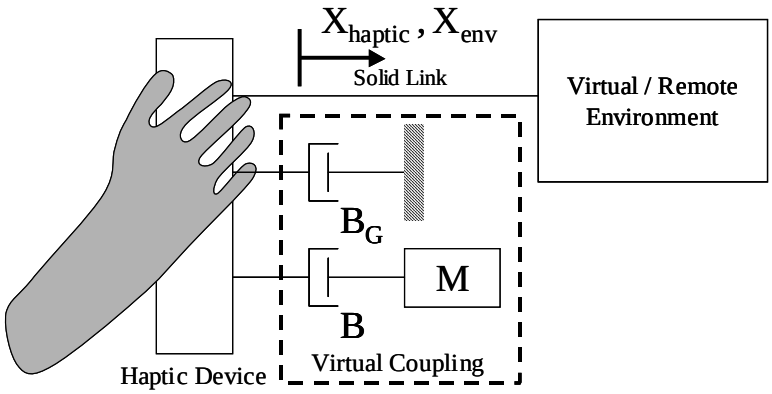

Figure 54: Revised A/I Network Virtual Coupling with B_G

to the solution. Specifically this coupling differs from the coupling illustrated in Chapter 5 by the slight shifting of the coupling's zero from unity through the additional of grounded damper B_G. Using the basic first order coupling listed in Chapter 5, the virtual coupling illustrated in figure 54 can be described by

$$F_h - F_e^* = Z_{CA} V_e^* = \left(\frac{z-1}{K_{cc}(z-\alpha_c)} + B_G \right) V_e^* = \left(\frac{z-\beta}{K(z-\alpha_c)} \right) V_e^* \tag{108}$$

with

$$\begin{aligned} K &= \frac{K_{cc}}{1 + K_{cc} B_G} \quad , \quad \beta = \frac{1 + \alpha_c K_{cc} B_G}{1 + K_{cc} B_G} \\ K_{cc} &= \frac{M_c + B_c}{M_c B_c} \quad , \quad \alpha_c = \frac{M_c}{M_c + B_c} \end{aligned} \tag{109}$$

again with M_c, B_c, and T defined as M/T, B, and discrete controllers sample period respectively. Using values in equation (107) corresponds to values of 673 (Kg–m^2), 290,938 ($^{(N-m)s}/_{rad}$), and 20 ($^{(N-m)s}/_{rad}$) for M, B, and B_G respectively. Because virtual coupling acts as a limit on maximum network admittance, if the interfaced environment's admittance approaches infinity the admittance of the environment / coupling combination, which is the admittance communicated to the operator, will approach the virtual coupling's admittance.

7.4 Comparisons of Final Two–Port Networks Limits

Adding force feedback to the impedance network had several effects on its impedance limits. First, as illustrated in figure 55 it required a more compliant virtual coupling, lowering the network's stiffness by $\approx 38\%$. Second, the force controller lowers minimum impedance to an inertia of ≈ 100 Kg–m^2 at lower frequencies while as the frequency increases the effect of the force controller diminishes. Third, the impedance / admittance network with a force controller has a maximum / minimum impedance limit crossover at aproximately half that of the network without force feedback control.(≈ 3.6 Hz vs ≈ 5.6 Hz)

Comparing the admittance limits of the A/I network to the impedance limits of the I/A network with force feedback shows the two networks are not equivalent. If the two were,

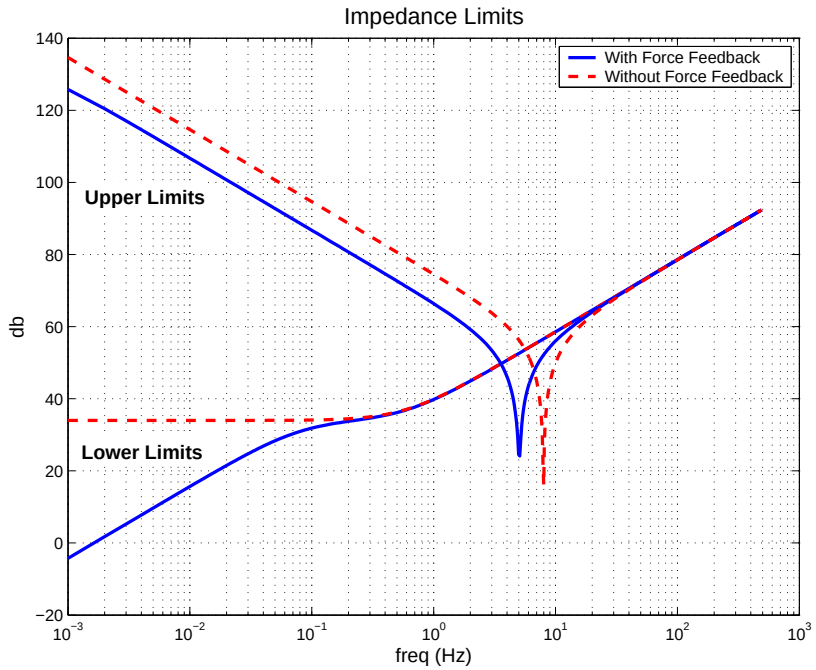

Figure 55: Axis #1 I/A Impedance Limits Comparison (with and without force feedback)

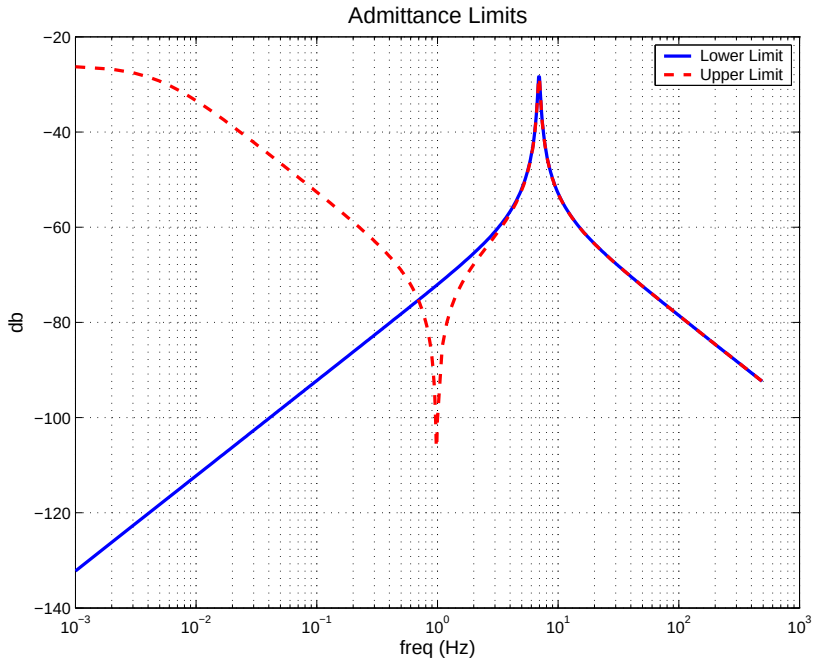

Figure 56: Axis #1 A/I Admittance limits

the maximum admittance of the A/I network would match the inverse (negated in db form) of the minimum impedance of the I/A network and the minimum admittance of the A/I network would match the inverse of the maximum impedance of the I/A network. Instead, the admittance network appears to be a slightly stiffer haptic system while the impedance network appears to be more transparent. A/I network's minimum impedance more closely matches the maximum impedance of the impedance network without force feedback. This should come as no surprise since the impedance network's virtual coupling, without force feedback, was used as the velocity feedback controller. The admittance network has a bandwidth of ≈ 0.7 Hz, the frequency corresponding to the minimum / maximum impedance crossover. This is considerably lower than the bandwidth of either I/A network. Maximum admittance of the A/I network mimics a device with a damping of ≈ 20 (N-m)/(rad/sec) and inertia of ≈ 680 Kg–m^2.

Initially one may conclude the force controller hurt performance, shrinking the impedance range of the device. What is not shown is that much like the velocity controller, the force feedback controller works to improve accuracy of the desired reflected environment. Force is generated through open loop mappings of the actuators in a traditional I/A network without force feedback. Residual friction, device dynamics, or disturbances are not compensated for, unless in an open loop fashion. Adding force feedback helps compensate for such phenomena's that may degrade accuracy. [18] By design, the admittance structure already provides this through the velocity feedback controller.

This tuning of a relatively simple haptic model adds insight to selecting an implementation form for the haptic device. Given the test case it is apparent an A/I network may be better at passively reflecting stiff environments, where as the I/A network may be more suitable at passively reflecting free environments. Furthermore the I/A network allows for a higher bandwidth of impedance limits than the A/I network allows for admittance limits.

CHAPTER 8

HUMAN ARM MODELING

As previously discussed, tuning haptic control systems for an arbitrary human impedance / admittance may be too conservative. Humans, while possessing the potential of mimicking infinite admittance interaction by letting go, can not impart infinite impedance on the haptic device. Chapter two lists three models for human arm interaction with haptic devices which were developed for use with specific haptic devices. Different devices that require different human arm configurations and muscles will afford different interaction models. because of this, these previously published models will not be used with HuRBiRT's network tuning, but rather this chapter will present a more complicated human arm model based on splitting the arm's dynamics into the arm's natural impedance and the human's cognitive compensatory response to position perturbations. This two part model will first be used to describe experimental frequency data for one human subject's arm impedance response to position perturbations. Following this the derived model will be incorporated into tuning of the haptic networks for HuRBiRT's axis #1 so that effects of including said human impedance limit models can be observed.

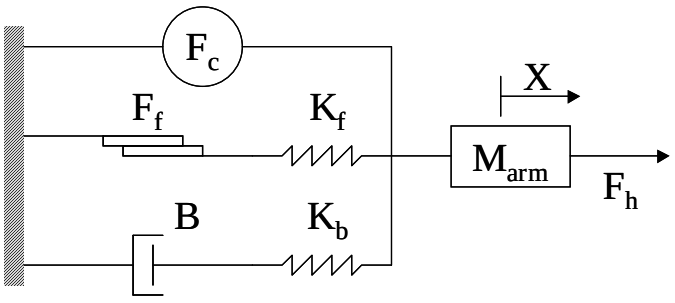

Figure 57: Human Arm / Shoulder Dynamic Model

8.1 Biomechanical Model

The human body is a complex nonlinear system and biomechanical modeling is an area of continuing research. Human's interaction with haptic devices will contain elements which are functions of both biomechanics and the human's "closed loop" controller. Many biomechanical models looking at mechanical properties of muscle elements often use various viscoelastic elements, such as Maxwell, Voigt, and Kelvin relaxation models, while friction, or slider, elements are often used in modeling plastic–elastic deformation of materials. [44] Besides the muscular stiffness and relaxation properties, a human's arm has inertia while the human adds cognitive resistance based on their control intentions and capabilities.

One such method of combining these elements is illustrated in figure 57. M_{arm} represents limb mass while F_c represents the human's force control on his or her limb. Elements K_b and B represent a Maxwell viscoelastic element while F_f and K_f represent a plastic–elastic deformation element. Elements F_c, F_f, and B are all grounded to the human body, while X and F_h represent position and force of the limb's endpoint. For example, if modeling an arm's gross movement X and F_h would correspond to the hand while F_c, F_f, and B would be grounded to the shoulder. If modeling control of a computer mouse while resting the arm on the table, X and F_h would correspond to the hand while F_c, F_f, and B would be grounded to the arm's wrist. One method of describing figure 57 is with a frequency based input output equation of

$$\frac{F_h(j\omega)}{X_h(j\omega)} = (j\omega)^2 m_{arm} + \frac{(j\omega)K_b B}{(j\omega)B + K_b} + \frac{jK_f F_f}{jF_f + K_f} + \frac{F_c(j\omega)}{X_h(j\omega)} \tag{110}$$

As with modeling friction in HuRBiRT's frequency response, a modified version of the describing functions covered in Appendix A are used to describe the plastic–elastic deformation element. This modeling problem can be separated into its respective elements by modeling the limb's dynamics separate from the human's control action. Following sections will use this model to describe experimental frequency input / output data for the human arm interacting with HuRBiRT's axis #1.

Table 10: Estimated Human Arm Model Parameters

Parameter	Units	Value
m_{arm}	Kg	3.36
K_f	N/m	85
F_f	N	78.1
K_b	N/m	123
B	N/(m/s)	24.1

8.2 Arm's Mechanical Dynamics

Using a digital PD position controller for axis #1 with a proportional and derivative gain of 1,500 (N-m)/(rad) and 65 (N-m)/(rad/s) respectively, HuRBiRT was sent various chirp position reference signals while the author held on to the force sensing handle. The author did not try to resist or aid in arm movement, but rather let the arm naturally move with the handle while sitting beside the device. Total of 33 data sets were collected with the chirp signals' maximum frequency content ranging from 0.2 to 10 Hz and amplitude of link rotation ranging from 20 to 4 degrees; corresponding to commanded perturbation of the handle ranging from 33.5 cm to 7 cm for the various chirp signals. Using DFT algorithms and frequency domain cross correlation averaging to help remove any signal remnants, the output (force in newtons) versus input (disturbance in meters) frequency response was calculated. Parameters in equation (110), with F_c set to zero, were solved for to best describe the experimentally determined response, resulting in the model fit illustrated in figure 58 which uses parameters listed in table 10.

Surprisingly, the biomechanical model does an excellent job at describing the data. Model mass of 3.36 kg is within 10% of rough measurements of the subject's arm mass with a scale. As expected, the low frequency magnitude response is dominated by the plastic–elastic deformation model, which also adds frequency independent phase. This corresponds to the arm's noninertial resistance to movement. Though the human may not consciously resist motion or try to return the arm from perturbation, some muscular resistance to movement is present unless the subject actively tries to regulate interaction force by matching

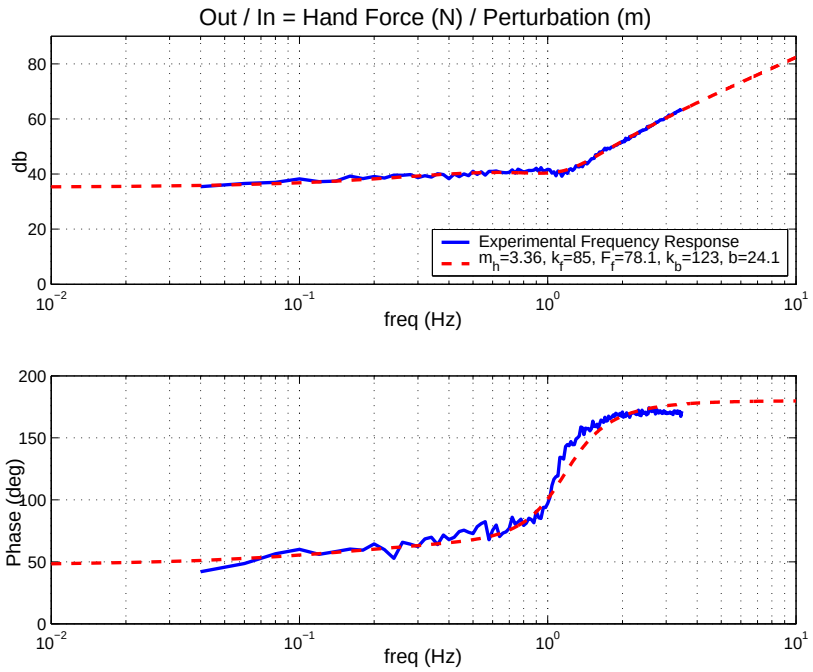

Figure 58: Human Arm's Non Cognitive Frequency Response to Chirp Perturbations

handle movement. As frequency increases the arm's mass begins to dominate the frequency response, signified by the +40 db per decade magnitude response and the phase shifts to 180°. While based on first principle models this is expected, it is interesting to note that this happens just above 1 Hz.

8.3 Cognitive Compensatory Dynamics

Using the same digital position controller utilized for collecting frequency response data of the arm's impedance, HuRBiRT was sent various digitally low pass filtered white noise perturbation signals while the author attempted to consciously resist motion. A total of 28 data sets were collected with varying input amplitudes and filter cut off frequencies ranging from 0.5 to 5 Hz. Low pass filtering was used to limit the frequency content well above the human or HurBiRT's controller bandwidth and to allow collection of low frequency human "controlled" impedance without high frequency perturbations corrupting or confusing the human. Again, using DFT algorithms and frequency domain cross correlation averaging to help remove any signal remnants, the output (force in newtons) versus input (disturbance

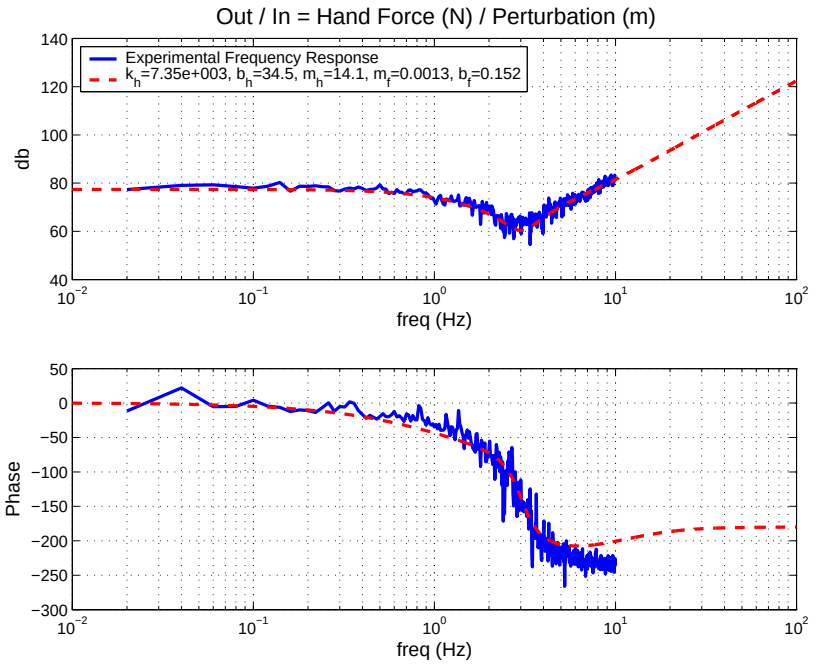

Figure 59: Human's Cognitive Frequency Response to White Noise Perturbations

in meters) frequency response was calculated and can be viewed in figure 59.

While the human's actual control action is not necessarily linear, one possible linear approximation is

$$\frac{F_c(s)}{X(s)} = \frac{m_c s^2 + b_c s + k_c}{m_F s^2 + b_F s + 1} \tag{111}$$

Equation (111) is equivalent to a PID velocity controller with second order high frequency attenuation. Attenuation was added to the PID controller because the human does not have infinite bandwidth. While collecting data the author observed stiff human control at low frequencies was common, but as frequency increased control effort diminished. As described in chapter 2, even though the subject wanted to regulate position, once signals exceeded the human's bandwidth the subject could not physically respond or "keep up". Using this control model to augment the previously derived arm model as outlined by equation (110) and table 10 results in the total arm / human control model illustrated in figure 59, figure 60, and table 11. Parameters used to describe the experimental data result in a second order underdamped controller (numerator dynamics) with a natural frequency of ≈ 2.5 Hz and damping ratio of 0.054. Attenuation parameters result in two first order filters, the first

Table 11: Estimated Human Compensatory Controller

Parameter	Units	Value
m_c	Kg	14.0660
b_c	N/(m/sec)	34.4694
k_c	N/m	7,348
m_F	NA	0.0013
b_F	NA	0.1518

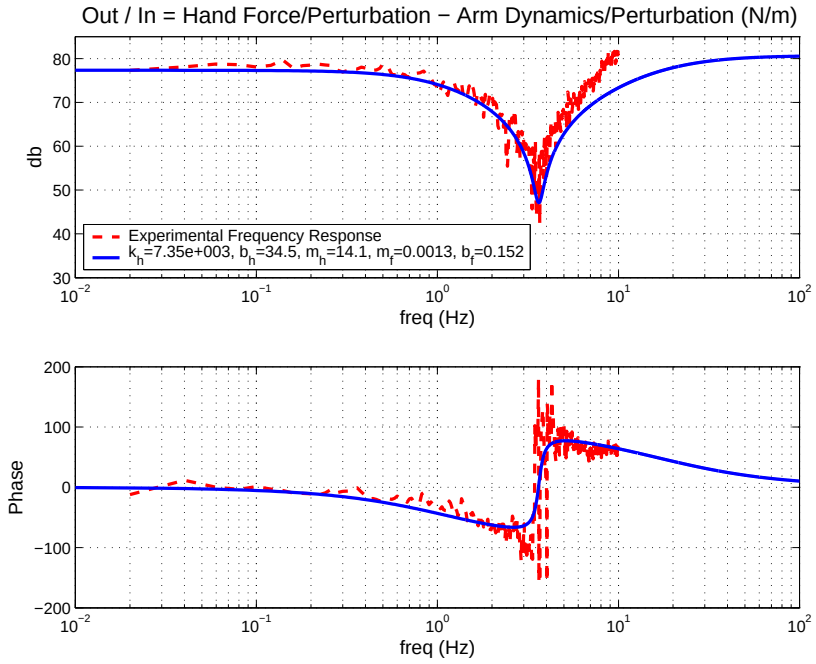

Figure 60: Estimated Human Compensatory Controller Frequency Response to White Noise Perturbations

having a corner frequency of ≈ 1.1 Hz and the second at ≈ 17.5 Hz. Figure 60 illustrates the experimental response with the aforementioned arm model subtracted and the assumed human control model ($F_c(s)$) based on equation (111).

Inspecting figure 59 shows the model does a fairly good job at describing the experimental data. Several important properties of the frequency response are worth noting. First, at low frequencies the subject acted like a stiff spring, but stiffness began to roll off with a 3db drop at ≈ 0.9 Hz. This is slightly lower than the estimation of 1.6 Hz mentioned in Chapter 2 for human's maximum compensatory bandwidth to random signals. Second, above 3 Hz

the response's magnitude is dominated by the arm mass, though phase lag temporarily exceeds 180° with the model returning to 180° as frequency continues to increase. Because the data and model use position as the input, to use with passivity analysis they must first be appropriately transformed to use velocity as the input. Doing so will further increase phase lag by 90° and cause the experimental data and describing model to have phase lag ranging from 90° to just past 270°; such lag will violate passivity criterion. Remembering that white noise is not a smoothly varying signal, adds insight to why this frequency response data has said lag. Because the human is responding without a priori knowledge of the perturbation, the human's causal response will naturally lag. As frequency increases the human's phase lag will increase to the point that he / she can no longer control, subsequently lightening up on control effort and allowing arm dynamics to take over.

8.4 Cognitive Compensatory With Pursuit Dynamics

The previous section presented data for one subject's impedance response to white noise perturbations. Because white noise is not a smoothly varying signal it is difficult for the human to predict perturbations and can only respond to the disturbances. What if a smoother signal was used to record the human / haptic device interface impedance? Using the same digital position controller utilized for collecting frequency response data of the arm's impedance, HuRBiRT was sent various chirp position reference signals while the author attempted to consciously resist motion. A total of 47 data sets were collected with the chirp signals' maximum frequency content ranging from 0.2 to 10 Hz. Using DFT algorithms and frequency domain cross correlation averaging to help remove any signal remnants, the output (force in newtons) versus input (disturbance in meters) frequency response was calculated. Figure 61 compares the authors frequency impedance response to such chirp signals with the previously presented white noise signals.

When reacting to chirp perturbations the impedance response appears stiffer at low

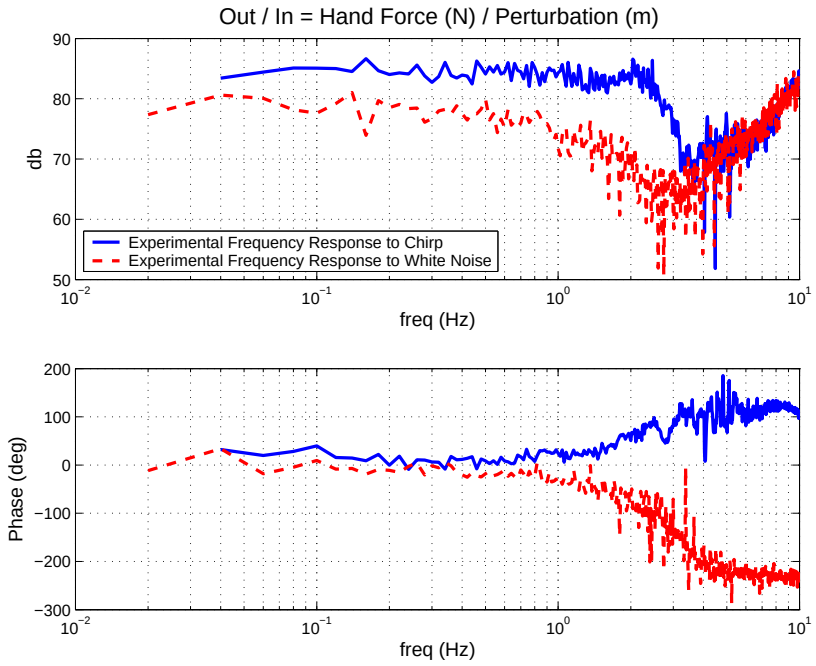

Figure 61: Human's Cognitive Response to Perturbations

frequencies and has a higher bandwidth than the experimental response to white noise perturbations. For example the impedance response to chirp perturbations has a 3 db drop at $\approx$ 3.6 Hz as opposed to $\approx$ 0.9 Hz for when responding to white noise perturbations. Furthermore, phase lag of the impedance response to chirp perturbations does not have any phase lag, but rather phase lead. As mentioned it is hypothesized the human can augment compensatory control with some pursuit control because the chirp signal is smoother and easier to predict. Indeed the author noticed that when responding to chirp perturbations it was much easier to pick up on the the pattern of chirp signal's frequency sweep and predict / adapt up until the subject's bandwidth was exceeded and the subject could not "keep up".

Two models for describing the human cognitive response to chirp perturbations are explored. First model is similar to that used for describing the cognitive response to white noise perturbations. Using the previously derived arm dynamics (equation (110) with parameters in table 10)and an assumed human impedance control model of

$$\frac{F_c(s)}{X_c(s)} = \left(\frac{m_c s^2 + b_c s + k_c}{m_F s^2 + b_F s + 1}\right)\left(\frac{e^{t_d s}}{\tau s + 1}\right) \tag{112}$$

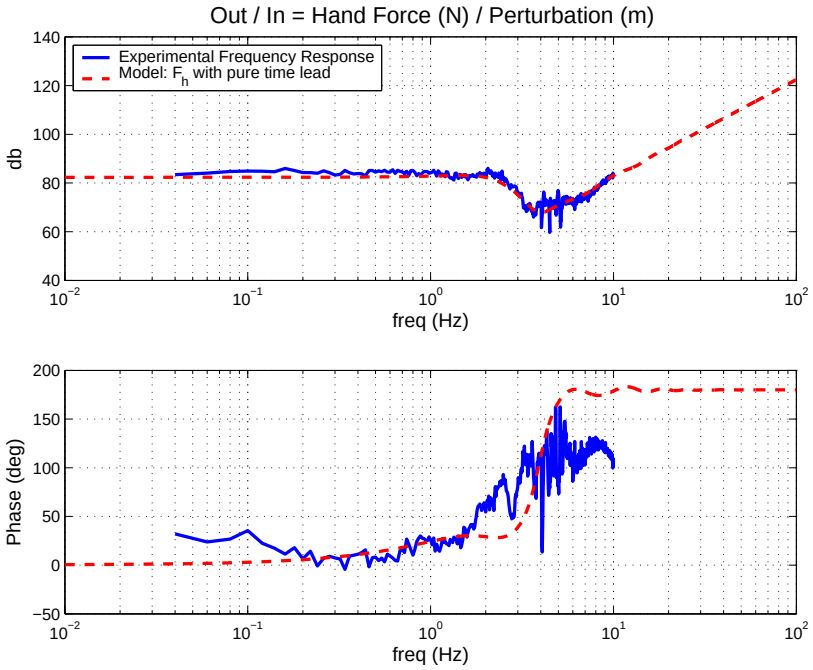

Figure 62: Human's Compensatory & Pursuit Frequency Response to Chirp Perturbations

with parameters listed in table 12 results in the human model illustrated in figure 62. Much like the previous human control model described by equation (111), equation (112) is based on a PID velocity controller with second order attenuation. Added to this is a first order low pass filter with a pure time lead. Parameters used to describe the experimental data result in a second order under damped controller (numerator dynamics) with a natural frequency of ≈ 5.8 Hz and damping ratio of 0.0044. Attenuation parameters result in a second order filter with a natural frequency of ≈ 2.3 Hz and damping ratio of 0.466. The additional first order filter has a corner frequency of ≈ 11.8 Hz with a time lead of 0.154 seconds. As illustrated in figure 62 this model does an excellent job at describing magnitude of the response, but is not as accurate at describing phase.

Another alternative is to ignore predetermined arm dynamics and simply model the human's response with a second order impedance equivalent to

$$\frac{F_h(s)}{X_h(s)} = ms^2 + bs + k \tag{113}$$

It's worth noting this is equivalent to the structure used by both Hogan and Kosuge in

Table 12: Human's Estimated Compensatory & Pursuit Controller

Parameter	Units	Value
m_c	Kg	9.6741
b_c	N/(m/sec)	3.1613
k_c	N/m	13,044
m_F	NA	0.0048
b_F	NA	0.0646
t_d	sec	0.1540
τ	NA	0.0135

Table 13: Estimated Linear Human Arm Model Parameters

Parameter	Units	Hogan	Kosuge	Hannaford	Tognetti
m	Kg	0.8	1.95	NA	6
b	N/(m/sec)	5.5	2.46	300	110
k	N/m	568	55	1,000	10,000
ω_n	Hz	4.24	0.85	0.53*	6.5
ζ	NA	0.13	0.12	NA	0.225

*Note: Value represents a first order corner frequency instead of second order natural frequency.

their human arm dynamic models. Figure 63 uses this model with a mass of 6 Kg, damping of 110 N/(m/sec), and stiffness of 10,000 N/m; corresponding to second order dynamics with a natural frequency of $\approx$ 6.5 Hz and a damping ratio of 0.225. This mass is about twice that used in the arm model previously presented while stiffness is approximately 75% that of the more complicated model utilizing arm's natural dynamics and F_c. Like the more complicated model this simplified second order model does a better job at describing magnitude than phase.

Table 13 lists values for the linear human arm models presented in Chapter 2 along with the simplified model presented in this section. Again, the different models were derived from experimental data taken from different devices. Size of the device and configuration of the subject's arm when interfacing with the device are not necessarily the same. Furthermore, different experimental methods were used for determining said models. For example Hogan's model represents precognitive response to perturbations, Kosuge's model

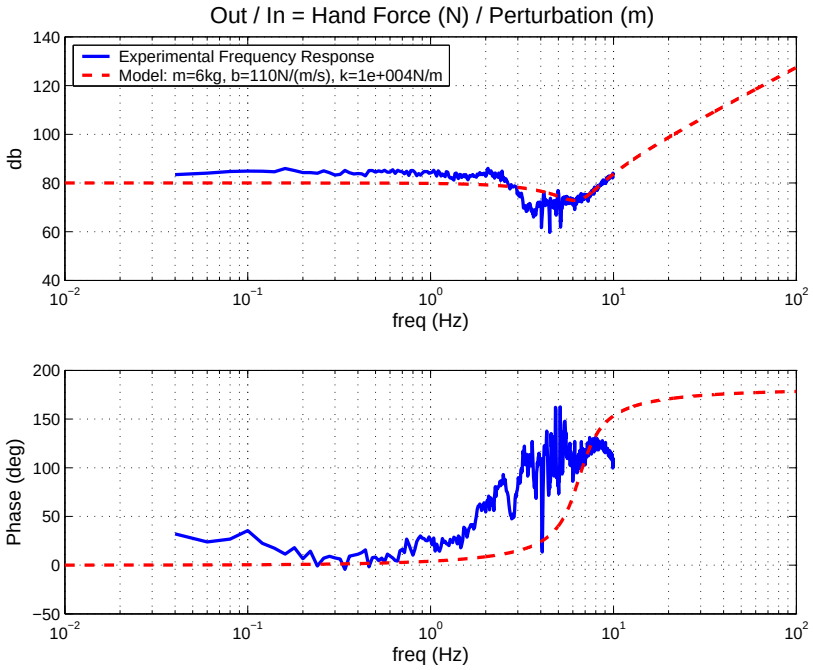

Figure 63: Human's Compensatory & Pursuit Frequency Response to Chirp Perturbations (linear model fit)

represents cognitive compensatory response, while simplified second order model presented in this section represents cognitive pursuit response. Hannaford does not clarify how their model is developed. Still it is interesting to compare these models for insight on the human's bandwidth, stiffness, and damping characteristics.

Both of these models used for describing the human subject's impedance to chirp perturbations will be incorporated into the structure of the two–port networks for HuRBiRt's axis #1. Controller and virtual coupling parameters will be selected for these two–port networks and the final systems will be compared with the networks previously tuned for axis #1 in past chapters.

8.5 Human Model Effects on Two–Port Tuning

Incorporating human impedance / admittance limits into the two–port networks' formulation through the human limit model architecture outlined in chapter 2 results in an "effective" two–port network for tuning. Block reduction of the new A/I and I/A networks which incorporate human impedance limit, Z_h, or its inverse human admittance limit, $Y_h = 1/Z_h$, results in the following A/I and I/A two–port network equations.

$$\begin{bmatrix} V_h(j\omega) \\ F_e^*(e^{j\omega T}) \end{bmatrix} = \begin{bmatrix} H(j\omega) + Y_h(j\omega) & -Q(j\omega) \\ M(j\omega) & Z_{CA}(e^{j\omega T}) \end{bmatrix} \begin{bmatrix} F_h(j\omega) \\ -V_e^*(e^{j\omega T}) \end{bmatrix} \tag{114}$$

$$\begin{bmatrix} F_h(j\omega) \\ -V_e^*(e^{j\omega T}) \end{bmatrix} = \begin{bmatrix} \frac{G(j\omega)}{1+G(j\omega)Y_h(j\omega)} & \frac{P(j\omega)}{1+G(j\omega)Y_h(j\omega)} \\ \frac{-D(j\omega)}{1+G(j\omega)Y_h(j\omega)} & \frac{D(j\omega)P(j\omega)Y_h(j\omega)}{1+G(j\omega)Y_h(j\omega)} + Y_{CI}(e^{j\omega T}) \end{bmatrix} \begin{bmatrix} V_h(j\omega) \\ F_e^*(e^{j\omega T}) \end{bmatrix} \tag{115}$$

Human limits incorporated in the A/I network shows up as a modification to the haptic device's physical admittance, adding compliance. Doing so may relax passivity requirement on $H(j\omega)$, which may allow increasing stiffness of the feedback velocity controller. Incorporating human limits in the I/A network modifies each two–port mapping term; most notably an offset term is added to the lower diagonal term (p_{22}), effectively adding virtual coupling to the model. Even with an infinitely stiff programmed virtual coupling ($Y_{CI} = 0$), the two–port network has some "effective" coupling with respect to satisfying Llewelyn's stability criterion. Similar to before, it can be shown that the inverse tuning method previously outlined in chapter 5 for selecting the feedback controllers applies to these "effective" two–port networks.

8.6 Impedance / Admittance Network – Using Human Models

Incorporating human limits previously presented through pursuit human models allows for a PI force controller with $K_p = 0.1111$ (N-m)/(N-m) and $K_i = 2.3$ (N-m)/(N-m-s) (based on backwards difference conversion); proportional and integral gains ≈ 24 times

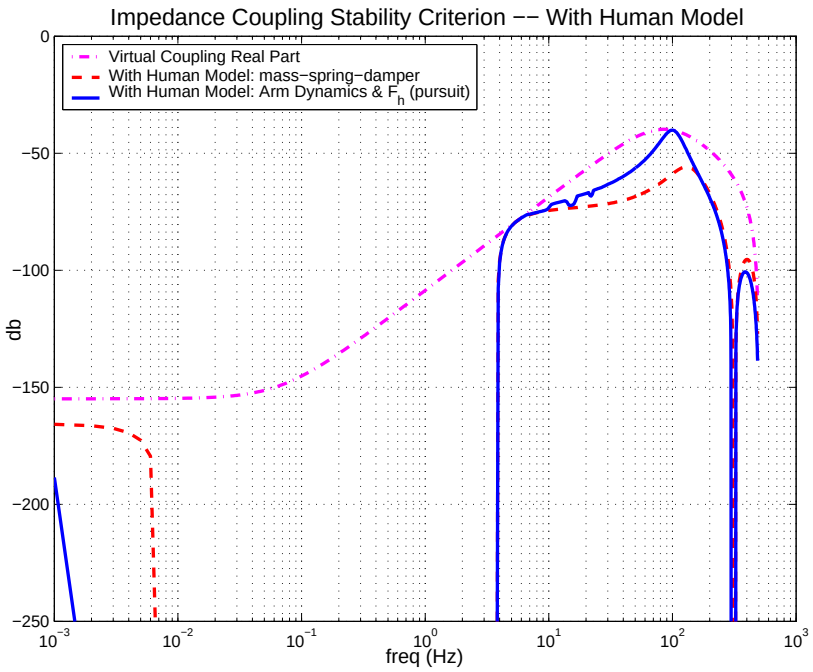

Figure 64: Axis #1 H I/A Stability Criterion & Virtual Coupling

and $\approx$ 4.5 times stiffer than when the human model was not incorporated. Figure 64 shows the resulting stability criterion for both the more complicated pursuit model and the simple second order model. At high frequencies the more complicated model results in a more stringent stability criterion than the simple second order model, but at low frequencies the second order model results in a more restrictive stability criterion. Both models' stability criterion drop off for a limited frequency range, which, as outlined in equation (115), corresponds to when the human model effects add enough effective virtual coupling to satisfy Llewelyn's stability criterion without any programmed virtual coupling . Completing the virtual coupling results in a coupling of

$$V_h - V_e^* = Y_{CI} F_e^* = \left(\frac{z^2 + 1.5481 \times 10^{-7} z + 0.999999}{325(z^2 - 1.205z + 0.403)} \right) F_e^* \tag{116}$$

and a final two–port network with impedance limits illustrated in figure 65. At low frequencies minimum impedance mimics a mass while the maximum impedance mimics a grounded spring. Future sections will compare this network with one which did not utilize human impedance limits when tuning feedback and coupling parameters.

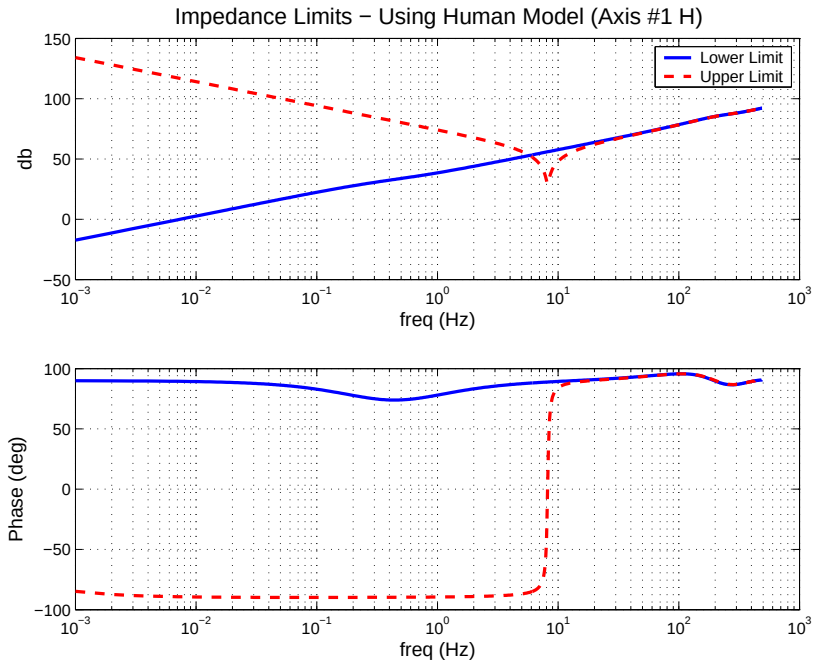

Figure 65: Axis #1 H I/A Impedance Limits

8.7 Admittance / Impedance Network – Using Human Models

Figure 66 illustrates the stability criterion for selecting the A/I network's velocity controller when using both pursuit human models and the stability criterion for when human models are not incorporated; again, this is equivalent to the virtual coupling stability criterion for the I/A network without feedback force control. At frequencies below ≈ 6 Hz the stability criterion drops off, signifying the network satisfies Llewelyn's stability criterion for those frequencies without any programmed virtual coupling. As in the previous chapter, velocity control was kept as a simple backwards difference PI velocity controller; specifically a digital PI controller with $K_p = 1,230(N-m)/(\theta/s)$ and $K_i = 169,400(N-m)/\theta$, equivalent to a PD position controller with gains $K_p = 169,400(N-m)/\theta$ and $K_d = 1,230(N-m)/(\theta/s)$. This position controller uses proportional and damping gains 6.6 and 38.7 times stiffer than the position controller allowed when human impedance limits were not utilized. Completing the network in figure 23 with a virtual coupling of

$$F_h - F_e^* = Z_{CA} V_e^* = \left(\frac{z - 0.999999}{1.206 \times 10^{-5}(z - 0.600)} \right) V_e^* \tag{117}$$

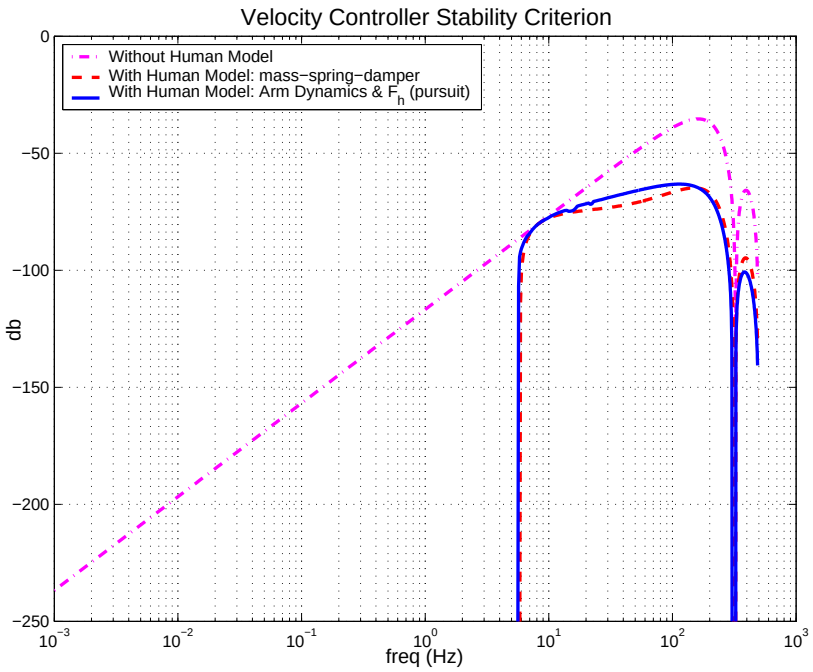

Figure 66: Axis #1 A/I Velocity Controller Stability Criterion (using human model)

results in a A/I network with admittance limits illustrated in figure 67. At low frequencies maximum and minimum admittance mimic a mass and grounded spring respectively.

Alternatively if the velocity controller was relaxed 71%, specifically a digital PI velocity controller with $K_p = 879(N-m)/(\theta/s)$ and $K_i = 121,000(N-m)/\theta$, equivalent to a PD position controller with gains $K_p = 121,000(N-m)/\theta$ and $K_d = 879(N-m)/(\theta/s)$, the admittance coupling stability criterion is relaxed.Completing the network in figure 23 with a virtual coupling of

$$F_h - F_e^* = Z_{CA}V_e^* = \left(\frac{z - 0.999999}{5.102 \times 10^{-5}(z - 0.688)}\right) V_e^* \tag{118}$$

results in a two–port A/I network with admittance limits illustrated in figure 67. Future sections will directly compare both of these networks with the previously tuned A/I networks which did not utilize a human model.

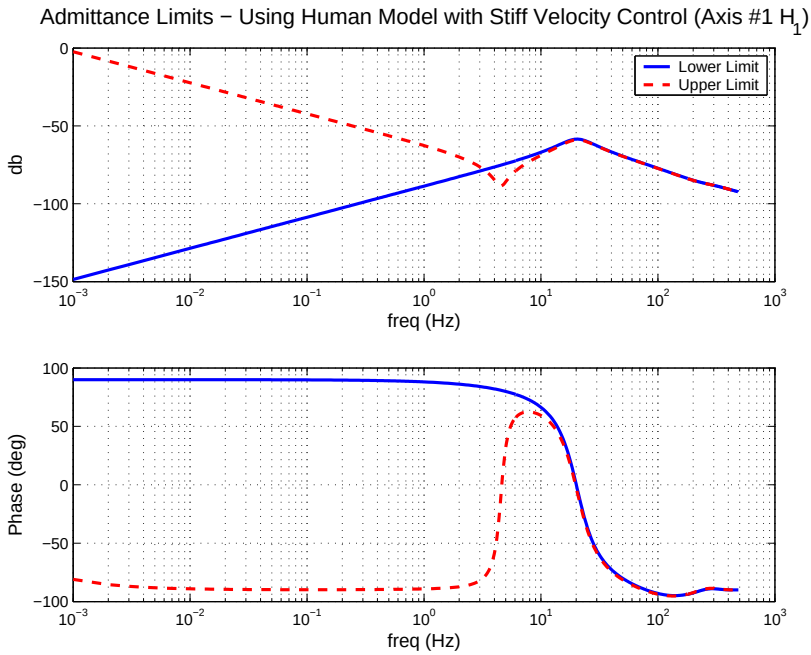

Figure 67: Axis #1 H_1 A/I Admittance Limits (with human model)

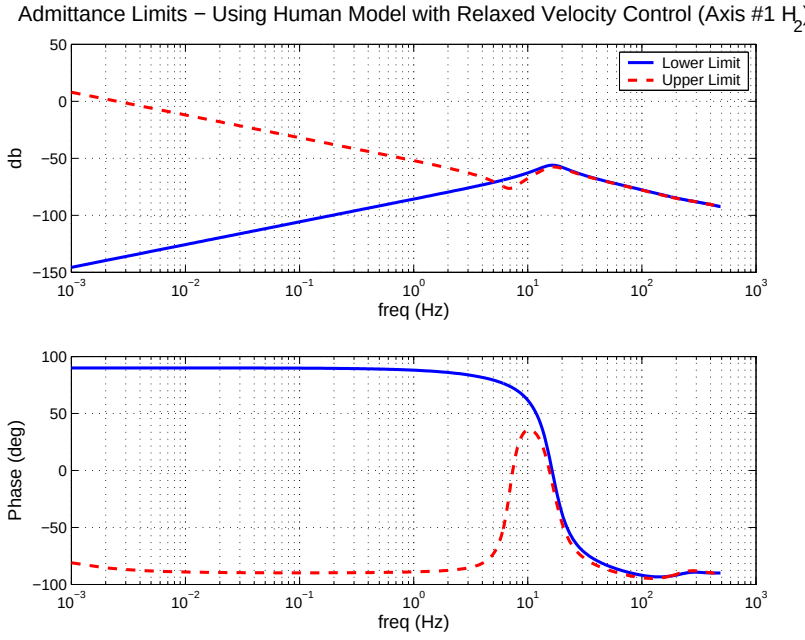

Figure 68: Axis #1 H_2 A/I Admittance Limits (with human model)

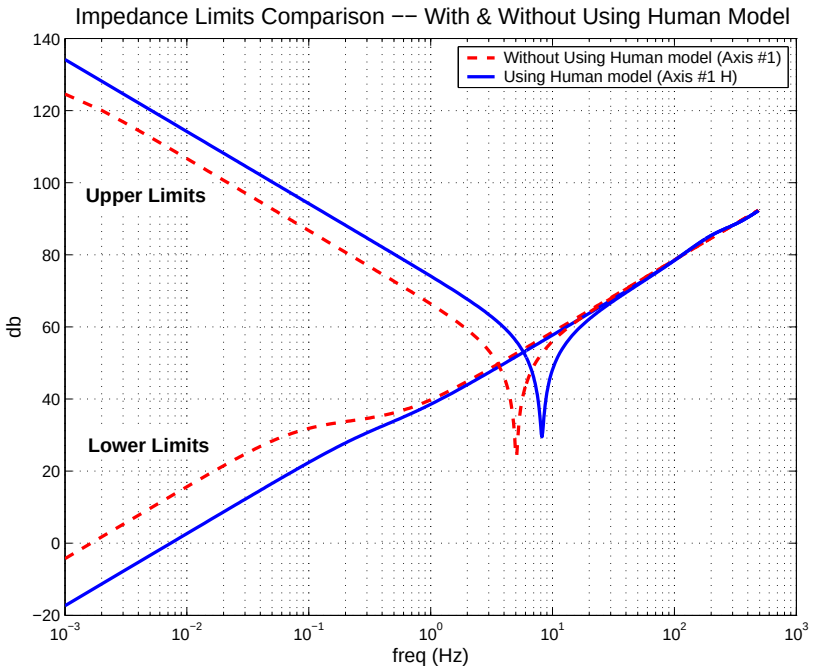

Figure 69: Axis #1 & Axis #1 H I/A Impedance Limits Comparison

Table 14: I/A Network Parameters for Axis #1

Axis	**#1**	**#1 H**
Force Controller		
K_p $\left({}^{(N-m)}/_{(N-m)}\right)$	4.6768×10^{-3}	1.111×10^{-1}
K_i $\left({}^{(N-m)}/_{(N-m)s}\right)$	0.5157	2.30
Virtual Coupling		
Transfer Function	(106)	(116)
X_1	54.91	325
X_2	1.221	1.205
X_3	0.7142	0.403
X_4	1.125×10^{-2}	-1.548×10^{-7}
X_5	-0.9887	-0.999999
Physical Parameters		
M $\left({}^{(N-m)s^2}/_{rad}\right)$	2.01×10^{-2}	1.06×10^{-1}
B $\left({}^{(N-m)s}/_{rad}\right)$	7.847	97.013
K $\left({}^{(N-m)}/_{rad}\right)$	13,547	32,143
B_S $\left({}^{(N-m)s}/_{rad}\right)$	$\approx 2.7 \times 10^6$	$\approx 7.6 \times 10^7$

Table 15: A/I Network Parameters for Axis #1

Axis	**#1**	**#1** H_1	**#1** H_2
Position Controller			
K_p $\left({}^{(N-m)}/_{rad}\right)$	25,684	169,400	121,000
K_d $\left({}^{(N-m)s}/_{rad}\right)$	31.8	1,230	879
Virtual Coupling			
Equation	(107)	(117)	(118)
K	4.922×10^{-6}	1.206×10^{-5}	5.102×10^{-5}
α	0.698	0.600	0.688
β	0.99997	0.999999	0.999999
Physical Parameters			
M $\left({}^{(N-m)s^2}/_{rad}\right)$	673	207	62.8
B $\left({}^{(N-m)s}/_{rad}\right)$	290,938	138,198	24,489
B_G $\left({}^{(N-m)s}/_{rad}\right)$	20	0.207	0.0628

8.8 Comparison of With and Without Human Models

Figure 69 compares the impedance limits of the I/A two–port networks derived with and without use of the human limits. A network utilizing human limits allowed stiffer feedback force control which translates into better transparency. Low frequency minimum impedance of the new network mimics an inertia of ≈ 22 Kg–m^2 as opposed to ≈ 100 Kg–m^2 for the network which did not utilize human limits. Stiffness of the new network is ≈ 2.4 times stiffer with a low frequency stiffness of 32,174 (N-m)/(rad) as apposed to a stiffness of 13,575 (N-m)/(rad). Another property of the new network is a higher impedance bandpass, the cross over of minimum & maximum impedance limits; specifically a crossover frequency of ≈ 5.8 Hz as opposed to ≈ 3.6 Hz.

Figure 70 compares the admittance limits of the A/I two–port networks derived with and without use of the human limits. As already noted, incorporating human impedance limits allows for stiffer velocity / position control which translates into lower minimum admittance. Interesting enough, slightly lowering the stiffness of the feedback controller allows for a less restrictive virtual coupling and broader overall network admittance limits.

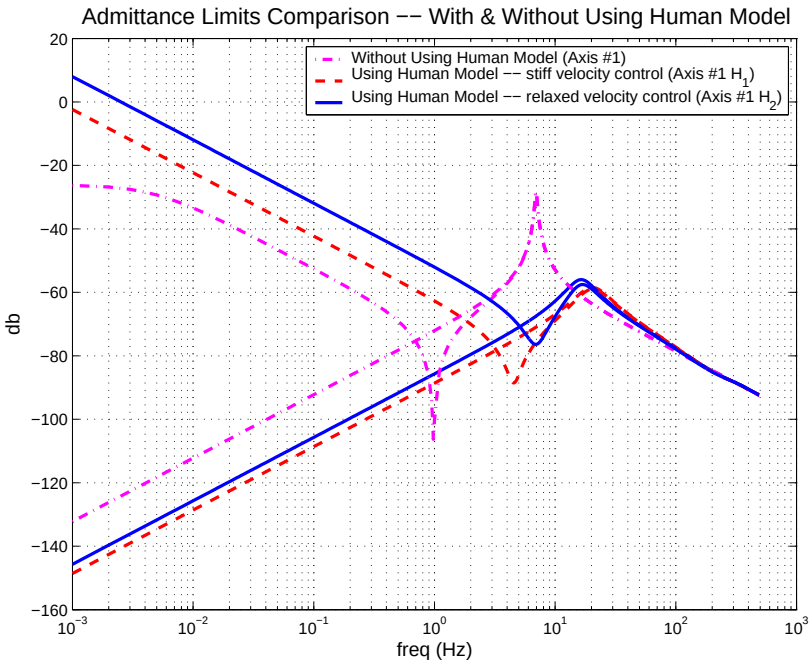

Figure 70: Axis #1, Axis #1 H_1, & Axis #1 H_2 A/I Admittance Limits Comparison

Whereas the network that does not utilize human limits has a maximum admittance which mimics a mass of 680 Kg–m^2 with damping of 20 (N-m)/(rad/sec), the network utilizing human impedance limits and stiff feedback control mimics an inertia of ≈ 207 Kg–m^2 and the network with slightly softer feedback control mimics an inertia of ≈ 63 Kg–m^2. Network bandpass, the cross over of minimum & maximum admittance limits, are higher for the networks utilizing human impedance limits; specifically ≈ 0.7 Hz for the network not utilizing human limits, ≈ 3.3 Hz for the network utilizing human limits and stiff feedback control, and ≈ 5.1 Hz for the network utilizing human limits and slightly softer feedback control.

Through utilizing the human model limits in the tuning it is shown that feedback control can be stiffened and virtual coupling relaxed so as to increase the impedance / admittance range of the device. Human model limits essentially add compliance to the network modeling, lowering the required compliance from feedback control and virtual coupling. It is hypothesized the human model's affect on network tuning is highly related to the physical

damping within the human model. Preceding chapters will explore the effects of directly incorporating additional damping within the haptic device. Complete modeling of a human's behavior in contact with a mechanical device is not realistic and derived human models are very device specific. Humans are highly variable, adaptive, and complex. Different devices which require different human arm / hand configurations, use different muscles, and require different magnitudes of motion will all result in different specific human impedance limit models. Though completely accurate modeling of the human is not a realistic goal, performing a few system identification experiments and developing a device specific human impedance / admittance limit model to be used in conjunction with the networks, human characteristics can be incorporated into the tuning so as to add insight without knowing the complete human model.

CHAPTER 9

HYBRID SYSTEMS / DESIGNING PHYSICAL DISSIPATION

Passive haptic devices and passive control of active devices are briefly introduced in Chapter 1 while Chapter 2 goes into more detail on passivity control of two–port networks. What if the inherent passivity of the device was increased by design; primarily what if energy dissipation was designed into the device? As described in Chapter 1, if this energy dissipation was through an adjustable dissipating actuator in parallel with the force controller, the haptic device would become a hybrid active / passive system. How would the addition of such an actuator affect tuning of the two–port network? Though such dissipative actuators could utilize "intelligent control" to provide resistive forces directly related to desired reflected force, this would create a nonlinear over actuated control problem. If instead the dissipative actuator were used as an adjustable damper, traditional linear theory can be used to determine it's affect on two–port tuning. Approaching the hybrid parallel active / passive device with the two–port network paradigm allows use of analysis tools developed in preceding chapters to analyze the system's performance and stability. Inspection of the I/A Llewelyn stability condition in Chapter 4 shows that if the real part of $G(j\omega)$ is increased through additional damping, the required real part of $Y_{CI}(e^{j\omega T})$ decreases. On the flip side, increasing damping also increases open loop impedance and can change the transparency of the device. Similarly, manipulating equations in Chapter 4 for the A/I network show that when the angle of $Z_d(j\omega)$ approaches zero, or the device is purely dissipative without mass or energy storage, the stability criterion is lowered.

Where as Chapter 7 outlined tuning of HuRBiRT's axis #1, this chapter will outline tuning of A/I and I/A two–port networks for three cases of axis #2; with the first case corresponding to not using of the magnetic rheological brake as a programmable damper

(axis #2), the second case corresponding to using the brake (axis #2 B), and the third case corresponding to not using the brake, but implementation of EMF damping (axis #2 EMF). As in Chapter 7, both impedance / admittance and admittance / impedance networks will be illustrated. Many of the patterns and techniques previously outlined in tuning the coupling / feedback controller for axis #1 directly apply to axis #2.

9.1 Selecting EMF Damping Parameters

While selection of the electric damping parameters discussed in Appendix B could be structured into an optimal tuning problem, such detail in selecting said parameters will not be addressed in this research. Instead, simple velocity and force controllers were tuned for various A/I and I/A networks utilizing EMF damping to see what combination of EMF damping parameters allowed for the stiffest controllers. Doing so resulted in an electric damping resistor of $R_b = 1$ ohm and an electric damping corner frequency of 30 Hz. Using the electrical parameters for axis #2's electric motors and the above EMF damping parameters results in a high pass damping term of

$$\frac{\mathrm{B_{EMF}}}{\mathrm{rad/sec}} = \frac{3.148 \times 10^{-2}\mathrm{s}}{5.305 \times 10^{-3}\mathrm{s} + 1} \tag{119}$$

which augments the the physical impedance of the device. This corresponds to an additional high frequency damping of ≈ 5.9 (N-m)/(rad/s). Similarly, these parameters result in a lag–lead motor dynamics of

$$\frac{\mathrm{I_m}}{\mathrm{I_c}} = \frac{2.721 \times 10^{-3}\mathrm{s} + 1}{5.305 \times 10^{-3}\mathrm{s} + 1} \tag{120}$$

which attenuates current to the motor by $\approx 50\%$. While increasing electric damping resistance increases electric damping, it also increases the lag–lead's attenuation, something that could hurt low frequency performance if the corner frequency is set too low. Similarly, increasing high frequency lag–lead attenuation helps decrease the high frequency stability criterion, which allows for higher damping in the position controller and stiffer proportional gain in the force controller. Considering that backwards difference velocity estimation can produce noisy signals at higher frequencies and therefore noisy control signals, this is not

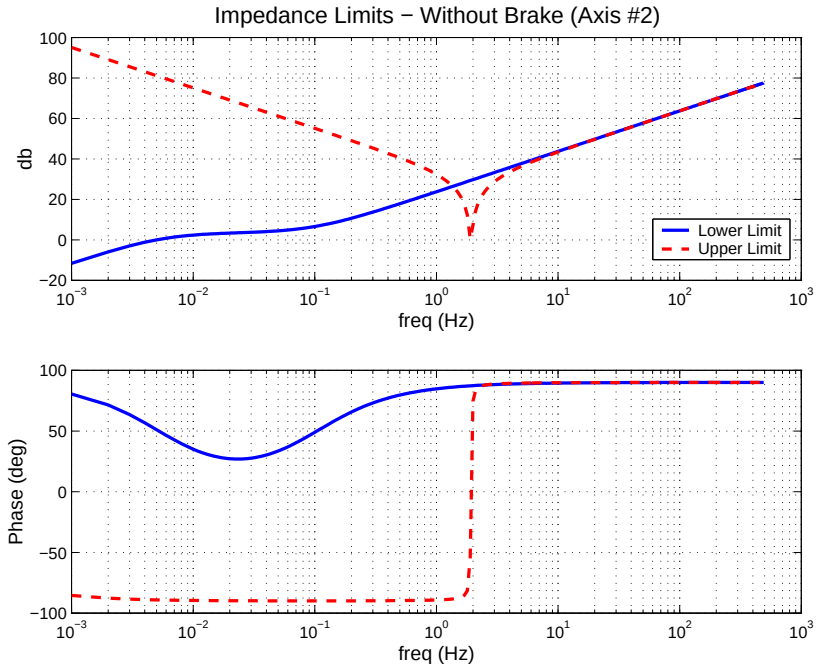

Figure 71: Axis #2 I/A Impedance Limits

very surprising. Selecting the electric damping parameters is a trade off between increasing lag–lead attenuation, increasing high frequency damping, and lowering corner frequency of high pass EMF damping. While the parameters selected above are based on models previously outlined in Chapter 6, experimental testing may reveal that unmodeled dynamics, such as backlash, higher order modes, etc may play a prevalent role when selecting EMF damping parameters.

9.2 Impedance / Admittance Two–Port Network – Without Brake

Residual friction and damping of axis #1 without the brake is relatively low, making the open loop dynamics of the device fairly transparent. Tuning the force controller for this system results in a PI controller with $K_p = 8.0736 \times 10^{-4}$ (N-m)/(N-m) and $K_i = 0.0351$ (N-m)/(N-m-s) (based on backwards difference conversion), not a very stiff feedback controller. As with axis #1, when using force feedback the stability condition for virtual coupling levels

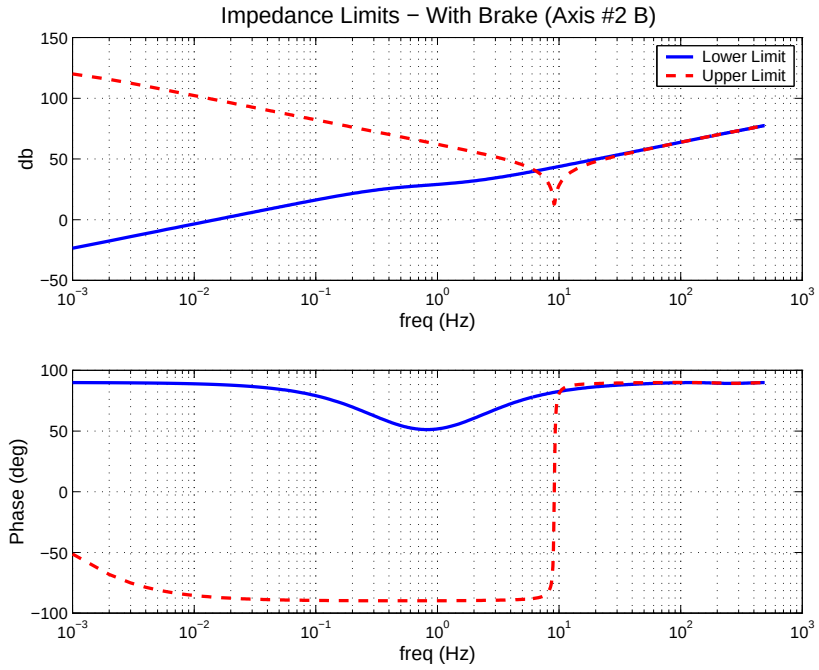

Figure 72: Axis #2 B I/A Impedance limits

off at low frequencies. Using techniques oulined in previous chapters a virtual coupling of

$$V_h - V_e^* = Y_{CI} F_e^* = \left(\frac{z^2 - 0.009413z - 0.990586}{1.367(z^2 - 1.233z + 0.756)} \right) F_e^* \tag{121}$$

is fit to the stability criterion, resulting in a two–port network with impedance limits illustrated in figure 71. Inspection of the network's impedance limits show, as expected, the force controller is not very stiff and only affects the device's transparency at very low frequencies. Worth noting are the number of significant digits in the virtual coupling's numerator (equation (121)) are rather high. As discussed in previous chapters, this is required to preserve the stability criterion at low frequencies. If rounded to lower significant digits than maximum impedance is compromised or the stability criterion is violated at $\approx 7 \times 10^{-4}$ Hz. While this may be considered too low of a frequency to be representative of the physical system, one can argue it represents the stability criterion as signals approach DC.

9.3 Impedance / Admittance Two–Port Network – With Brake

Chapter 6 list the estimated damping for axis #2 B (with brake) to be ≈ 17.7 times higher than without use of the brake as a damper. Tuning the force controller for this system

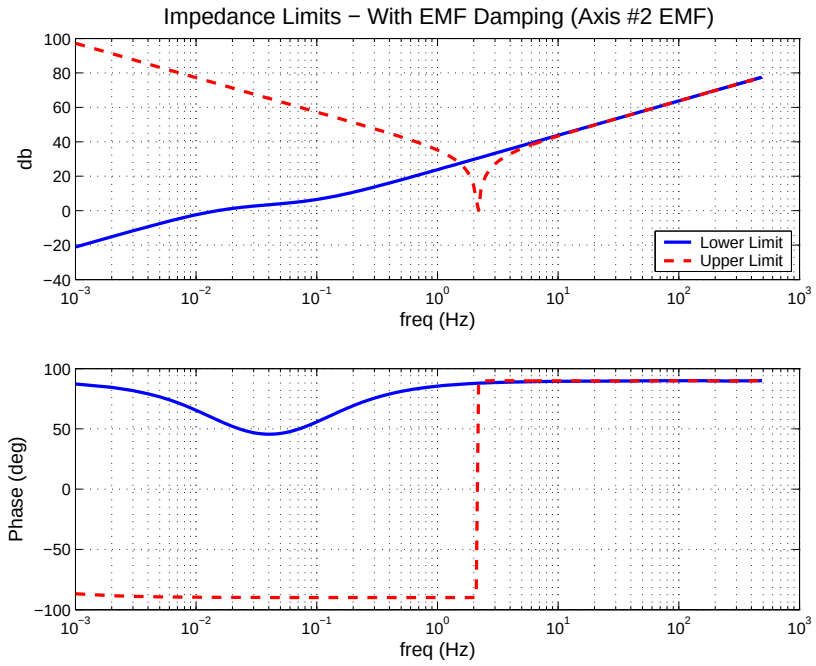

Figure 73: Axis #2 EMF I/A Impedance Limits

results in a PI controller with $K_p = 0.0128$ (N-m)/(N-m) and $K_i = 2.50$ (N-m)/(N-m-s) (based on backwards difference conversion). Increased damping allowed stiffer force control than without use of the brake as a programmable damper, specifically proportional gain is 15.86 times stiffer and integral control is 71.2 times higher. As with axis #1 and #2 the stability condition for virtual coupling levels off at low frequencies. Fitting the virtual coupling to satisfy the stability criterion while minimizing coupling magnitude produces a coupling of

$$V_h - V_e^* = Y_{CI} F_e^* = \left(\frac{z^2 - 0.01302z - 0.98697}{34.6(z^2 - 1.20z + 0.666)} \right) F_e^* \tag{122}$$

resulting in a two–port network with impedance limits illustrated in figure 72. As expected the shape of this network's impedance limits mimics that of the I/A network for axis #1 and #2.

9.4 Impedance / Admittance Two–Port Network – With EMF Damping

Equation (119) estimates that EMF damping increases high frequency damping by $\approx 5\times$ and equation (120) attenuates high frequency motor current by $\approx 50\%$. Tuning the force controller for this system results in a PI controller with $K_p = 7.62 \times 10^{-3}$ (N-m)/(N-m) and $K_i = 0.1056$ (N-m)/(N-m-s) (based on backwards difference conversion). EMF damping allowed slightly stiffer force control than without its use, specifically the proportional gain is 9.4 times stiffer and integral control is 3.0 times higher. Again the stability condition for virtual coupling levels off at low frequencies. Fitting the virtual coupling to satisfy the stability criterion while minimizing coupling magnitude produces a coupling of

$$V_h - V_e^* = Y_{CI} F_e^* = \left(\frac{z^2 - 6.130 \times 10^{-5} z - 0.999938}{3.678(z^2 - 1.113z + 0.362)} \right) F_e^* \tag{123}$$

resulting in a two–port network with impedance limits illustrated in figure 73.

9.5 Admittance / Impedance Two–Port Network – Without Brake

As with axis #1, velocity control was kept as a simple backwards difference PI velocity controller; specifically a digital PI controller with $K_p = 0.954(N-m)/(\theta/s)$ and $K_i = 771(N-m)/\theta$, equivalent to a PD position controller with gains $K_p = 771(N-m)/\theta$ and $K_d = 0.954(N-m)/(\theta/s)$, was chosen. As before the stability criterion levels off at low frequencies. Again, minimizing coupling magnitude while satisfying stability criterion, results in a virtual coupling of

$$F_h - F_e^* = Z_{CA} V_e^* = \left(\frac{z - 0.999998}{2.787 \times 10^{-5}(z - 0.873)} \right) V_e^* \tag{124}$$

and a two–port network with admittance limits illustrated in figure 74. As with axis #1 the A/I network's limits mirror the I/A network's limits, with the A/I network having lower bandwidth, slightly higher stiffness, and less transparency.

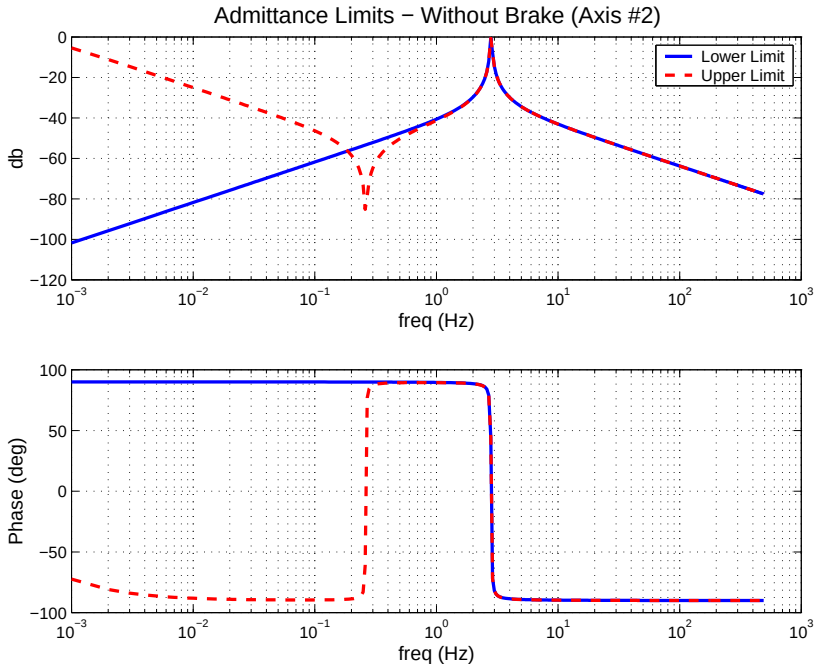

Figure 74: Axis #2 A/I Admittance Limits

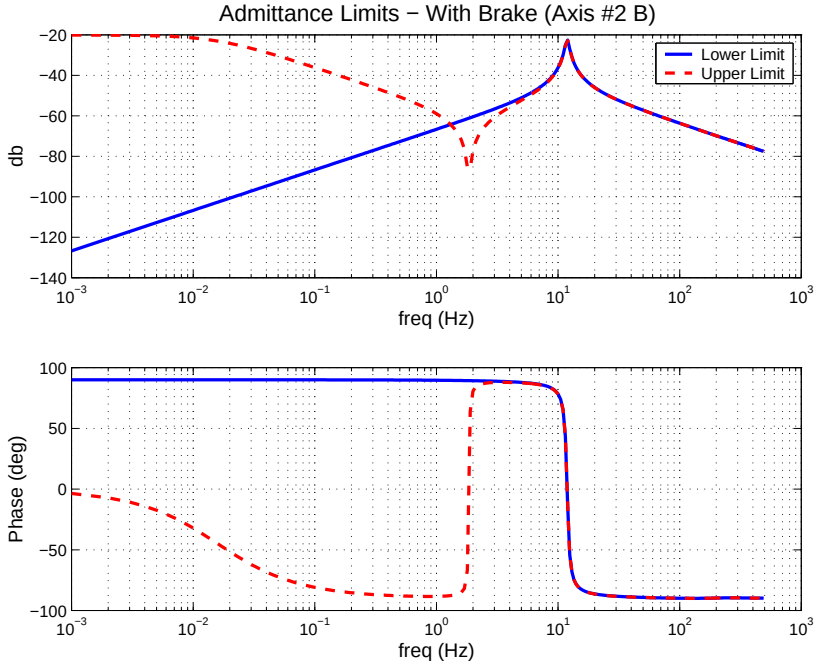

Figure 75: Axis #2 B A/I Admittance Limits

9.6 Admittance / Impedance Two–Port Network – With Brake

Again, velocity control was kept at a simple backwards difference PI velocity controller; specifically a digital PI controller with $K_p = 16.85(N-m)/(\theta/s)$ and $K_i = 13,613(N-m)/\theta$, equivalent to a PD position controller with gains $K_p = 13,613(N-m)/\theta$ and $K_d = 16.85(N-m)/(\theta/s)$, was chosen. These controller parameters are 17.7 times greater than without use of the brake. Remembering that the velocity controller is derived through the impedance structure without force feedback and that the resulting impedance stability criterion is scaled by the device's damping. Again, minimizing coupling magnitude while satisfying stability criterion results in a virtual coupling of

$$F_h - F_e^* = Z_{CA} V_e^* = \left(\frac{z - 0.9999}{2.53 \times 10^{-5}(z - 0.607)} \right) V_e^* \tag{125}$$

and a two–port network with admittance limits illustrated in figure 75.

9.7 Admittance / Impedance Two–Port Network – With EMF Damping

Velocity control was selected as a digital PI controller with $K_p = 13.08(N-m)/(\theta/s)$ and $K_i = 1,667(N-m)/\theta$, equivalent to a PD position controller with gains $K_p = 1,667(N-m)/\theta$ and $K_d = 13.08(N-m)/(\theta/s)$. EMF damping allowed slightly stiffer velocity control than without its use, specifically proportional gain (position damping) is 13.7 times greater and integral control (position stiffness) is 2.16 times higher. Minimizing coupling magnitude while satisfying stability criterion results in a virtual coupling of

$$F_h - F_e^* = Z_{CA} V_e^* = \left(\frac{z - 0.999999}{4.815 \times 10^{-5}(z - 0.7237)} \right) V_e^* \tag{126}$$

and a two–port network with admittance limits illustrated in figure 76.

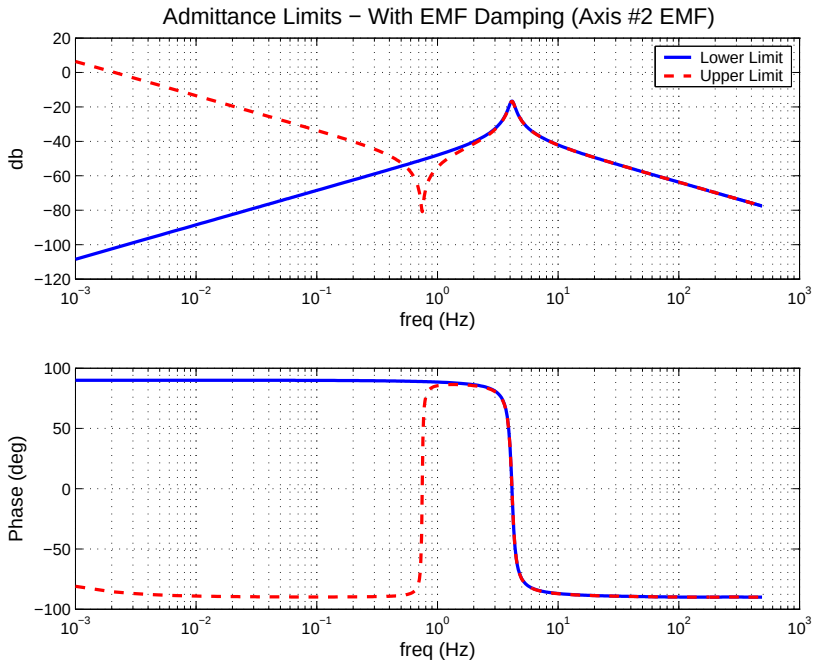

Figure 76: Axis #2 EMF A/I Admittance Limits

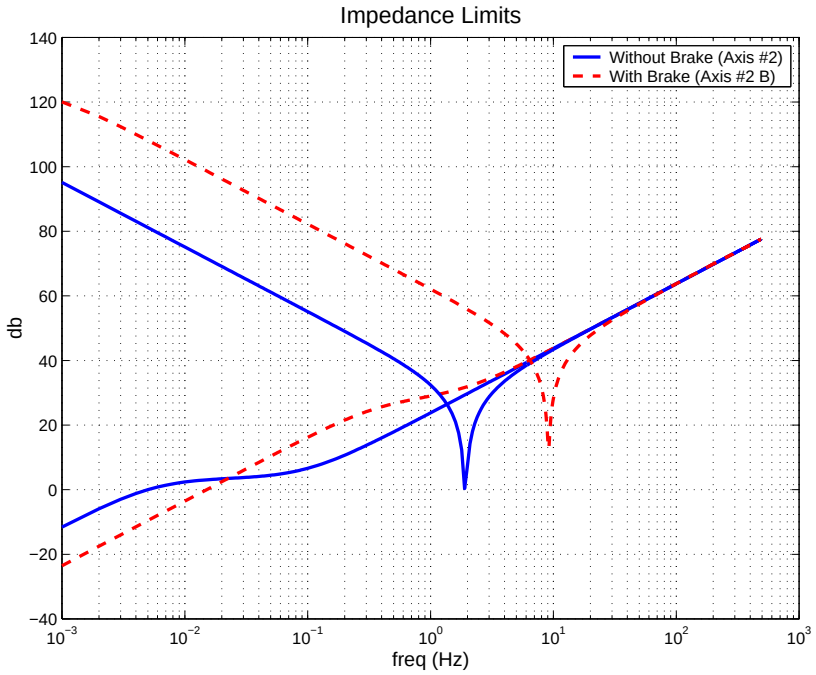

Figure 77: Axis #2 & #2 B I/A Impedance Limits Comparison

Table 16: I/A Network Parameters for Axis #2, #2 B, & #2 EMF

Axis	**#2**	**#2 B**	**#2 EMF**
Force Controller			
K_p $\left({}^{(N-m)}/_{(N-m)}\right)$	8.0736×10^{-4}	1.28×10^{-2}	7.62×10^{-3}
K_i $\left({}^{(N-m)}/_{(N-m)s}\right)$	0.0351	2.50	0.1056
Virtual Coupling			
Transfer Function	(121)	(122)	(123)
X_1	1.367	34.6	3.678
X_2	1.233	1.20	1.113
X_3	0.756	0.666	0.362
X_4	9.413×10^{-3}	1.302×10^{-2}	6.130×10^{-5}
X_5	-0.990586	-0.98697	-0.999938
Physical Parameters			
M $\left({}^{(N-m)s^2}/_{rad}\right)$	5.11×10^{-4}	1.24×10^{-2}	1.14×10^{-3}
B $\left({}^{(N-m)s}/_{rad}\right)$	0.167	5.794	1.174
K $\left({}^{(N-m)}/_{rad}\right)$	357	8,023	458
B_S $\left({}^{(N-m)s}/_{rad}\right)$	$\approx 7.1 \times 10^5$	$\approx 1.6 \times 10^6$	$\approx 1.3 \times 10^6$

9.8 Comparing Impedance / Admittance Two–Port Networks

As already noted, adding physical damping to the I/A network allowed for stiffer force control. Increasing damping by a factor of 17.7 resulted in allowing an increase of high frequency control stiffness of 17 times and low frequency stiffness of 71 times. Substituting the simple first order haptic device model of a mass with damping into equations (43), 88, and 45 and making the simplifications for using velocity feed forward without velocity feedback so that the admittance network structure can be used for tuning the force controller, one can easily show that at high frequencies the stability condition is approximately inversely scaled by the device damping. Stability condition at low frequencies is fairly proportional to the nonlinear cosine term, which can be simplified through small angle approximation to be proportional to the square of frequency and mass / damping ratio. Because of this stiffer force control the resulting impedance network utilizing the brake actually has better transparency at ultra low frequencies by $\approx$ 12 db, just under four times better than the minimum impedance of the network not using the brake. This corresponds to a minimum

impedance at low frequencies corresponding to an inertia of 10.6 Kg–m^2 for the network with the brake versus an equivalent inertia of 42 Kg–m^2 for the network without the brake. As frequency increases minimum impedance of the network using the brake does become less transparent at $\approx$ 0.2 Hz than the network without the brake by just a little over 3.5 times at the highest difference, still much less of an increase than the 17.7 times damping increase which would traditionally cause a direct proportional decrease in minimum transparency if force feedback was not utilized.

When inspecting figure 77 it is most obvious that the network utilizing the brake has a much higher maximum impedance; specifically maximum impedance is increased by $\approx$ 27 db (around 22.4 times). Another benefit of this stiffer impedance virtual coupling is the increased bandwidth of the impedance limits. Without use of the brake the impedance limits cross over at 1.36 Hz, while using the brake and stiffer tuned virtual coupling causes the impedance limits to cross over at 6.4 Hz. Completing the virtual coupling tuning shows that even with higher force control, increased damping allows for less compliant virtual coupling. The higher damped model does give up some transparency in comparison to the lower damped model at part of the frequency range, primarily from approximately 0.3 to 20 rad / sec.

Using EMF damping had less affect on the impedance limits than anticipated. Inspection of figure 78 illustrates maximum impedance is only slightly increased, specifically by $\approx$ 2.1 db, or 1.28 times stiffer. EMF damping had more of an affect on tuning the force controller, decreasing minimum impedance by $\approx$ 9.6 db or 3.0 times less minimum impedance at low frequencies. Though not explored, it would be interesting to see how a network utilizing both the brake and EMF damping compares to these networks.

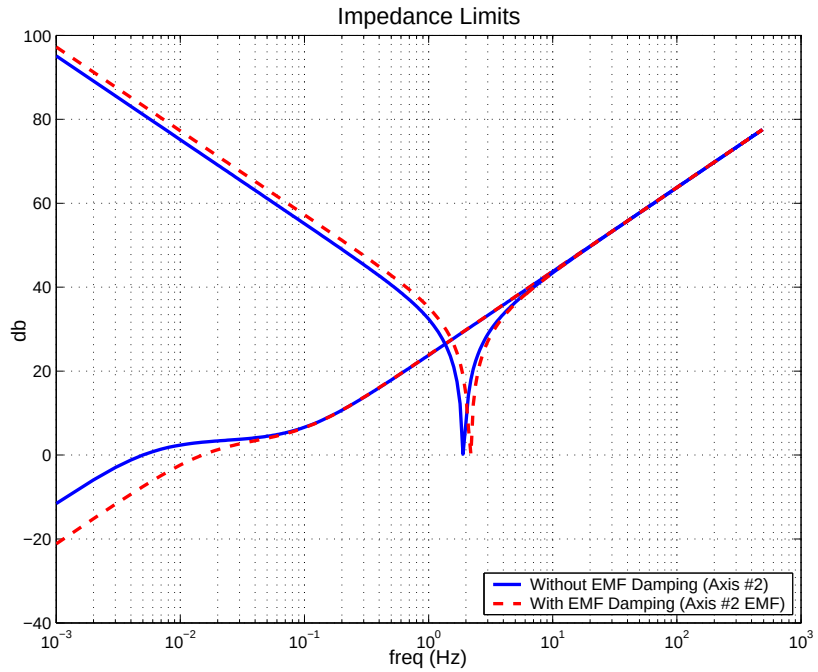

Figure 78: Axis #2 & #2 EMF I/A Impedance Limits Comparison

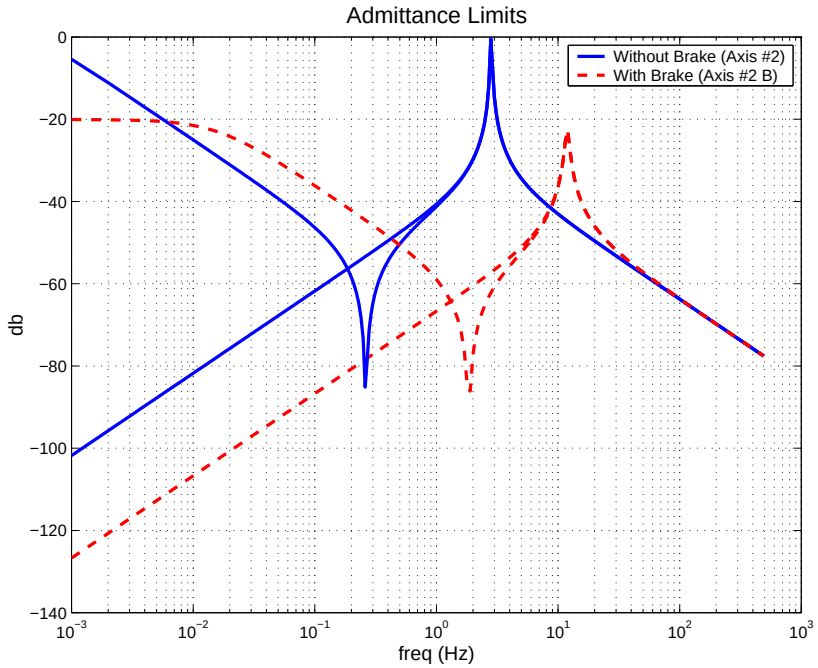

Figure 79: Axis #2 & #2 B Admittance limits comparison

Table 17: A/I Network Parameters for Axis #2, #2 B, & #2 EMF

Axis	**#2**	**#2 B**	**#2 EMF**
Position Controller			
K_p $\left({}^{(N-m)}/_{rad}\right)$	771	13,613	1,667
K_d $\left({}^{(N-m)s}/_{rad}\right)$	0.954	16.85	13.08
Virtual Coupling			
Equation	(124)	(125)	(126)
K	2.788×10^{-5}	2.540×10^{-5}	4.815×10^{-5}
α	0.873	0.607	0.724
β	0.999998	0.9999	0.999999
Physical Parameters			
M $\left({}^{(N-m)s^2}/_{rad}\right)$	282	100	75
B $\left({}^{(N-m)s}/_{rad}\right)$	41,113	64,865	28,698
B_G $\left({}^{(N-m)s}/_{rad}\right)$	0.565	10	0.075

9.9 Comparing Admittance / Impedance Two–Port Networks

As previously noted tuning the velocity controller shows increasing physical damping by a factor of 17.7 allows an increase in controller stiffness by $\approx$ 24.9 db (17.7 times). Because both position stiffness and damping were both increased by the same factor, damping ratio of the resulting closed loop control increased because of both the increased physical damping and increased ratio for damping versus square root of stiffness.

Figure 79 illustrates that increasing damping hurt the network's transparency at frequencies below $\approx$ 0.006 Hz, again a very low frequency, by leveling off; specifically maximum admittance of the A/I network utilizing the brake mimics a device with a damping of $\approx$ 10 (N-m)/(rad/sec) and inertia of $\approx$ 100 Kg–m^2. This decrease in low frequency transparency was a result of the stability criterion leveling off at low frequencies. Physically this may correlate to the controller's limited ability at simulating infinite admittance given the device's physical damping. Though low enough frequencies were not explored, it is hypothesized that the maximum admittance for the network without the brake will level off as well, but to a much smaller value than for the network utilizing the brake. For frequencies above

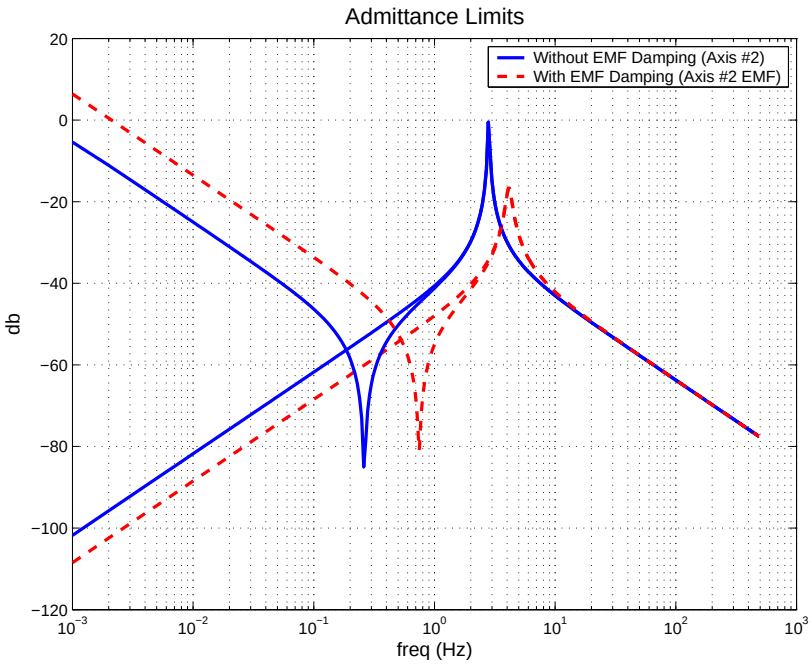

Figure 80: Axis #2 & #2 EMF A/I Admittance Limits Comparison

≈ 0.006 Hz where the inertia effect of the maximum admittance was dominant, the network utilizing the brake provides both better transparency and better stiffness. Maximum admittance of the A/I network not utilizing the brake mimics an inertia of ≈ 300 Kg–m^2. Again this may go against traditional thought that increased physical damping can hurt device performance. Furthermore, because of the stiffer feedback controller and smaller coupling impedance, the network's bandwidth was increased from 0.186 Hz to 1.31 Hz. Furthermore, because increasing the damping allowed the velocity feedback controller to be stiffened it allows for more accurate closed loop reflection.

Where as EMF damping appeared to have minimal affect on the impedance limits of the I/A network, inspection of figure 80 shows it has more of an affect on the admittance limits of the A/I network. As already commented on, using EMF damping allowed stiffer feedback control. At low frequencies the stiffer feedback controller lowered minimal admittance by ≈ 6.7 db (≈ 2.16 times stiffer). One advantage of EMF damping is that the lag–lead controller and increased high frequency damping allowed for 13.7 time the control

damping, providing a much higher closed loop damping ratio. Again, this is not to surprising given that backwards difference velocity estimation can provide noisy command signals which limit allowable gain. By adding high frequency gain and attenuating high frequency motor current greater range of allowable damping control can be used. Furthermore, using EMF damping allowed for the virtual coupling effect to be decreased which results in better network transparency; specifically maximum admittance is increased by ≈ 11.8 db, or 3.9 times maximum admittance. This corresponds to a maximum admittance equivalent to $\approx 75\ Kg\text{–}m^2$ with EMF damping versus $\approx 300\ Kg\text{–}m^2$ for the network without EMF damping. In addition, through increased feedback control and lower virtual coupling affect the network's bandwidth is increased from 0.186 Hz to 0.5298 Hz. Again, though not explored, it would be interesting to see how a network utilizing both the brake and EMF damping compares to these A/I networks.

9.10 Overall Comparison of Increased Damping

It is evident physical damping in the haptic device benefits the system's performance when simulating rigid environments. Increased damping also allows increased feedback control stiffness, which helps increase accuracy of the reflected force or velocity; albeit trade offs are the potential of decreased transparency. EMF damping had a positive effect on both the I/A and A/I networks, though its effect on the I/A network was not as prominent as on the A/I network. Returning to the hybrid active / passive paradigm allows the damper to be set based on the task at hand. By using prior knowledge of the virtual environment or measured environment stiffness to adjust the damping with matching stable feedback control and virtual coupling, the impedance / admittance limits of the haptic two–port network can be adjusted accordingly. For example, physical damping can be increased and the corresponding virtual coupling stiffened when solid, stiff environments are to be realized while virtual coupling and physical damping can be relaxed to increase transparency for free motion.

Identification of the environment would require implementation of a discrete adaptation algorithm. Some work has been performed in identifying interaction environments or using knowledge of the environment's stiffness, but the information "learned" was used in a different manner than proposed.[116, 86] Love chose to identify and store a mapping of the environment, using the information to adjust the digital control parameters. Love used root locus based design and did not touch upon passivity of the system. Salcudean uses the known or measured environment impedance, or admittance, to adjust the two–port haptic-slave network between impedance or admittance implementation. Here it is proposed to adjust the physical damping and virtual coupling to fit the measured environmental impedance while preserving passivity control

CHAPTER 10

EXPERIMENTAL VALIDATION

Previous chapters utilize linearized models of HuRBiRT and Llewelyn's stability criterion to choose haptic two–port network parameters. This chapter will outline and report the results of experimentally selecting said two–port network parameters. Following sections will first present how the discrete virtual environment with virtual coupling is implemented, how energy is discretely estimated, and nonlinear components in the control. Further sections will then present experimental network parameters, qualitative observations, experimental results, and discussion relating said experimental results to theoretical tuning results in this and previous chapters.

10.1 Implementation of Virtual Coupling with Discrete Virtual Environment

Implementation of the virtual coupling with a passive environment requires the environment to be free of delay. This requirement adds practical inconvenience to implementing virtual coupling with discrete virtual environments. Ideally one would prefer to separate the modeled discrete virtual environment and virtual coupling as illustrated in figure 82. Unfortunately doing so creates algebraic loops in the numerical computation. While the significance of this delay in implementing virtual coupling with teleoperation applications is not known and poses an interesting topic, it will not be addressed here.

One work–around for the algebraic loop is to combine the simulated discrete environment and the virtual coupling into one discrete closed loop transfer function as illustrated by figure 83. Based on this combined closed loop virtual environment–virtual coupling the artificial workspace illustrated by figure 84 can be programmed for HuRBiRT, where

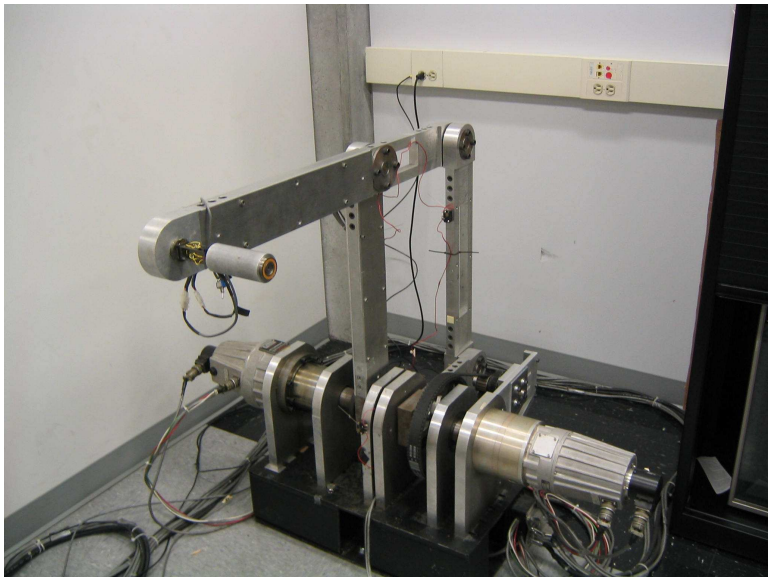

Figure 81: HuRBiRT

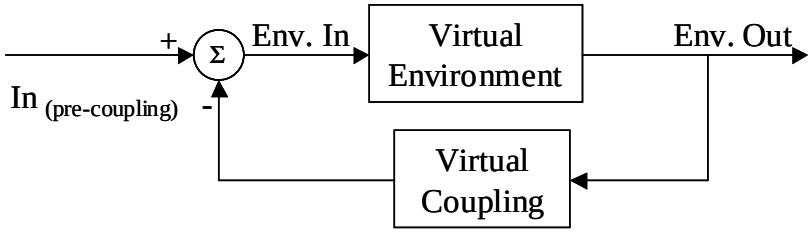

Figure 82: Discrete Environment with Virtual Coupling

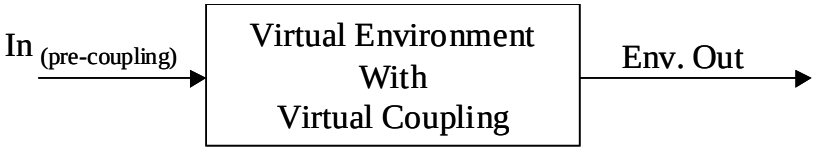

Figure 83: Equivalent Closed Loop Model for Discrete Environment with Virtual Coupling

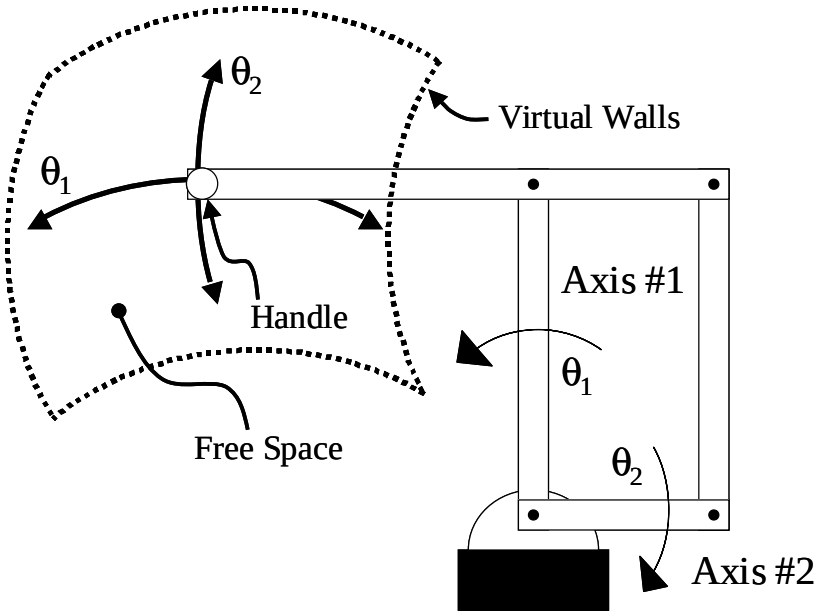

Figure 84: HuRBiRT's Programmed Virtual Wall

environment resistance in the "free space" can be set independent of the virtual walls. This allows testing of the network's transparency and stiffness abilities with one environment structure. Though analysis of two–port networks traditionally use velocity signals, experimental implementation of the environment and coupling was modified via backwards difference differentiation to use position.

Previous chapters outline virtual coupling forms resulting from numerically tuning two–port networks which utilized linear models of HuRBiRT's axes. The I/A virtual coupling form presented in Chapter 7 has a damper in series, B_S in figure 54, in order to satisfy the stability criterion at low frequencies. This damper allows for creep in the interface / environment connection and hinders performance in the experimental system. Initial experiments confirmed the network was stable with B_S removed for various environment stiffnesses tested; therefore I/A coupling used in following sections will not have the additional damper B_S. It is hypothesized that programed integration limits in the force feedback controller helps eliminate any low frequency force "wind up"or coulomb friction provided additional low frequency dissipation, helping eliminate the need for any creep deflection in

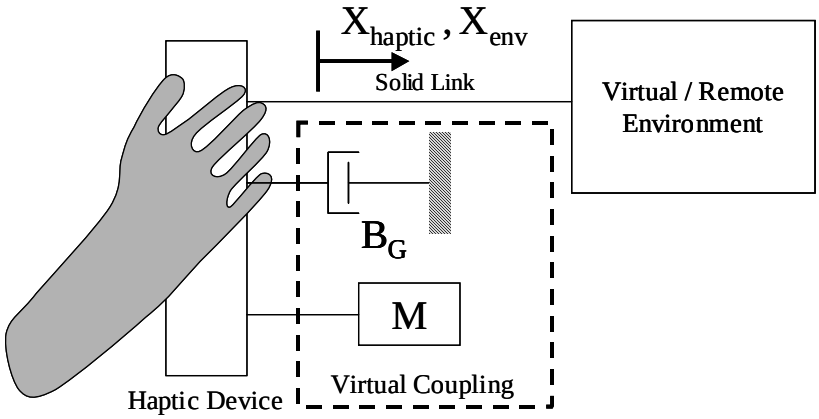

Figure 85: Simplified A/I Virtual Coupling

the I/A virtual coupling. Furthermore, while numerical analysis showed advantage in increasing the I/A coupling form to include pseudo mass, the experimental I/A coupling was reduced to the traditional spring–damper model for ease and intuitiveness of adjustment.

It was also determined the experimental tuning of the A/I coupling illustrated by figure 54 is not intuitive. Rather, the virtual coupling illustrated in figure 85 can be described by

$$F_h - F_e^* = Z_{CA} V_e^* = \left(\frac{(M_c + B_G)z - M_c}{z} \right) V_e^* = \left(\frac{z - \beta}{Kz} \right) V_e^* \tag{127}$$

Removing the damper that is in series with the coupling's mass, eliminating the coupling's high frequency break point, changes the coupling's dynamics from lag–lead to just a lead. Virtual coupling (127) was programmed using the physical variables M_c and B_G to both minimize numerical roundoff that occurs when storing the transfer functions coefficients and to provide "intuitive" variables to adjust. Numerical tuning with HuRBiRT's model proves this coupling form theoretically affords a less transparent coupling. Regardless, it is used as a starting point for experimental tuning which is to be compared with previously presented "optimal" numerical tuning of networks based on HuRBiRT's model.

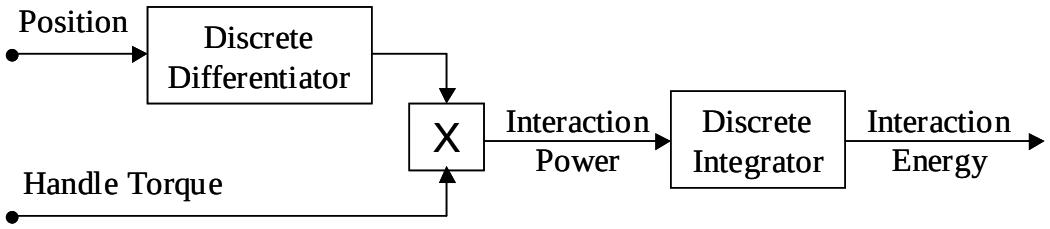

Figure 86: Discrete On line Human–Device Energy Estimation

10.2 On–Line Energy Measurement, and Control Nonlinearities

To monitor human–device interaction energy from measured device position and handle torque, the position must first be discretely differentiated and then multiplied by human–device interaction torque to estimate instantaneous interaction power which is discretely integrated to estimate interaction energy. It was found through testing this simple technique with numerical simulations of continuous systems that bilinear transformation (Tustin) based differentiation and integration, with better phase preservation than backwards difference, proved more accurate at estimating interaction energy than backwards difference.

Besides device nonlinearities in the hardware, some additional nonlinearities were added to the control. First, axis #1's motor is capable of applying $\approx 2,200$ N–m, or $\approx 3,620N$ at the handle. Even though it is known to compromise performance, for safety reasons torque is software saturated at 500 N–m, or $\approx 820N$ of handle force. Furthermore, as outlined in previous chapters, the force feedback controller utilizes integral action. Saturation limits were added to this integral action so as to minimize affects of integrator wind up and subsequent stability issues. Future sections will outline how this saturation limit was chosen and its effects on device performance and stability.

The procedure for experimentally tuning consisted of first creating an I/A network without virtual coupling, but just the discrete virtual environment illustrated in figure 84. First, human induced motion in the environment's "free space" is used to adjust the force feedback controller so as to maximize transparency while retaining a passive human–machine

interface. Next, wall damping and stiffness were adjusted so as to satisfy stability and passivity. Resulting wall stiffness and damping were used as the virtual coupling parameters, while wall parameters from the trials that did not use force control were utilized as a basis for selecting the position PD controller in the A/I network. To complete the A/I network a PD controller was selected and the virtual coupling illustrated by figure 85 was adjusted so as to maximize transparency and preserve passivity of the human–machine interface.

Experimental parameters presented in the following sections are much more aggressive than those derived in past chapters through numerical analysis of the models. Why is this? Several factors may contribute to these differences. First, numerical models assumed negligible motor amplifier dynamics and a pure time delay of one sample period. In reality the delay may be less, motor amplifier dynamics have limited bandwidth, and the human's actuation has limited bandwidth. Furthermore, linear passivity condition is based on phase of the system over all frequencies and is not dependent on magnitude amplification of the response. While a system may not be passive over a given frequency range, it's non–passive response over that frequency range may be minuscule due to the system's attenuation or because excitations in that range are minimal compared to other more dominant components in the excitation. Active response at said frequency may be countered by greater dissipation at the more dominant frequencies, resulting in net dissipation when measuring energy flow over time. One topic that is briefly explored is tuning the models to a lower frequency than the Nyquist frequency used in past chapters. Following sections will also present "theoretical" two–port parameters resulting from "optimal" numerical tuning networks modified to eliminate the pure time delay and only include frequencies up to 20 Hz, rather than the digital controller's Nyquist frequency.

10.3 Experimental Tuning of I/A Two-Port Parameters

Various unmodeled device nonlinearities and dynamics created limitations in selecting two–port control parameters. First, Axis #1's harmonic drive has slight pulsation and binding

Table 18: Axis #1 I/A Network Experimental Parameters

Axis	**#1**	
Force Controller		
K_p $\left({}^{(N-m)}/_{(N-m)}\right)$	2.0	0.0
K_i $\left({}^{(N-m)}/_{(N-m)s}\right)$	18	0
$\text{sat}(\int (K_i \times Error)dt)$ $_{(N-m)}$	$\pm$100	NA
Virtual Coupling		
Transfer Function	(74)	(74)
B $\left({}^{(N-m)s}/_{rad}\right)$	1,100	1,100
K $\left({}^{(N-m)}/_{rad}\right)$	100,000	100,000
Coefficients		
K_{cc}	1,200	1,200
α_c	0.917	0.917

from the harmonic action. This disturbance is magnified with high proportional force feedback gains, therefore proportional force feedback gains were limited to the values listed in table 18. While higher gains did not destabilize the system, they did result in deterioration of device smoothness. Similarly, backlash in Axis #2's gear box causes adverse effects with proportional force feedback, therefore it was limited to values listed in table 19. Integral gains and saturation were adjusted to complete the force feedback controller such that passivity is preserved while maximizing transparency when moving HuRBiRT in the environment's "free space". Integral limits were selected so that the occurrence of integrator saturation was minimized when moving quickly in the "free space".

Selecting wall parameters, stiffness and damping, was accomplished through first adjusting damping and then stiffness. It was found that high frequency noise, drive line compliance, gear backlash, etc caused chatter in a system with too high of environment wall damping. Wall stiffness was adjusted to the point of either wall chattering or such that initial contact of the virtual wall with the operator letting go causes the device to perpetually bounce between artificial limits. Again, resulting parameters are listed in tables 18 and 19. It was found that lower integrator saturation limits, while limiting effectiveness

Table 19: Axis #2 & # 2B I/A Network Experimental Parameters

Axis	**#2**			**#2 B**		
Force Controller						
K_p $\left({}^{(N-m)}/_{(N-m)}\right)$	0.05	0.05	0.00	0.05	0.05	0.00
K_i $\left({}^{(N-m)}/_{(N-m)s}\right)$	2.0	2.0	0.0	12.5	12.5	0.0
$\text{sat}(\int (K_i \times Error)dt)$ $(N-m)$	$\pm$10.0	$\pm$5.0	NA	$\pm$25.0	$\pm$15.0	NA
Virtual Coupling						
Transfer Function	(74)	(74)	(74)	(74)	(74)	(74)
B $\left({}^{(N-m)s}/_{rad}\right)$	25	25	25	25	25	25
K $\left({}^{(N-m)}/_{rad}\right)$	2,000	5,500	8,000	5,500	8,000	8,000
Coefficients						
K_{cc}	27	30.5	33	30.5	33	33
α_c	0.926	0.820	0.758	0.820	0.758	0.758

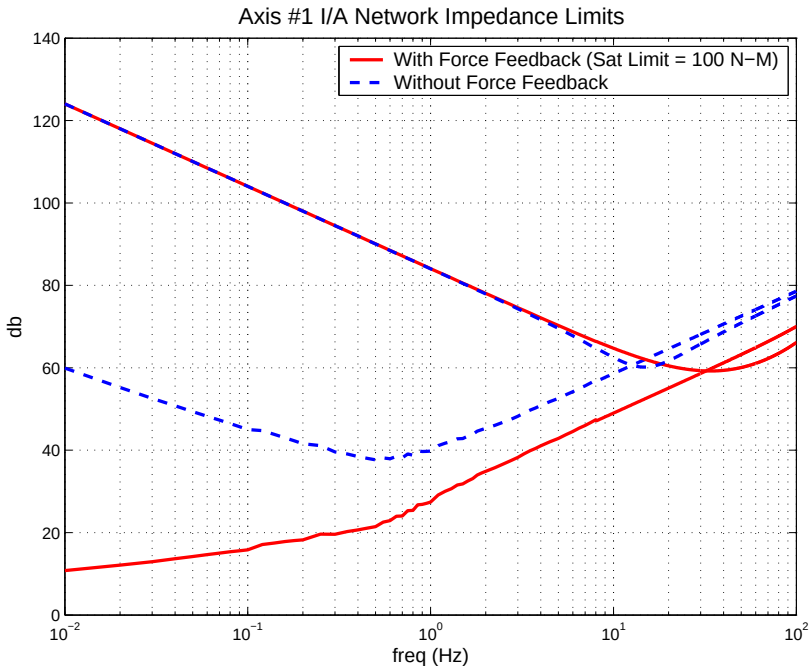

Figure 87: Axis #1 I/A Experimental Impedance Limits

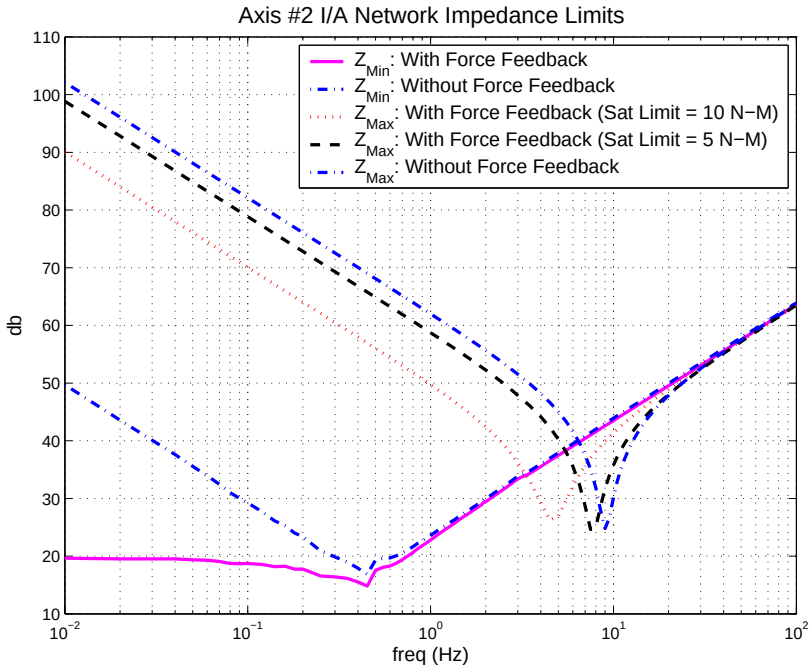

Figure 88: Axis #2 I/A Experimental Impedance Limits

of integral action, allowed for stiffer walls. It was noticed that the integrator would saturate at wall interaction, causing the device to be propelled away from the wall whenever the user immediately let go after contacting the virtual wall. Once the device reached the opposite wall, with the operator no longer holding the handle and therefore not imparting any interaction force/torque, the integrator would saturate in the opposite direction and the limit cycle would repeat. Lowering saturation limits or lowering wall stiffness allowed the device's physical dissipation to reduce, or dampen out, this cycle.

Figures 87 through 90 illustrate the resulting impedance limits for an I/A network formulated from the experimental frequency response data presented in Chapter 6 for HuRBiRT and the experimentally tuned network control parameters listed in table 20. Figure 87 illustrates the improvement in transparency when stable force feedback control is used with Axis #1. Figure 88 and 89 illustrate the effect of force feedback and varying force controller integration saturation limits on impedance limits of Axis #2 and Axis #2 B respectively; specifically that lowering saturation limits allows for stiffer coupling and as with Axis #1, adding force feedback improves transparency. Figure 90 compares impedance limits of Axis

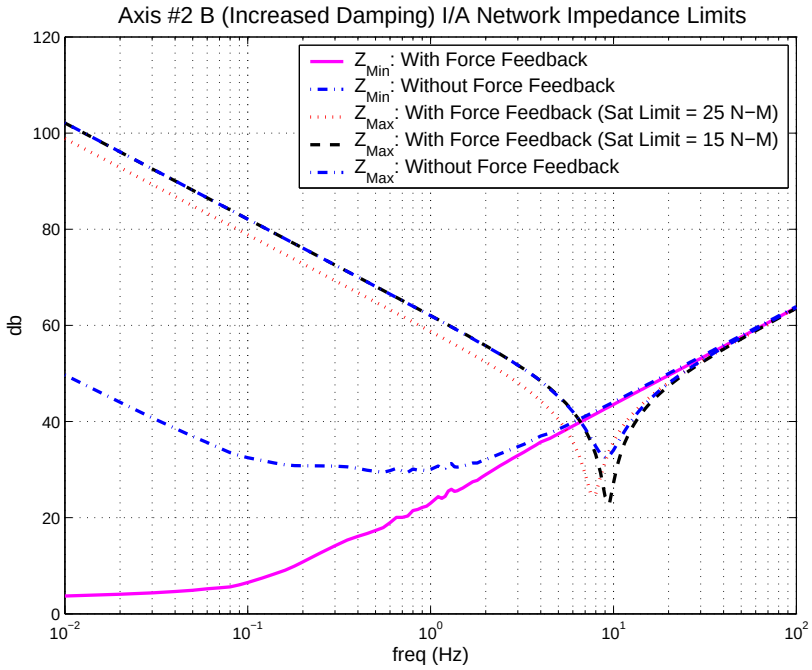

Figure 89: Axis #2 I/A Experimental Impedance Limits

#2 and Axis #2 B for force controllers with the higher saturation limits. Axis #2 B, with increased physical damping, shows to be a more transparent and stiffer network than Axis #2 when experimental two–port parameters are used with the experimental system identification data presented in Chapter 6. As predicted, Axis #2 B also provides a network with higher maximum / minimum impedance crossover frequency, which means the network for Axis #2 B has a higher usuable bandwidth.

How do these experimental I/A network parameters compare with the parameters numerically tuned from linearized models of HuRBiRT's axis? Figure 91 illustrates that experimental network parameters for Axis #1 are much more transparent and stiffer than when using numerically tuned parameters. Specifically, when the experimental force controller is used with the linearized model the resulting network's minimum impedance is estimated to mimic an inertia of 2.8 Kg–m^2, as opposed to 22 Kg–m^2 and 100 Kg–m^2 for numerical tuning with and without consideration of human dynamics respectively. Similarly, experimental virtual coupling is much stiffer with a stiffness of 100,000 (N-m)/rad and damping of 1,100 (N-m)/(rad/s), as opposed to 13,547 (N-m)/rad & 7.85 (N-m)/(rad/s) and 32,143

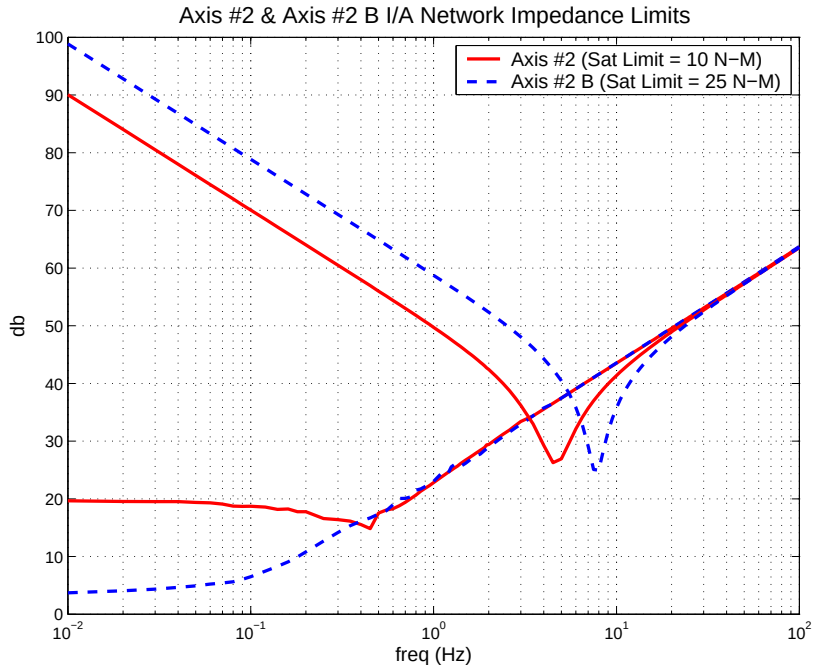

Figure 90: Axis #2 & #2 B I/A Experimental Impedance Limits

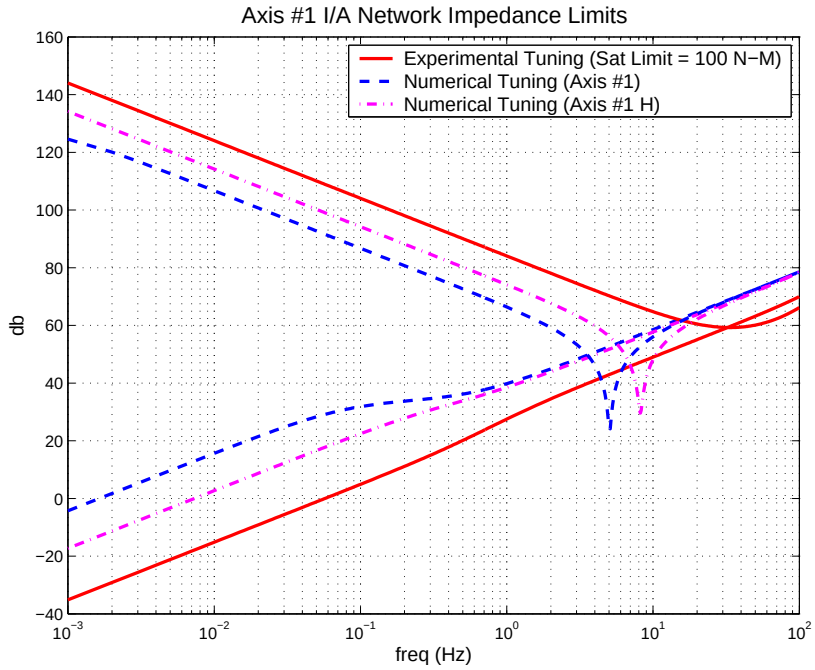

Figure 91: Axis #1 I/A Numerical and Experimental Impedance Limits Comparison (uses linear model for $Z_d(j\omega)$)

(N-m)/rad & 97 (N-m)/(rad/s) for numerical tuning with and without consideration of human dynamics respectively, resulting in both a stiffer network and a network with a higher maximum / minimum impedance crossover frequency. While damping in the experimental coupling pushed stability limits, because of safety considerations stiffness for Axis #1 was not pushed to absolute limits. Figure 92 shows a similar trend for Axis #2, with minimum transparency of 0.75 Kg–m^2 resulting from using the experimental force controller with the linearized model, apposed to 42 Kg–m^2 for numerical tuning. Figure 93 illustrates similar minimum impedance trends for Axis #2 B, with a minimum impedance mimicking 2.2 Kg–m^2 as apposed to 10.6 Kg–m^2. While Axis #1 and Axis #2 experimental couplings were stiffer than numerically tunned coupling, experimental coupling for Axis #2 B has a lower spring stiffness, 5,500 (N-m)/rad compared to 8,023 (N-m)/rad, but higher damping of 25 (N-m)/(rad/s) compared to 5.8 (N-m)/(rad/s), than that resulting from "optimal" numerical tuning. It should be noted that numerical tuning was based on a force controller considerably less stiff than experimentally used. When the force controller was relaxed in the experimental testing it allows for stiffer virtual coupling at the expense of transparency. Similarly, when the force controller integration saturation limits were lowered it allowed the experimental coupling's spring stiffness to be increased to that comparable with the numerical tuning results.

While figure 90 and 77 show the respective experimental and numerical based network limits for Axis #2 B being more transparent than Axis #2 over certain frequencies, figure 94 shows using experimental force controller with the linearized model results in the network for Axis #2 being more transparent than Axis #2 B for all frequencies. It is hypothesized the reason this differs from results illustrated by figure 90 is that Coulomb friction in Axis #2 has higher low frequency dissipation than the equivalent modeled viscous damping, while viscous damping from the brake contributes more to Axis #2 B's modeled damping than Coulomb friction in the system.

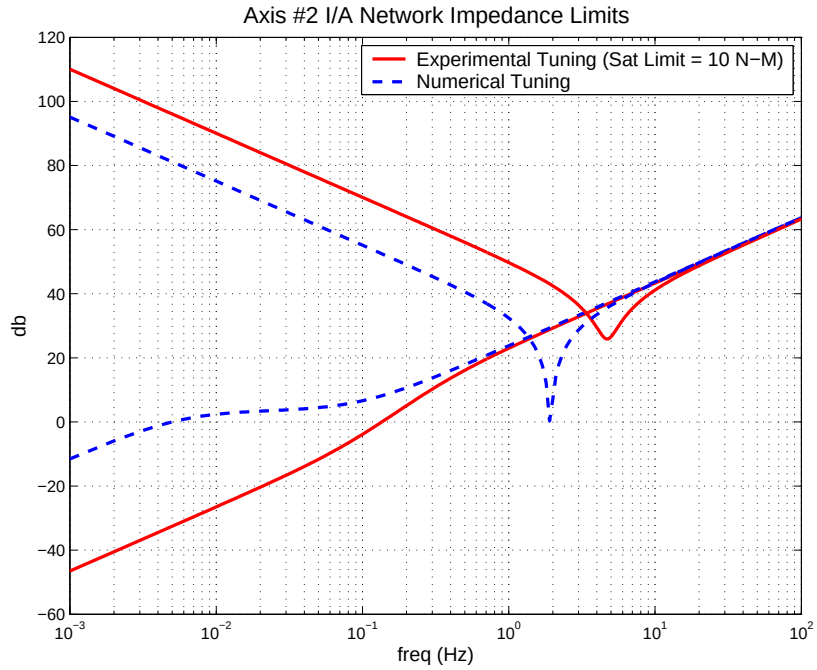

Figure 92: Axis #2 I/A Numerical and Experimental Impedance Limits Comparison (uses linear model for $Z_d(j\omega)$)

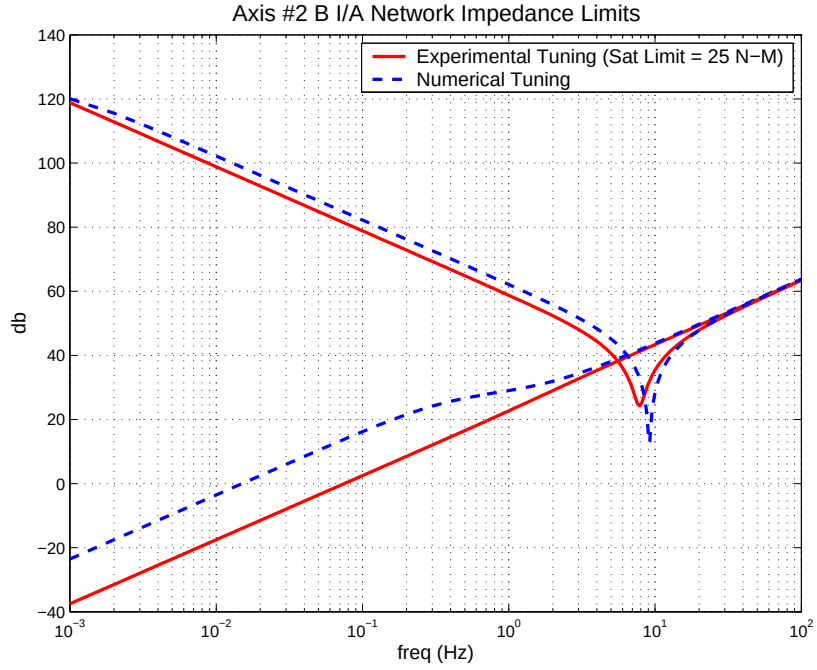

Figure 93: Axis #2 B I/A Numerical and Experimental Impedance Limits Comparison (uses linear model for $Z_d(j\omega)$)

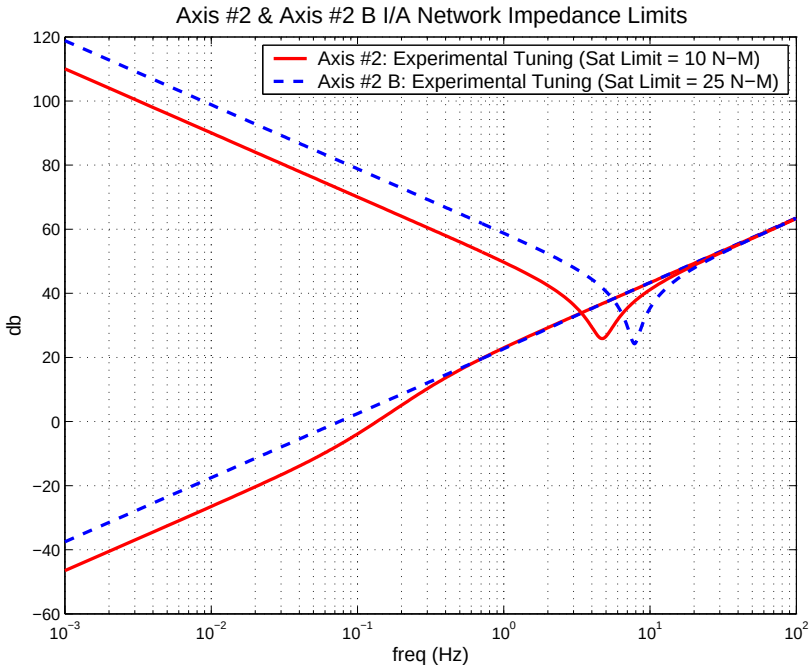

Figure 94: Axis #2 & #2 B Experimental Impedance Limits Comparison (uses linear model for $Z_d(j\omega)$)

10.4 Experimental Tuning of A/I Two-Port Parameters

Position controller for the A/I networks were selected by slightly relaxing the virtual coupling from the I/A network which did not utilize force feedback. Next, virtual coupling described by figure 85 and equation 127 was combined with the virtual environment to complete the network. Similar to the procedure used for adjusting the force controller in the I/A network, the A/I network's coupling parameters were adjusted so as provide the best transparency while still preserving passive interaction for movement in the environment's "free space". First, coupling damping was initially set to zero and coupling mass decreased until higher frequency movements ($\approx$ 0.75–1.5 Hz) caused a non passive interface. After increasing mass so as to provide a passive "high frequency" man–machine interaction, coupling damping was increased until "low frequency" movement within the "free space" also resulted in passive human–machine interaction. Resulting parameters can be viewed in table 20. Figures 95 and 96 compare A/I admittance limits for HuRBiRT when the networks were both numerically and experimentally tuned. While these coupling parameters represent what was experimentally determined to provide a passive interface when moving

Table 20: Axis #1, #2, & #2 B A/I Network Experimental Parameters

Axis	**#1**	**#2**	**#2 B**
Position Controller			
K_p $\left({}^{(N-m)}/_{rad}\right)$	50,000	5,000	5,000
K_d $\left({}^{(N-m)s}/_{rad}\right)$	1,000	20	20
Virtual Coupling			
Equation	(127)	(127)	(127)
M $\left({}^{(N-m)s^2}/_{rad}\right)$	20	2.5	2.5
B_G $\left({}^{(N-m)s}/_{rad}\right)$	1.5	0.5	4.0
Coefficients			
K	4.9996×10^{-5}	3.9992×10^{-4}	3.9944×10^{-4}
β	0.9999	0.9998	0.9986

in the environment's "free space", it was found that much lower coupling values could safely be used; though the resulting network with improved transparency was more likely to result in slightly active human–machine interaction dynamics that.

Figure 95 illustrates the experimentally and numerically tuned A/I network limits for Axis #1. Experimental tuning resulted in both a more transparent and stiffer environment for Axis #1 when human dynamics were not considered in the numerical tuning. Using a stiffer velocity controller when considering human dynamics results in a stiffer, but less transparent network (Axis #1 H_1) than experimentally derived. Even relaxing the velocity controller by approximately 30% (Axis #1 H_2) when numerically tuning with human dynamics, while resulting in a more transparent network through a more transparent virtual coupling, results in a less transparent network above 0.004 Hz than experimental tuning. While the experimental coupling has a much lower mass, which makes it more transparent at higher frequencies, it has more grounded damping than numerically tuned coupling, which hurts low frequency transparency. While lower grounded damping comporable to that in the numerical tuning could be safely used on HuRBiRT, it was found that slight damping helped with user control and to guarantee the "free space" dynamics contained some dissipation. Furthermore, as already commented the experimental velocity controller

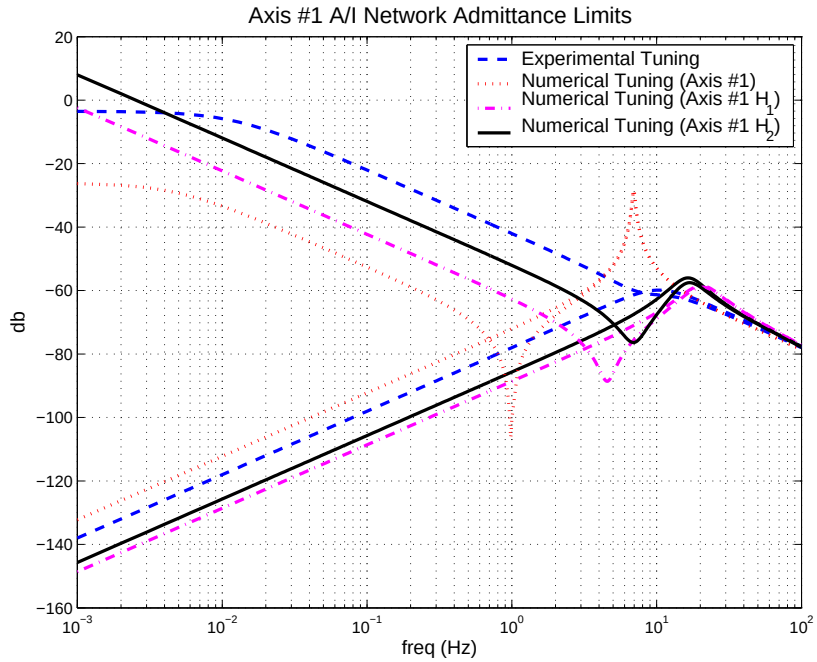

Figure 95: Axis #1 A/I Numerical and Experimental Admittance Limits Comparison

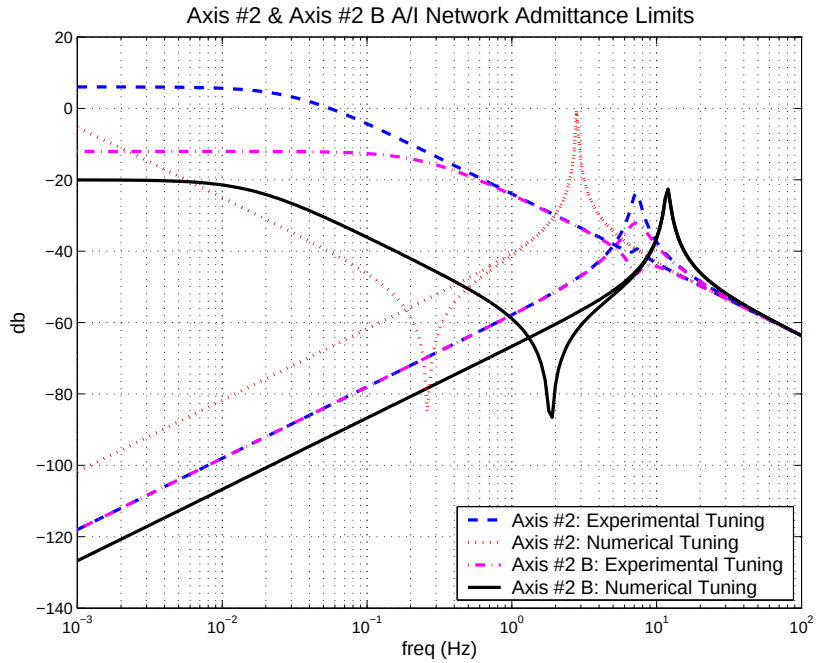

Figure 96: Axis #2 & Axis #2 B A/I Numerical and Experimental Admittance Limits Comparison

was not set at the absolute limits and could have been stiffer, but given the already stiff control, software set saturation limits, and limited position damping, a stiffer position controller (spring stiffness) only provided marginal increase in perceived device stiffness.

Figure 96 illustrates the admittance limits for experimentally and numerically tuning Axis #2 and Axis #2 B. Again, experimental tuning resulted in a stiffer network than numerically tuning for Axis #2, but not for Axis #2 B. Worth noting is that experimental velocity controller for Axis #2 and Axis #2 B were the same. If the magneto–rheological brake did not have backlash or if it was connected to the motor shaft and not the 20:1 gearbox output shaft, it might be more effective at damping out the controller chatter and allow stiffer velocity control of Axis #2 B. As with Axis #1, experimentally tunned coupling was more transparent than numerically tuned coupling, with experimental coupling for Axis #2 being more transparent than Axis #2 B for frequencies below $\approx$ 1 Hz. Again, while the A/I coupling parameters presented represent passive experimental operation, A/I coupling inertia and damping could be reduced by an order of magnitude while still providing a stable interface.

It is interesting to note that past chapters illustrated how numerically tunned A/I networks had a much lower maximum / minimum admittance crossover frequency than the I/A network's maximum / minimum impedance crossover frequency for the same system, but experimental parameters result in the comparable crossover frequencies for the respective networks. Furthermore, combining experimental I/A and A/I network parameters (tables 18, 19, and 20) with linearized HuRBiRT models results in I/A networks being more transparent than the respective A/I networks, but when combined with experimental input/output frequency data from Chapter 6 the opposite is true. This can be attributed to HuRBiRT having considerable Coulomb friction rather than viscous damping. Such friction is indirectly compensated for in the A/I network through the velocity controller's position feedback. Alternatively the I/A network's force controller's limited error rejection and the friction force, which causes higher low frequency resistance than does viscous damping, limit

low frequency transparency of the I/A network.

Theoretically coupling form (108) allows for more transparent coupling than (127), but for reasons already given coupling (127) has been utilized for experimental tuning. Using coupling in table 20 as a starting point, expanded coupling (108) was experimentally investigated. Unfortunately it was found that adding the damper in series with the mass caused deterioration of performance on HuRBiRT. Specifically if coupling inertia was kept comparable to that listed in table 20 and the damper connected to it was decreased, the device would jump when the operator moved it away from contacting the virtual wall. Raising inertia helped reduce this problem at the expense of transparency. Using coupling derived through numerical tuning could be successfully implemented, but as illustrated by figures 95 and 96 these couplings are not as transparent as the coupling's experimentally derived through use of (127).

10.5 Investigation of Stability Over Finite Frequency Range

Earlier the notion of only tuning over a finite frequency range instead of up to the Nyquist frequency was alluded to. While a system may not be passive above a set frequency, it's response above that frequency may be minuscule due to the system's attenuation or because high frequency excitations are minimal compared to other more dominant components in the excitation. What would result if the linear models were only numerically tuned over a limited frequency range and high frequency characteristics were ignored? Adjusting the two–port models to eliminate the one sample pure time delay and only investigate frequencies up to 20 Hz, twice the maximum frequency used during experimental system identification, results in the two–port parameters listed in table 21, 22, and 23.

Table 23 lists resulting I/A parameters when only investigating the network's stability over the finite frequency range. Comparing these numerically tunned parameters to those in past chapters shows that by cutting back the frequency range investigated allows for

Table 21: I/A Network Parameters Numerically Tuned up to 20Hz

Axis	**#1**	**#1 H**	**#2**	**#2 B**
Force Controller				
K_p $\left({}^{(N-m)}/_{(N-m)}\right)$	0.0472	0.238	0.00818	0.1249
K_i $\left({}^{(N-m)}/_{(N-m)s}\right)$	1.61	3.61	0.111	7.65
Virtual Coupling				
Transfer Function	(74)	(74)	(74)	(74)
B $\left({}^{(N-m)s}/_{rad}\right)$	995	2,552	34.5	172.8
K $\left({}^{(N-m)}/_{rad}\right)$	79,998	153,141	4,415	21,698
Coefficients				
K_{cc}	1,075	2,705	38.915	194.498
α_c	0.926	0.943	0.887	0.888

stiffer force control and virtual coupling, especially coupling damping. Specifically force controller proportional gains could be increased by a factor of ten and integral gains by a factor of three, except for when the human model was incorporated into Axis #1's tuning (proportional increased two times and integral increased 1.5 times). Increase in virtual coupling damping and stiffness did not increase a consistent amount, with damping increasing from 26 to 206 times and stiffness increasing from 2.7 to 12 times that of when tuning for all frequencies up to the controller's Nyquist frequency. Comparing experimental network parameters to these shows that except for Axis #1 (without human limit models) the coupling for the newly tunned parameters are stiffer than experimentally achieved, but force controller parameters are still much less aggressive (less transparent network) than experimentally possible; except proportional force controller gain for Axis #2 B. Again, experimental force controller gain for Axis #2 and Axis #2 B was limited by gear train backlash. Possibly higher proportional gains could be achieved if the brake was mounted directly to the motor shaft instead of the gearbox's output shaft. As already mentioned, due to safety considerations coupling tuning for Axis #1 was not experimentally pushed. It is possible the spring stiffness of the experimental Axis #1 coupling could be increased, but damping was near its limit. It should also be noted that numerical tuning of coupling was based on the considerably less stiff force controller than used in experimental tuning.

Table 22: A/I Network Parameters Numerically Tuned up to 20Hz

Axis	**#1**	**#1 H_A***	**#1 H_B***	**#2**	**#2 B**
Position Controller					
K_p $(^{(N-m)}/_{rad})$	50,000	50,000	50,000	5,000	5,000
K_d $(^{(N-m)s}/_{rad})$	1,000	1,000	1,000	20	20
Virtual Coupling					
Equation	(108)	(108)	(108)	(108)	(108)
K	8.117×10^{-4}	1.95×10^{-3}	9.33×10^{-4}	9.539×10^{-4}	2.634×10^{-3}
α	0.8866	0.8874	0.8873	0.9248	0.9275
β	0.99997	0.999992	0.999999	0.9999999	0.99926
Physical Parameters					
M $(^{(N-m)s^2}/_{rad})$	10.9	4.6	9.5	13.9	5.19
B $(^{(N-m)s}/_{rad})$	1,377	578	1,208	1,134	405
B_G $(^{(N-m)s}/_{rad})$	0.302	0.0351	4.07×10^{-3}	1.14×10^{-3}	3.85

*H_A: Pursuit human model M,B,K; *H_B: Pursuit human model F_h

If the force controller was relaxed in the experimental testing the resulting experimental coupling can be stiffened, though again experimental damping was limited by unmodeled system properties.

Table 22 lists resulting A/I parameters when only investigating the network's stability over the finite frequency range. To better correlate with experimental networks, the experimental velocity controller was used; which was not possible when previously numerically investigating Llewelyn stability up to the Nyquist frequency. Comparing resulting coupling parameters with past numerically tunned coupling shows them to be much more transparent and closer to what was experimentally archived, signifying that limiting frequency range results in more transparent networks. Though numerical tuning listed in table 22 uses the higher order coupling form that was not experimentally used, table 23 lists the resulting network parameters when the simpler coupling (127) is numerically tuned instead of (108). Results in table 23 are much less transparent than those in table 22 or that which was experimentally achieved (table 20). Even with this less transparent coupling form, the resulting networks are more transparent than networks presented in tables 15 and 17, which

Table 23: A/I Network Parameters Numerically Tuned up to 20Hz (simple coupling)

Axis	**#1**	**#1 H_A***	**#1 H_B***	**#2**	**#2 B**
Position Controller					
K_p $(^{(N-m)}/_{rad})$	50,000	50,000	50,000	5,000	5,000
K_d $(^{(N-m)s}/_{rad})$	1,000	1,000	1,000	20	20
Virtual Coupling					
Equation	(127)	(127)	(127)	(127)	(127)
M $(^{(N-m)s^2}/_{rad})$	90	36	80	194	74
B_G $(^{(N-m)s}/_{rad})$	0.305	0.036	0.104	0.815	3.85
Coefficients					
K	1.111×10^{-5}	2.778×10^{-5}	1.250×10^{-5}	5.155×10^{-6}	1.351×10^{-5}
β	0.9999966	0.999999	0.9999987	0.9999958	0.999948

*H_A: Pursuit human model M,B,K; *H_B: Pursuit human model F_h

considered all frequencies up to the controller's Nyquist frequency.

While this initial exploration of investigating Llewelyn's stability up to a limited frequency was only performed for an arbitrary maximum frequency of 20 Hz, it adds insight into using this two–port analysis method. Lowering the maximum investigated frequency allows for much stiffer velocity controller and I/A coupling parameters. Specifically the damping in the I/A coupling and A/I velocity controller was considerably increased, while spring stiffness slightly increased. As noted, resulting numerically tunned networks are now stiffer than the experimental networks, therefore choosing a maximum frequency of 20 Hz appears to be too low when considering velocity controller and I/A coupling. Alternatively, resulting numerically tunned networks were still less transparent than the experimental networks. Transparency of the experimental networks were tunned through monitoring interaction energy of the operator with the device. Operator's input had limited bandwidth, effectively limiting the investigated experimental frequency range to much less than 20 Hz. Therefore choosing a maximum frequency of 20 Hz appears to be high when considering feedback force control or A/I coupling.

CHAPTER 11

RESEARCH OVERVIEW & FUTURE DIRECTION

Chapter one lists several contributions of this research. Specifically this research has built on the two-port haptic network paradigm introduced by Adams and Hannaford through the following:

1. Investigation of how nonlinear components affect the application of previously used two–port passivity based stability criteria.

2. Expansion of the concept of virtual coupling to nonintuitive forms.

3. Introduction of force feedback into the traditional impedance two–port network.

4. Showing the true duality between the traditional admittance and traditional impedance two–port networks, giving insight into velocity and force feedback controller selection.

5. Proposed biomechanical based human dynamic models for interaction with mechanical devices are demonstrated using one human subject's frequency response to device perturbations. Resulting model properties are compared with various human models published in haptic literature.

6. Incorporation of human models as impedance or admittance limits and the investigation of how using experimentally determined human models affects selection of the two–port control parameters.

7. Application of the two–port haptic network analysis to a hybrid active / passive in parallel device and analysis of DC motor back EMF damping.

8. Experimental validation of haptic two–port network stability on a nonlinear two DOF haptic device that can be configured to provide admittance or impedance reflection, with one DOF converted so as to provide an axis of hybrid active / passive actuation.

While details of these contributions are presented in previous chapters, following sections will briefly review the main points.

11.1 Investigation of Non-Linear Effects

First, detailed information on Llewelyn's stability criterion and how it differs from passivity requirement of a two–port network was presented. Llewelyn originally applied his analysis to linear two–port circuits interfaced with passive linear terminating one–port networks. Through use of strictly positive real (SPR) conditions Lyapunav's indirect method can be used to guarantee a nonlinear system is exponentially passive near the equilibrium point of question and therefore provides a dissipative interface to the user. This allows use of Llewelyn's stability criterion on nonlinear systems through linearization and application of SPR conditions to Llewelyn's stability criterion. Possible sources of nonlinear components in a haptic two–port network and practical methods for guaranteeing SPR of the linearized models are briefly discussed. Later sections use linearized experimental models as the basis for developing two–port networks for a nonlinear haptic testbed. These networks are later experimentally verified on the haptic testbed.

11.2 Incorporation of Human Modeling

Early chapters investigate the origin of assuming the human as a passive element in the haptic system, while later chapters challenge this assumption through using the experimental frequency response of one human subject to both smooth and random position perturbations. Experimental data shows the subject was able to control the device in a passive manner when responding to smooth perturbations that can be predicted. Alternatively, when reacting to random signals the subject's response contained considerable phase lag, which caused the response to no longer be passive. It was also shown that the subject had higher control stiffness and bandwidth when regulating smooth predictive perturbations than when regulating random perturbations, specifically the human subject's control stiffness and bandwidth for this system increased from 7,350 N/m and $\approx$ 0.9 Hz to 13,044 N/m and $\approx$ 2.5 Hz. This increase in bandwidth and stiffness correlates with trends presented in

various literature. It also suggests that giving the operator a preview of the environment's interaction might aid in improving human's performance and ability to stabilize a system. Both linear second order and nonlinear biomechanical stiffness models for describing the subject's response were presented and compared to other dynamic models in haptic research. Furthermore, the notion of specific haptic model's being specific to the device used and human kinematic configuration was touched upon; that is human stiffness and damping models developed on one device / configuration can not be arbitrarily applied to another device / configuration.

While incorporating human stiffness models within the haptic system modeling is not in itself a new idea, this research presents a specific argument and methodology for including human admittance or impedance limits in the analysis of two–port networks. The aforementioned human models based on physical neural muscular phenomenon were incorporated into the two–port analysis as stiffness limits. While these model parameters derived from only testing one subject can not decisively validate the model forms and human dynamic limits for the specified haptic device interaction, it does successfully demonstrate how they can be applied and their effect on two–port network parameter selection. It was found adding such human limits allows for considerably more aggressive network control and coupling parameters.

11.3 Duality Between A/I and I/A Two–Port Networks

Formulation of the I/A network was expanded to include force feedback control. It was shown that similar to how the inverse of virtual coupling for an I/A network without force feedback can be used as the A/I network's velocity controller, the inverse of virtual coupling for an A/I network without velocity feedback control can be used as the I/A network's force feedback controller. This allows for improved transparency of the I/A network, though it theoretically requires relaxing virtual coupling stiffness for the two–port network to satisfy Llewelyn's stability criterion. Having two sets of parameters, one feedback controller and

one virtual coupling, makes tuning either haptic two–port network formulation a trade off between stiffness and transparency. A tuning methodology utilizing constrained nonlinear optimization routines was presented and demonstrated in order to facilitate parameter selection while investigating effects of different model parameters.

Several cases based on linearized models of HuRBiRT's axes were used to demonstrate formulation of the I/A and A/I networks. These network models were compared to determine differences in anticipated performance of structuring the problem as admittance reflection versus impedance reflection. Through the numerical models it was illustrated the I/A network theoretically provides better transparency, but lower maximum stiffness, than the A/I network. This leads to the idea that A/I networks, which inherently regulate device position, may be better suited for stiff environment reflection, while I/A networks, which inherently regulate interaction force / torque, may be better suited for transparent environment reflection. It was also illustrated that the I/A network had a higher maximum / minimum impedance crossover frequency than the A/I network's minimum / maximum admittance crossover frequency, signifying the I/A network can theoretically provide higher bandwidth. Furthermore, the proposed tuning procedures were utilized for tuning expanded, non intuitive forms of the virtual coupling for the I/A and A/I networks. Resulting transfer functions were then related back to equivalent physical models for a better intuitive understanding of the virtual coupling's physical interaction with the system. Such physical insight proved useful when experimentally implementing the two–port networks and experimentally adjusting network parameters.

11.4 Investigation of Hybrid Active / Passive Device via Two–Port Analysis

The idea of adding passive elements to a haptic device was investigated using the two–port paradigm. Effects of increased physical dissipation on the admittance and impedance limits of haptic two–port networks was demonstrated, primarily increasing viscous damping and

the introduction of EMF damping were theoretically studied while effects of increased viscous damping were also experimentally validated.

Addition of EMF damping was found to allow a slightly stiffer, but more transparent, I/A network. Adding EMF damping to the A/I network resulted in a system that was considerably more transparent and roughly twice as stiff when compared to removing the EMF damping. Furthermore, it was found that increased high frequency physical damping and resulting lag–lead motor current dynamics theoretically allowed for significant increase of control damping in both the A/I network's velocity controller and I/A network's virtual coupling. Selection of the EMF circuit parameters is another design problem worthy of experimental investigation. It is hypothesized that addition of physical high frequency electrical damping and lag–lead motor current dynamics would help reduce high frequency vibration or chatter experienced when trying to increase the network's stiffness.

Increased viscous damping was found to theoretically allow a stiffer I/A network with a higher bandwidth, while decreasing transparency only over a limited frequency range. Transparency at low frequencies improved with increased damping through higher allowable integral force control. Similarly, increasing damping allows for much stiffer A/I network with higher bandwidth and improved transparency over a frequency range, with low frequency transparency being compromised due to the required increase in the coupling's grounded damping. These theoretical findings support claims by Colgate that device designers should design physical dissipation in their device to improve performance rather than concentrating on eliminating it. [24]

11.5 Experimental Validation

Haptic two–port networks were experimentally evaluated on HuRBiRT, a nonlinear haptic device. HuRBiRT's nonlinear characteristics include gravity, link dynamics, friction, saturation limits, and gear train dynamics (backlash, binding, etc.) that make it an excellent

experimental testbed. This research also included adding a passive actuator to one degree of freedom so that controlled increased physical damping could be experimentally investigated.

Experimental implementation confirmed several of the two–port network characteristic trends illustrated when numerically tuning. First, the duality between the I/A network's force controller and the A/I network's coupling was experimentally validated through using equivalent experimental procedures for their tuning. Second, the ability of force feedback to improve I/A network's transparency was experimentally demonstrated. While increasing force controller stiffness requires relaxing the virtual coupling, adding integration saturation limits allowed increasing coupling stiffness with minimal compromise in transparency. Effects of increased damping were also experimentally confirmed on axis #2, specifically increasing allowable I/A network stiffness and bandwidth. Unfortunately due to real world system properties, increase in allowable A/I network stiffness through increased physical damping could not be validated; though it was experimentally validated that increasing physical damping resulted in a decrease in A/I network transparency due to an increase in required coupling grounded damping, B_G. Expanded coupling forms were also experimentally investigated, with practical issues forcing the final implementation forms to take on simpler models selected through insight gained from the more complicated numerically tuned coupling. Though incorporation of the force controller theoretically required an I/A virtual coupling with a damper in series, experimental testing showed it was not required. Possibly additional device dissipation or the experimental integrator saturation limits help reduce the need for "stress relaxing" behavior in the coupling.

It was found that network parameters derived from numerically tuning the linearized models were usually conservative with respect to what was experimentally possible. One extreme difference was that experimental A/I networks could use much more transparent coupling than that derived from numerically tuning the models. This proved to produce an experimental A/I network with much higher bandwidth than anticipated. There are several possible reasons for the experimental results being more aggressive than the numerical

predictions. First, models for HuRBiRT were formulated to conservatively estimate the equivalent damping of friction and underestimate the low frequency dissipation provided by coulomb friction, while other dynamic elements in the system not included in the modeling may have added to energy dissipation in HuRBiRT. Furthermore passivity is not a required condition for stability, rather a sufficient condition. Even though a system may violate passivity it can still be stable, especially if the magnitude response is significantly attenuated at the frequency in which passivity is violated. While interaction energy was experimentally monitored, it was used more for tuning network transparency than stiffness, with system stability being the dominant factor when selecting the A/I velocity controller and I/A virtual coupling. Numerical tuning investigated all frequencies up to the Nyquist frequency, while real system signals are band limited to much lower frequencies. For example, the human operator's bandwidth for moving HuRBiRT and experimentally testing transparency is limited to around 3 Hz, effectively allowing experimental tuning to neglect higher frequency signals. Chapter 10 covered some initial investigation of limiting the "tuning" bandwidth, showing it allows more aggressive parameter selection.

Llewelyn's stability is derived to guarantee passive port interaction when the second port is terminated by any passive one–port. When Llewelyn's third stability condition is violated it does not necessarily mean the network will respond actively when interfaced with all given environments. It is possible to tune a two–port network with passive dynamic impedance or admittance limits (Z_{min} & Y_{max}) and Z_{max} & Y_{min})) and that passively reflects most terminating ports, but violates the third stability condition and therefore there exists a range of passive terminating one–port interactions that will cause the two–port to behave actively over a set frequency range. If the two–port network never interacts with an environment in this range then it will remain passive to the user. It is possible some of the experimental virtual couplings chosen may have provided a passive interface for all tested environments, but that there may exist a small range of virtual impedance or admittance that cause the network to respond actively.

11.6 Suggested Direction of Continuing Research

While this research worked to increase the understanding and expand the complexity of haptic two–port networks, there are still several directions for further development of said networks. This section will briefly discuss some of these directions, specifically the following areas will be discussed.

1. Experimental exploration of EMF damping in two–port networks.
2. Investigate intelligent control of the Magneto–Rheological brake, rather than using it as an adjustable damper.
3. Applications of two–port networks to devices that use non back drivable actuators, such as hydraulics, non back drivable gear trains, etc.
4. Further development of human dynamic models.
5. Transformation of joint space haptic two–port networks to end effector space via jacobian and inverse kinematics.
6. Investigation of time delay in environment / coupling communication.
7. Experimental exploration of two–port networks for forming bilateral teleoperation systems.

EMF damping proved beneficial when numerically tuning the two port networks. HuRBiRT was affected by high frequency jitter when experimentally trying to use high control damping or high proportional force feedback. It is hypothesized that high frequency back EMF damping and lag–lead motor current dynamics can be tunned to help filter out this less desirable high frequency response. Lag–lead dynamics in the force control can be investigated through numerical analysis and experimental implementation of an equivalent digital filter in the command signal to HuRBiRT's motor amplifiers, but this will not account for high frequency electrical damping.

The adjustable brake on HuRBiRT was used to mimic an adjustable damper for investigating the effects of changing linear viscous damping. Initial exploration of using the brake in a more intelligent manner was explored, but no conclusive results were sought. For example, the brake was used to only increase damping or fully engage at the virtual wall interface. Unfortunately the brake used on HuRBiRT is not strong enough to reflect an impenetrable wall, though its initial engagement does give the initial perception of a solid wall. Comparison of user perception when using the brake only, motor only, or brake and motor for reflecting stiff walls would add insight to the brake's effectiveness at improving virtual wall perception when not used as a viscous damper.

This research used a back drivable haptic system as the device model and experimental testbed. Formulation of the I/A network requires a system that can be back driven, but A/I network does not. Because they are capable of resisting high forces, it is often desirable to use a system that can not be back driven. Equation (45), through division of $\mathrm{Re}(H(j\omega))$ in the Llewelyn stability criterion, illustrates tuning the A/I network coupling theoretically requires compliance in the closed loop position control. Systems based on hydraulic manipulators and worm drives have minimal mechanical compliance and therefore theoretically require large A/I coupling real part; though it may be possible to introduce additional compliance through more complicated control. Furthermore, equation (114) suggest such required compliance may be accounted for through incorporation of human dynamic limits in the network. Experimentally implementing an A/I network on a non back drivable device may prove capable of providing a passive human–device interface.

As noted, human characteristics are an important topic in haptics control. While this research presents and demonstrates one possible model to be added to the list, much work still needs to be completed in order to characterize the human's dynamic characteristics when interfacing with man–machine systems. This research presented one example of where the human was not a passive element in the loop, countering accepted assumption in various

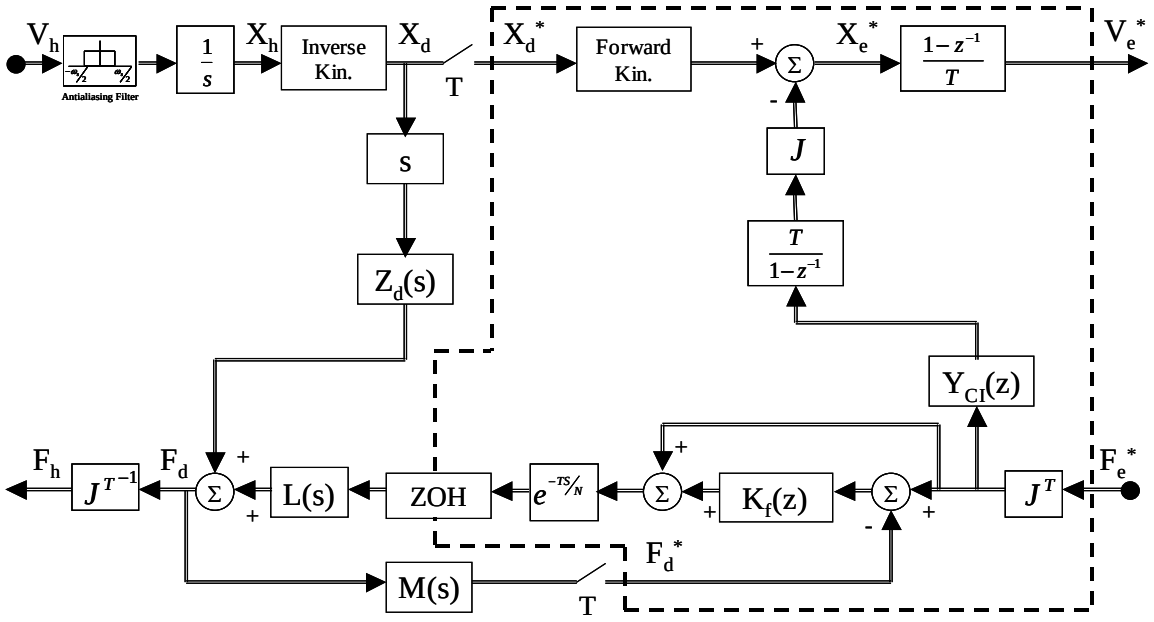

Figure 97: I/A Two–Port Network with Coordinate Transformation

haptic literature. More experimental work is required in the area of developing human dynamic models, or dynamic model limits. It is suggested that such models be derived from a sample of human subjects responding to different perturbation signals on various devices and arm movements / configurations. This would allow comparison of different human subjects, different arm configurations for different devices, and change in humans' response to different classes of perturbation signals. These different human models can then be used to see how their variance translates into variations of the two–port network parameter selection.

Many virtual environments and remote devices are structured to utilize user space coordinates, while haptic two–port network structures are formulated with respect to the haptic device's specific joint parameters. If the goal is to reflect virtual sensations not orthogonal to the device's joint space motion, then the environment coordinates must be transformed to the device's respective pair of joint coordinates. Robotics literature is rich in procedures for transferring joint space control to end effector control and figures 97 & 98 illustrate one proposed method of implementing the transformations in the haptic network structure. Both figures include illustration of communicating position instead of velocities as implemented on the experimental test bed. Transformation relies on both Jacobian and and

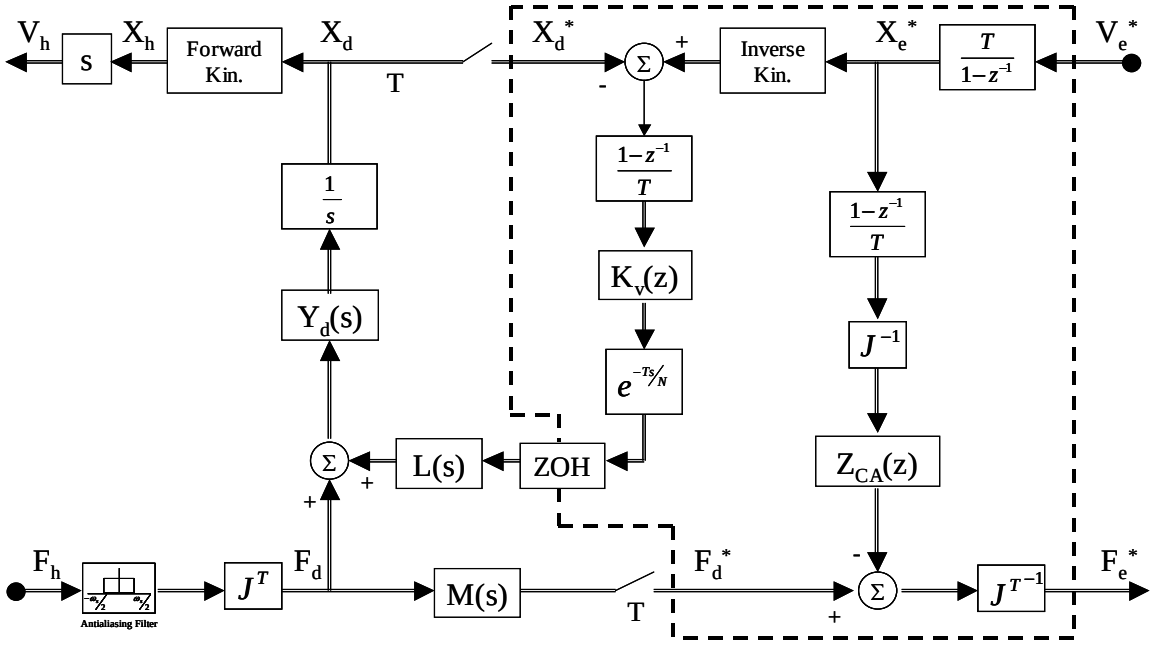

Figure 98: A/I Two–Port Network with Coordinate Transformation

inverse kinematics, which relies on measurement of the current position to calculate. This also requires separation of the virtual coupling from the environment, which is found to introduce delay into the system, another topic of interest.

Experimental implementation of the haptic two–port networks required combining the virtual environment with the coupling so as to guarantee there wasn't any time delay in the communication or algebraic loops in the numerical algorithms. Ideally it would be preferable to separate the coupling from the environment so that the networks can be used with slave devices and environment coordinates can be transformed to the required combination of haptic device's joint coordinates. Llewelyn's stability criterion relies on a passive environment, separating the environment from the coupling in numerical simulation will require a time step delay, which can cause the communicated virtual environment to no longer be passive. Several have investigated the topic of numerical environment simulations and conditions for guaranteeing passivity. With respect to two–port networks, this issue of time step delay can be approached through lumping the delay with the numerical environment and developing a criterion so that it remains passive, or through placing the delay within

the two–port network and investigating how it effects tuning of network parameters.

The beauty of two–port networks is their modular characteristics. To date this research has only used numerical virtual environments as the reflected haptic sensation. Next natural progression is to utilize haptic two–port networks for a master–slave system. Again, the notion of potential time delay and its effects on stability of the system will be a practical issue. It is suggested that the master–slave control be initially done with the same digital control system so that proof of concept can be demonstrated before addressing more complicated bilateral teleopertion systems that have long distance communication delay.

These proposed directions of continuing research would further build on the development of haptic two–port networks, understanding human interaction in man–machine devices, and the implementation of hybrid active / passive actuated haptic devices. While many of these topics have been touched upon in various haptic literature, very few have approached these topics through analysis of the two–port paradigm or application of virtual coupling for both impedance and admittance reflection. Hybrid active / passive haptic devices is an area of research that has seen little attention as few have explored the synergistic combination of active and passive actuators. Addressing these topics in haptics would help add insight to both design and control of haptic systems and ultimately further the development of applying modular haptic networks.

APPENDIX A

FRICTION (COULOMB DAMPING)

Real world mechanical systems usually include friction to some degree. While most designers try to minimize effects of friction, it is very difficult to completely eliminate. While nonlinear in nature, coulomb friction can be approximated with equivalent damping for a given forcing input. To illustrate the effects of friction on a system's frequency response, a simple mass with damping and friction is considered. Both friction and damping dissipate energy in a cycle for a given periodic input, therefore the equivalent damping for friction can be equated by looking at the dissipated energy per cycle. Total dissipated energy per cycle for a mass with friction and damping can be evaluated through

$$\Delta E/_{cycle} = \int_{cycle} \left(b_d v(t)^2 + F_f \text{sgn}(v(t)) v(t) \right) dt \tag{128}$$

First assume the input force is greater than friction force (F_f) and the system's steady state velocity is periodic with the form of

$$v(t) = V \cos(w_{dr} t - \Phi) \tag{129}$$

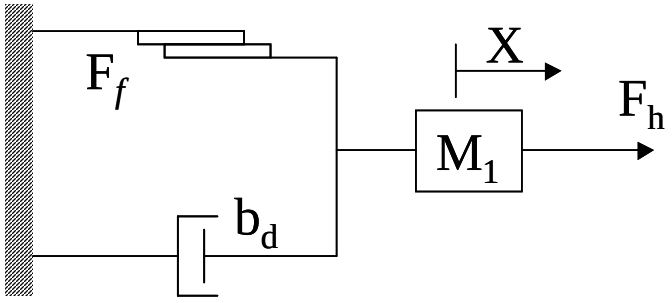

Figure 99: Mass with Viscous Damping and Coulomb friction

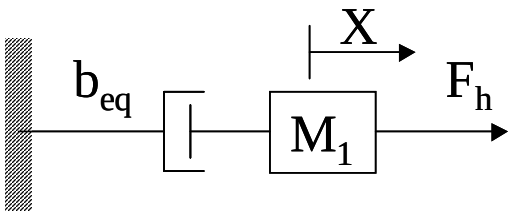

Figure 100: Mass with Equivalent Damping

where motion magnitude, V, and phase, F, may now be nonlinearly dependent on input magnitude. Evaluating the integral gives

$$\Delta E/_{cycle} = \frac{\pi b_d V^2}{\omega_{dr}} + \frac{4F_f V}{\omega_{dr}} \tag{130}$$

For a system with only pure damping, the energy loss per cycle is

$$\Delta E/_{cycle} = \frac{\pi b V^2}{\omega_{dr}} \tag{131}$$

Equating the two expressions result in an estimation of equivalent system damping as

$$b_{eq} = b_d + \frac{4F_f}{\pi V} = b_d + \frac{h}{V} \tag{132}$$

Essentially the equivalent damping of friction force is a scaling based on magnitude of the velocity response. This should not be too surprising since damping force is linearly based on velocity and magnitude of friction force is independent of velocity, just dependent on the sign of velocity.

It is evident the equivalent damping of the friction element depends on the magnitude of velocity, which is related to the magnitude of applied force. To simplify the discussion, it will be assumed the physical damper is removed from the original system and only friction is left to dissipate energy. Substituting the equivalent damping into the steady state frequency velocity response of a mass with damping results in

$$V = \frac{\sqrt{F_{in}^2 - h^2}}{m\omega_{dr}} \quad , \quad \Phi = \tan^{-1}\left(\frac{\sqrt{F_{in}^2 - h^2}}{h}\right) \tag{133}$$

with equivalent damping for the cycle equaling

$$b_{eq} = \frac{m\omega_{dr} h}{\sqrt{F_{in}^2 - h^2}} \tag{134}$$

If it is assumed the forcing function is greater than friction the expression within the radical will be a positive value. If force is the input, the output velocity magnitude is now linearly dependent on the input frequency's inverse and nonlinearly dependent on input force amplitude. The interesting relationship is that equivalent phase is independent of input frequency, but dependent on magnitude of the input force. Similarly to raising physical dampening, raising friction reduces the phase angle, as well as lowering the magnitude of the velocity response. If one were to assume F_{in} is much larger than h ($F_{in} >> h$), the equations conveniently simplify to

$$V = \frac{F_{in}}{m\omega_{dr}} \quad , \quad \Phi = \tan^{-1}\left(\frac{F_{in}}{h}\right) \tag{135}$$

with equivalent damping for the cycle equaling

$$b_{eq} = \frac{m\omega_{dr}h}{F_{in}} \tag{136}$$

Though these linear approximations of non-linear friction may not be ideal, they help show the effect of friction and how it applies to the frequency response of a system. It is evident friction helps reduce the phase of the system for all frequencies, while having minimal affect on magnitude of the output. Similar analysis can be done for a second order system with stiffness, resulting in parallel results.

APPENDIX B

DC MOTOR BACK EMF DAPMING

Using dissipative actuators in conjunction with active actuators, creating a hybrid active / passive device, is one method of designing dissipation into the physical system. If a haptic device uses traditional DC motors it is possible to increase the device's energy dissipation through utilizing the motors' back EMF. For example, if one were to disconnect a motor's leads from its amplifier driver and short them together the motor's shaft impedance dynamics would be that of a damper with inertia. As the motor is turned it generates back EMF proportional to haft velocity, which generates a current proportional to motor resistance and proportional to the shaft's resistive torque. When controlling a motor in current mode (torque control) driver amplifier circuits compensate for any back EMF through its own internal controls. If, as illustrated in figure 101, an appropriate circuit element (Z_b) were wired in parallel with the motor leads it is possible to harness the motor's back EMF to provide additional physical damping.

Table 24: Nomenclature EMF Damping Schematic

Variable	Units	Description
R_t	ohms	Motor Resistance
L_m	H	Motor Inductance
K_v	V/RPM	Motor Back EMF Constant
K_t	(N-m)/amp	Motor Torque Constant
Θ_m	rad	Motor Shaft Position
T_m	N-m	Motor Shaft Torque
GR	NA	Gear Ratio
Θ_L	rad	Link Position
T_L	N-m	Link Torque

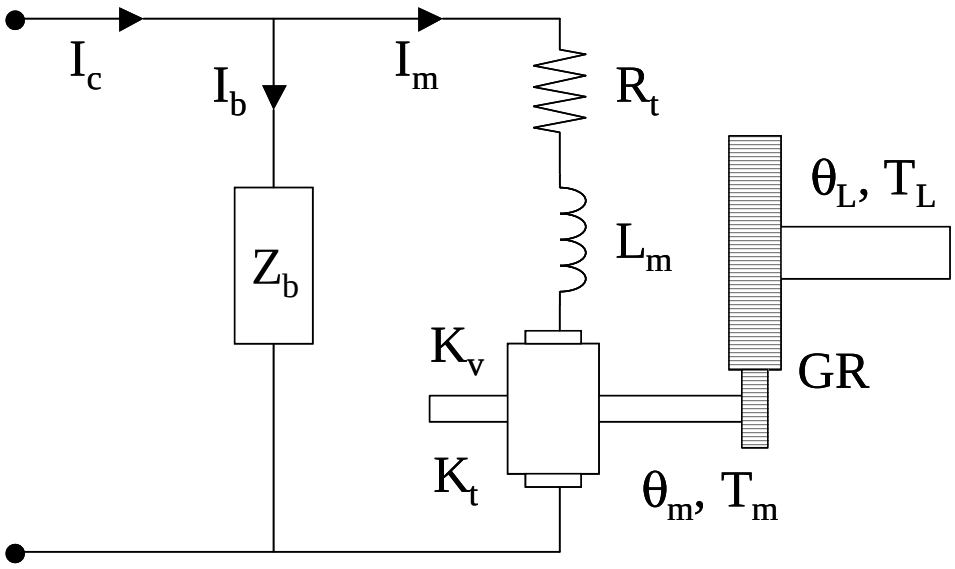

Figure 101: EMF Damping Schematic

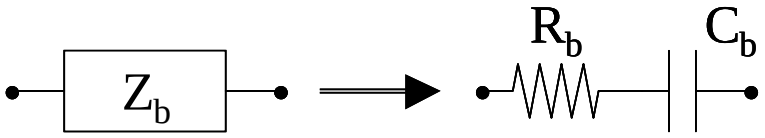

Figure 102: EMF Damping Schematic

Neglecting shaft / gear train inertia and viscous damping, which are both already accounted for in the haptic device's base dynamic model, the dynamic equations for figure 101 can be expressed as

$$I_m = \frac{Z_b}{Z_b + (R_t + L_m s)} I_c - \frac{\hat{K}_v}{Z_b + (R_t + L_m s)} \dot{\Theta}_m \tag{137}$$

This equation can be split into two elements. The first is a lag–lead effect on "motor current" given "control current". The second is a motor reverse current generated from back EMF, which is proportional to shaft velocity, and will lead to a damping effect. Choosing a resistor and capacitor in series, as illustrated in figure 102, for the parallel circuit results in

$$Z_b = \frac{R_b C_b s + 1}{C_b s} \tag{138}$$

Remembering that applied motor torque is proportional to motor current, using equation (138) in equation (137) and neglecting motor inductance results in a lag–lead "link torque"

versus "controller torque" dynamics of

$$\frac{T_L}{T_c} = \frac{I_m}{I_c} = \frac{R_b C_b s + 1}{(R_b + R_t) C_b s + 1} \tag{139}$$

Furthermore, back EMF results in an equivalent link damping of

$$\frac{B_{L,EMF}}{\dot{\Theta}_L} = \frac{\hat{K}_v K_t G R^2 C_b s}{(R_b + R_t) C_b s + 1} \tag{140}$$

which acts like a high pass damping element; where $\hat{K}_v$ is the motor back EMF constant with approiate units (V/(rad/s)).

Both the motor lag–lead dynamics and the high pass damping element share the same corner frequency of

$$F_{c,EMF} = \frac{1}{2\pi} \frac{1}{(R_b + R_t) C_b} \tag{141}$$

with the lag–lead's high frequency attenuation being

$$\frac{R_b}{(R_b + R_t)} \tag{142}$$

and the high frequency back EMF damping being equal to

$$\frac{\hat{K}_v K_t G R^2}{(R_b + R_t)} \tag{143}$$

Selection of the components R_b and C_b in Z_b is not a trivial process, requiring a balance between lowering corner frequency for increased low frequency damping, increasing magitude of back EMF damping, and minimizing the lag–lead's attenuation at low frequencies. Chapter 9 offers some comments on selecting R_b and $F_{c,EMF}$ for one of HuRBiRT's links and explores the effect of EMF damping on tuning the two–port haptic networks.

REFERENCES

[1] Adams, R. J. and Hannaford, B., "A two-port framework for the design of unconditionally stable haptic interfaces," in *International Conference on Intelligent Robots and Systems*, (Victoria, B.C.), pp. 1254–9.

[2] Adams, R. J. and Hannaford, B., "Stable haptic interaction with virtual environments," *IEE Transactions on Robotics and Automation*, vol. 15, no. 3, pp. 465 – 474, 1999.

[3] Adams, R. J. and Hannaford, B., "Control law design for haptic interfaces to virtual reality," *IEE Transaction on Control Sysems Technlogy*, vol. 10, no. 1 (January), 2002.

[4] Adams, R. J., Klowden, D., and Hannaford, B., "Stable haptic interaction using the excalibur force display," in *IEE International Conference on Robotics & Automation*, (San Francisco, CA), pp. 770 – 775.

[5] Adams, R. J., Moreyra, M. R., and Hannaford, B., "Stability and performance of haptic displays: Theory and experiments," in *ASME International Mechanical Engineering Congress and Exhibition*, (Anaheim, Ca), pp. 227–34.

[6] An, J. and Kwon, D.-S., "Haptic experimentation on a hybrid active/ passive force feedback device," in *IEEE International Conference on Robotics & Automation*, vol. 4, (Washington DC), pp. 4217–22, 2002.

[7] Anderson, R. J. and Spong, M. W., "Asymptotic stability for force reflecting teleoperators with time delay," *International Journal of Robotics Research*, vol. 11, no. 11, pp. 1350 – 149, 1992.

[8] Bendat, J. S. and Piersol, A. G., *Random Data: Analysis Measurement Procedures*. New York: Wiley–Interscience, 1971.

[9] Bendat, J. S. and Piersol, A. G., *Engineering Applications of Correlation and Spectral Analysis*. New York: Wiley–Interscience Publications, 1980.

[10] Blakelock, J. H., *Automatic Control of Aircraft & Missles*. New York: Wiley, 2 ed., 1991.

[11] Bolinder, E. F., "Survey of some properties of linear networks," *IRE Transactions on Circuit Theory*, pp. 70–78, 1957.

[12] Brown, J. M. and Colgate, J. E., "Minimum mass for haptic display simulation," in *ASME International Mechanical Engineering Congress and Exhibition*.

[13] Brown, J. M. and Colgate, J. E., "Physics–based approach to haptic display," in *International Symposium on Measurement and Control in Robotics*, (Houston, TX), pp. 101–106.

[14] Brown, J. M. and Colgate, J. E., "Passive implementation of multi body simulations for haptic display," in *ASM International Mechanical Engineering Congress and Exhibition*, vol. 61, pp. 85 – 92, 1997.

[15] Burghart, C., Krempien, R., Redlich, T., Pernozzoli, A., Grabowski, H., Munchenberg, J., Albers, J., Habfeld, S., Vahl, C., Rembold, U., and Worn, H., "Robot assisted craniofacial surgery: First evaluation," in *Computer Assisted Radiology and Surgery*, (Paris, France), pp. 828–833, 1999.

[16] Buttolo, P., Kung, D., and Hannaford, B., "Manipulation in real, virtual and remote environments," in *IEE conference on System, Man and Cybernetics*, vol. 5, (Vancouver, BC), pp. 4656–61.

[17] Cannon, S. C. and Zahalak, G. I., "The mechanical behavior of active human skeletal muscle in small oscillations," *Journal of Biomechanics*, vol. 15, no. 2, pp. 111–121, 1982.

[18] Carignan, C. R. and Clearly, K. R., "Closed-loop force control for haptic simulation of virtual environments," *Haptics–e*, vol. 1, no. 2.

[19] Chang, B. and Colgate, J. E., "Real-time impulse based simulation of rigid body systems for haptic display," in *International Mechanical Engineering Congress and Exhibition* (ASME, ed.), 1997.

[20] Cheah, C.-C. and Wang, D., "Learning impedance control for robotic manipulators," *IEE Transactions on Robotics and Automation*, vol. 14, no. 3, pp. 452 – 465.

[21] Chesney, C. C. W., *Implementation of a Planar Input Device with Hybrid Active / Passive Force Feedback*. PhD thesis, University of Florida.

[22] Colgate, J. E. and Brown, J. M., "Factors affecting the z -width of a haptic display," in *International Conference on Robotics & Automation*, (San Diego, Ca), pp. 3205–10.

[23] Colgate, J. E., Peshkin, M. A., and Wannasuphoprasit, W., "Nonholonomic haptic displays," in *IEE International Conference on Robotics & Automation*, (Minneapolis, Mn), pp. 539 – 544, 1996.

[24] Colgate, J. E. and Scenkel, G. G., "Passivity of a class of sampled-data systems: Application to haptic interfaces," *Journal of Robotic Systems*, vol. 14, no. 1, pp. 37–47, 1997.

[25] Colgate, J. E. and Shenkel, G., "Passivity of a class of sampled-data systems: Application to haptic interfaces," (Baltimore, Md), pp. 3236–3240.

[26] Colgate, J. E., Stanely, M. C., and Brown, J. M., "Issues in the haptic display of tool use," in *IEEE/RSJ International Conference on Intelligent Robots and Systems*, (Pittsburgh, Pa), pp. 140–145.

[27] Colgate, J. E., Wannasuphoprasit, W., and Peshkin, M. A., "Cobots: Robots for collaboration with human operators," in *Dynamic Systems and Control Division* (ASME, ed.), (Atlanta, GA), pp. 433–9, 1996.

[28] Contantinescu, D., Chau, I., DiMaio, S. P., Filipozzi, L., Salcudean, S. E., and Ghassemi, F., "Haptic rendering of planar rigid-body motion using redundant parallel mechanism," in *IEE International Conference on Robotics & Automation*, (San Francisco, Ca), pp. 2440 – 2445, 2000.

[29] Craig, J. J., *Introduction to Robotics Mechanics and Control*. second ed., 1989.

[30] d'Aulignac, D., Balaniuk, R., and Laugier, C., "A haptic interface for a virtual exam of the human thigh," in *IEEE International Conference on Robotics & Automation*, (San Francisco, Ca), pp. 2452 – 2457.

[31] Davies, B., "Synergistic robots in surgery - surgeons and robots working co - operatively," in *Experimental Robotics V* (Casals, A. and Almeida, A. T., eds.), (Barcelona, Catalonia), 1997.

[32] DiMaio, S., Salcudean, S., Reboulet, C., Tafazoli, S., and Hashtrudi-Zaad, K., "A virtual excavator for controller development and evaluation," in *IEE International Conference on Robotics & Automation*, (Leuven, Belgium), pp. 52 – 58, 1998.

[33] Dowling, N. E., *Mechanical Behaviour of Materials*. Upper Saddle River: Prentice Hall, 1993.

[34] Ellis, R. E., Sarkar, N., and Jenkins, M. A., "Numerical methods for the force reflection of contact," *ASME Transactions on Dynamic Systems, Measurements, and Control.*, vol. 119, no. 4, pp. 768–74.

[35] Erbse, S., Radermacher, K., Anton, M., Rau, G., Boeckmann, W., Jakse, G., and Staudte, H.-W., "Development of an automatic surgical holding system based on ergonomic analysis," in *CVRMed-MRCAS*, (Grtenoble, France), pp. 737–744, 1997.

[36] Fasse, E. D., "On the spatial compliance of robotic manipullators," *Journal of Dynamic Systems, Measurements, and Control*, vol. 119, no. December, pp. 839–843.

[37] Fasse, E. D., "A spatial compliance controller for serial manipulators," in *ASME Dynamics and Control Division*, vol. 58, pp. 607–613.

[38] Fasse, E. D., "Control of physical contact and dynamic interaction," in *Robotics Research, The Seventh International Symposium*, pp. 28 – 38, 1996.

[39] Fasse, E. D. and Broenink, J. F., "A spatial impedance controller for robotic manipulation," *IEE Transactions on Robotics and Automation*, vol. 13, no. 4, pp. 546 – 556.

[40] Fasse, E. D., Hogan, N., Gomez, S. R., and Mehta, N. R., "A novel variable mechanical - impedance electromechanical actuator," *Dynamic Systems and Control*, vol. 55-1, pp. 311 – 318.

[41] Fasse, E. D., Hogan, N., Kay, B. A., and Mussa-Ivaldi, F. A., "Haptic interaction with virtual object; spatial perception and motor control," *Biological Cybernetics*.

[42] Flite, K. B., Speich, J. E., and Goldfarb, M., "On the use of two channels for bilateral telemanipulation," in *International Mechanical Engineering Congress and Exposition* (ASME, D. S. and Division, C., eds.), vol. 69-2, (Orlando, Fl), pp. 1231–1238, 2000.

[43] Franklin, G. F., Powell, J. D., and Emami-Naeini, A., *Feedback Control of Dynamic Systems*. Reading: Addison–Wesley, third ed., 1994.

[44] Fung, Y., *Biomechanics, Mechanical Properties of Living Tissue*. New York: Springer, second ed., 1993.

[45] Furusho, J., Zhang, G., and Sakguchi, M., "Vibration suppression control of robot arms using homogeneous-type electrorheoligical fluid," in *International Conference on Robotics & Automation* (IEE, ed.), (Albuquerque, NM), pp. 3441–3448, 1997.

[46] Gillespie, B. R., Colgate, E. J., and Peshkin, M. A., "A general framework for cobot control," *IEEE Transactions on Robotics and Automation*, vol. 17, no. 4, pp. 391–401, 2001.

[47] Gillespie, R. B. and Colgate, J. E., "A survey of multibody dynamics for virtual environments," in *Dynamic Systems and Control Division* (ASME, ed.), (Dallas, TX), pp. 45–54, 1997.

[48] Gillespie, R. B. and Cutkosky, M. R., "Stable user - specific haptic rendering of the virtual wall," in *Dynamic Systems and Control Division* (ASME, ed.), (Atlanta, GA), pp. 397–406, 1996.

[49] Goswami, A. and Peshkin, M. A., "Mechanical computation for passive force control," in *International Conference on Robotics and Automation* (IEEE, ed.), (Atlanta, GA), pp. 476–83.

[50] Goswami, A. and Peshkin, M. A., "Task-space / joint-space damping transformations for passive redundant manipulators," in *International Conference on Robotics and Automation* (IEEE, ed.), (Atlanta, GA), pp. 642–7.

[51] Haddad, W. M. and Chellaboina, V.-S., *Nonlinear Dynamic Systems and Control: A Dissipative Systems Approach*. Atlanta: Authors, 2002.

[52] Hannaford, B., "A design framework for teleoperatoors with kineshetic feedback," *IEE Transactions on Robotics and Automation*, vol. 5, no. 4, pp. 426 – 434, 1989.

[53] Hannaford, B., Bejczy, A., Buttolo, P., Moreyra, M., and Venema, S., "Mini-teleoperation technology for space research," in *MIMR*, (Sendai, Japan).

[54] Hannaford, B. and Ryu, J.-H., "Time domain passivity control of haptic interfaces.," in *IEE International Conference on Robotics & Automation*, (Seoul, Korea), pp. 1863– 1869, 2001.

[55] Hannaford, B. and Ryu, J.-H., "Time-domain passivity control of haptic interfaces," *IEEE Transaction on Robotics and Automation*, vol. 18, no. 1 (February), 2002.

[56] Harris, S. J., Lin, W. J., Fan, K. L., Hibberd, R. D., Cobb, J., Middleton, R., and Davies, B. L., "Experienced with robotic systems for knee surgery," in *CVRMed-MRCAS*, (Grtenoble, France), pp. 757–766, 1997.

[57] Hashtrudi-Zaad, K. and Salcudean, S. E., "Analysis and evaluation of stability and performance robustness for teleoperation control architetures," in *IEE International Conference on Robotics & Automation*, (San Francisco, CA), pp. 3107 – 3113.

[58] Hashtrudi-Zaad, K. and Salcudean, S., "On the use of local force feedback for transparent teleoperation," in *International Conference on Robotics & Automation*, (Detroit, Mi), pp. 1863 – 1869, 1999.

[59] Haykin, S. S., *Active Network Theory*. Readiing: Addison-Wesley, 1970.

[60] Hinckley, K., Pausch, R., Goble, J. C., and Kassell, N. F., "Passive real world interface props for neurosurgical visualization," in *ACM CHI Conference on Human Factors in Computing Systems*, pp. 452–458.

[61] Hogan, N., "Controlling impedance at the man/machine interface," in *International Conference on Robotics and Autoation*, vol. 3, (Scottsdale, Az).

[62] Hogan, N., "Impedance control: An approach to manipulation, part 1 - theory," *Journal of Dynamic Systems, Measurements, and Control*, vol. 107, pp. 1 – 7.

[63] Hogan, N., "Impedance control: An approach to manipulation, part 2 - implementation," *Journal of Dynamic Systems, Measurements, and Control*, vol. 107, pp. 8 – 16.

[64] Hogan, N., "Impedance control: An approach to manipulation, part 3 - applications," *Journal of Dynamic Systems, Measurements, and Control*, vol. 107, pp. 17 – 24.

[65] Hollerbach, J. M., "Some current issues in haptics research," in *IEE International Conference on Robotics & Automation*, (San Francisco, Ca), pp. 757–762.

[66] Inaba, T. and Matsuo, Y., "Loop-shaping characteristics of a human operator in a force reflective manual control system," in *IEE International Conference on Systems, Man, and Cybernetics* (IEE, ed.), vol. 4, (Orlando, Fl), pp. 3621–3625, 1997.

[67] Ivanisevic, I. and Lumelsky, V., "Human augmentation in teleoperation of arm manipulators in an environment with obstacles," in *IEE International Conference on Robotics & Automation*, (San Francisco, Ca), pp. 1994–1999.

[68] Kazerooni, H., "Human–robot interaction via the transfer of power and information signals," *IEEE Transactions on Systems, Man and Cybernetics*, vol. 20, no. 2, pp. 450–63, 1990.

[69] Khalil, H. K., *Nonlinear Systems*. Upper Saddle River: Prentice Hall, third ed., 2002.

[70] Kichenman, M. and Goldfarb, M., "Implications of haptic interface force saturation on the haptic display of detail," in *International Mechanical Engineering Congress and Exposition* (ASME, D. S. and Division, C., eds.), vol. 69-2, (Orlando, Fl), pp. 1125–1131, 2000.

[71] Kikuchi, J., Takeo, K., and Kosuge, K., "Teleoperation system via computer network for dynamic environment," in *Bilateral Matched Impedance Teleoperation with Application to Excavator Control*, (Leuven, Belgium), 1998.

[72] Kim, Y. S. and Hannaford, B., "Some practical issues in time domain passivity control of haptic inerfaces," in *IEEE / RSJ International Conference on Intelligent Robots and Systems*, (Maui, Hi), pp. 1744–1750, 2001.

[73] Kosuge, K., Fujisawa, Y., and Fukudo, T., "Mechanical system control with man-machine-environment interactions," in *IEEE International Conference on Robotics and Automation*, vol. 1, (Atlanta, GA), pp. 239–44, 1993.

[74] Kosuge, K., Hashimoto, S., and Yoshida, H., "Human-robots collaboration system for flexible object handling," in *IEE International Conference on Robotics & Automation*, (Leuven, Belgium), pp. 1841 – 1846.

[75] Kosuge, K. and Murayama, H., "Teleoperation via computer network," *Electrical Engineering in Japan*, vol. 124, no. 3, pp. 49–56, 1998.

[76] Kuh, E. S. and Rohrer, R. A., *Theory of Active Linear Networks*. San Francisco: Holden - Day, 1967.

[77] Kuh, E. S. and Rohrer, R., *Theory of Linear Networks*. San Francisco: Holden-Day Inc., 1967.

[78] Kumar, R., Berkelman, P., Gupta, P., Barnes, A., Jensen, P. S., Whitcomb, L. L., and Taylor, R. H., "Preliminary experiments in cooperative human/robot force control for robot assisted microsurgical manipulation," in *International Conference on Robotics & Automation*, (San Francisco, Ca), pp. 610–617, IEE.

[79] Kunii, Y. and Hashimoto, H., "Virtual environment for haptic interface in robotic network systems," in *IEE International Conference on Robotics & Automation*, (Minneapolis, Mn), pp. 545 – 550.

[80] Lawrence, D. A., "Stability and transparency in bilateral teleoperation," *IEE Transactions on Robotics and Automation*, vol. 9, no. 5, pp. 624 – 637, 1993.

[81] Lerner, A. G., Stoianovici, D., Whitcomb, L. L., and Kavoussi, L. R., "A passive positioning and supporting device for surgical robots and instrumentation," in *Medical Image Computing and Computer-Assisted Intervention*, (Cambridge, UK), pp. 1052–61, 1999.

[82] Li, P. Y., "Passive control of bilateral tleoperation manipulators," in *American Control Conference*, vol. 6, (Philidelphia, Pa), pp. 3838–42.

[83] Li, P. Y. and Lee, D., "Passive feedforward approach to bilateral teleoperated manipulators," in *International Mechanical Engineering Congress and Exposition* (ASME, D. S. and Division, C., eds.), vol. 69-2, (Orlando, Fl), pp. 1153–1160, 2000.

[84] Llewellyn, F. B., "Some fundamental properties of transmission systems," in *I.R.E* (IRE, ed.), pp. 271–283, 1952.

[85] Loffler, M., Costescu, N., Zergeroglu, E., and Dawson, D., "Telerobotic decontamination and decommissioning qith qrobot, a pc-based robot control system," in *IEE International Symposium on Computer-Aided Control System Design*, pp. 24–29.

[86] Love, L., *Adaptive impedance control*. Ph.d., Georgia Institute of Technology, 1995.

[87] Love, L. J. and Book, W., "Design and control of a multiple-degree-of freedom haptic interface," in *International Mechanical Engineering Congress and Exposition* (DSC, A., ed.), (Chicago, Illinois), pp. 851–856, 1994.

[88] Lynch, K. M. and Liu, C., "Designing motion guides for ergonomic collaborative manipulation," in *IEEE International Conference on Robotics & Automation*, (San Francisco, Ca), pp. 2709 – 2715.

[89] Maneewarn, T. and Hannaford, B., "Haptic feedback of kinematic conditioning for telerobotic applications," in *Inernational Conference on Intelligent Robots and Systems*, (Victoria, B.C., Canada), pp. 1260 – 1265.

[90] Masamune, K., Kobayashi, E., Nakamura, R., Sakuma, I., Dohi, T., Isek, H., and Hashimoto, D., "Safety of medical aspects of safety," in *Computer Assisted Radiology and Surgery*, (Paris, France), pp. 808–812.

[91] McRuer, D., "Human dynamics in man-machine systems," *Automatica*, vol. 16, no. 3 (May), pp. 237–252, 1980.

[92] McRuer, D. T. and Jex, H. R., "A review of quasi-linear pilot models," *IEE Transactions on Human Factors in Electronics*, vol. 8, no. 3 (September), pp. 231–249, 1967.

[93] Miller, B. E., Colgate, E., and Freeman, R. A., "Passive implementation for a class of static nonlinear environments in haptic display," in *IEEE International Conference on Robotics & Automation*, (Detroit, Mi), pp. 2937 – 2942, 1999.

[94] Mitsuishi, M., Tomisaki, S., Yoshidome, T., Hashizume, H., and Fujiwara, K., "Tele–micro–surgery system with intelligent user interface," in *IEE International Conference on Robotics & Automation*, (San Francisco), pp. 1607 – 1614, 2000.

[95] Moore, C. A., Peshkin, M. A., and Colgate, E. J., "Cobot implementation of virtual paths and 3d virtual surfaces," *IEE Transactions on Robotics and Automation*, vol. 19, no. 2, pp. 347–51, 2003.

[96] Moore, C. A., Peshkin, M. A., and Colgate, J. E., "Design of a 3r cobot using continuously variable transmissions," in *IEEE International Conference on Robotics & Automation*, (Detroit, Mi), pp. 3249 – 3254.

[97] Moy, G., Singh, U., Tan, E., and Fearing, R. S., "Human psychophysics for teletaction system design," *Haptics-e*, vol. 1, no. 3.

[98] Munir, S., *Internet-based teleoperation*. Ph. d., Georgia Institute of Technology, 2001.

[99] Munir, S. and Book, W., "Internet based teleoperation using wave variables with prediction," in *International Conference on Advanced Intelligent Mechatronics. Proceedings (AIM)* (IEEE/ASME, ed.), (Como, Italy), pp. 43–50, 2001.

[100] Mussa-Ivaldi, F. A., Hogan, N., and Bizzi, E., "Neural, mechanical, and geometric factors subserving arm posture in humans," *The Journal of Neuroscience*, vol. 5, no. 10 (October), pp. 2732–2743, 1985.

[101] Ogata, K., *Discrete–Time Control Systems*. Englewood Cliffs: Prentice Hall, second ed., 1995.

[102] Ogata, K., *Modern Control Engineering*. Upper Sddle River: Prentice Hall, third ed., 1997.

[103] Ogata, K., *System Dynamics*. Upper Saddle River: Prentice Hall, third ed., 1998.

[104] Oh, Y. H., Chung, W. K., Jeong, K. W., and Youm, Y., "Implementation of passive hardware damper for force impact control," in *International Conference on Robotics Automation*, pp. 937–943.

[105] Peshkin, M., Colgate, J. E., and Moore, C., "Passive robots and haptic displays based on nonholonomic elements," in *IEE International Conference on Robotics & Automation*, (Minneapolis, Mn), pp. 551 – 556, 1996.

[106] Peshkin, M. A., Colgate, E. J., Wannasuphoprasit, W., Moore, C. A., and Gillespie, B. R., "Cobot architecture," *IEE Transactions on Robotics and Automation*, vol. 17, no. 4, pp. 377–90, 2001.

[107] Ruspini, D. C., Kolarov, K., and Khatib, O., "The haptic display of complex graphical environment," in *Computer Graphics Annual Conference*.

[108] Ruspini, D. C., Kolarov, K., and Khatib, O., "Haptic interaction in virtual environments," in *International Conference on Intelligent Robots and systems*, (Grenoble, France).

[109] Russo, M. and Tadros, A., "Controlling dissipative magnetic particle brakes in force reflective devices," in *Advances in Robotics*, vol. 42, (Anaheim, Ca), pp. 63–70.

[110] Russo, M. A., *The Design and Implementation of a Three Degree of Freedom Force Output Joystick*. Masters, Massachusetts Institute of Technology, 1990.

[111] Sakaguchi, M. and Furusho, J., "Development of er actuators and their applications to force display systems," in *Virtual Reality Annual International Symposium,* (IEE, ed.), pp. 66 – 70, 1998.

[112] Sakaguchi, M. and Furusho, J., "Force display system using particle-type electrorheological fluids," in *International Conference on Robotics & Automation* (IEE, ed.), (Leuven, Belgium), pp. 2586–2591, 1998.

[113] Sakaguchi, M. and Furusho, J., "Development of 2 dof force display system using er actuators," in *International Conference on Advanced Intelligent Mechatronics* (IEEE, A. ., ed.), (Atlanta, Ga), pp. 707–712, 1999.

[114] Sakaguchi, M., Furusho, J., and Genda, E., "Basic study on rehabilitation training system sing er actuators," in *IEEE International Conference on Systems, Man, and Cybernetics* (SMC, I. ., ed.), pp. 135 –140, 1999.

[115] Sakaguchi, M., Zhang, G., and Furusho, J., "Modeling and motion control of an actuator unit," in *International Conference on Robotics & Automation* (IEE, ed.), (San Francisco, Ca), pp. 1347 – 1353, 2000.

[116] Salcudean, S. E., Hashtrudi-Zaad, K., Tafazoli, S., DiMaio, S. P., and Reboulet, C., "Bilateral matched-impedance teleoperation with application to excavator control," *IEE Control System Magazine*, vol. 19, no. 6, pp. 29 – 37, 1999.

[117] Salcudean, S. E., Tafazoli, S., Hashtrudi-Zaad, K., and Lawrence, P., "Evaluation of impedance and teleoperation control of a hydraulic mini-excavator," in *Experimental RoboticsV. The Fith International Symposium*, pp. 229–240.

[118] Salcudean, S., Hashtrudi-Zaad, K., Tafazoli, S., DiMaio, S., and Reboulet, C., "Bilateral matched impedance teleoperation with application to excavator control," in *IEE International Conference on Robotics & Automation*, (Leuven, Belgium), pp. 133 – 139.

[119] Salcudean, S. E., "Control for teleoperaton and haptic interfaces," in *Control Problems in Robotics and Automation, International Workshop*, (San Diego), pp. 51–66.

[120] Schneider, O., Troccaz, J., Chavanon, O., and Blin, D., "Padyc: a synergistic robot for cardiac puncturing," in *IEEE International Conference on Robotics & Automation*, (San Francisco, Ca), pp. 2883 – 2888.

[121] Schneider, O., Troccaz, J., Chavanon, O., and Blin, D., "Synergistic robotic assistance to cardiac procedures," in *Computer Assisted Radiology and Surgery*, (Paris, France), pp. 803–807.

[122] Schutter, J. D., Bruyninckx, H., Zhu, W.-H., and Spong, M. W., "Force control: a bird's eye view," in *Control Problems in Robotics and Automation, International Workshop*, (San Diego, CA), pp. 1–17, 1997.

[123] Sciavicco, L. and Siciliano, B., *Modeling and Control of Robot Manipulators*. New York: McGraw–Hill, 1996.

[124] Sheridan, T. B. and Ferrell, W. R., *Man-Machine Systems*. Cambridge: The MIT Press, 1974.

[125] Sirouspour, M. R., Maio, S. P. D., Salcudean, S. E., Abolmaesumi, P., and Jones, C., "Haptic interface control - design issues and experiments with a planar device," in *IEEE International Conference on Robotics & Automation*, (San Francisco, Ca.).

[126] Sirouspour, M. R. and Salcudean, S. E., "On the nonlinear control of hydraulic servo-systems," in *IEE International Conference on Robotics & Automation*, (San Francisco, Ca), pp. 1276 – 1282, 2000.

[127] Slotine, J.-J. E. and Li, W., *Applied Nonliner Control*. Englewood Cliffs: Prentice Hall, 1991.

[128] Smith, M. J., *Tactile Interface for Three-Dimensional Computer-Simulated Environments: Experimentation and Design of a Brake-Motor Device*. Masters, Massachusetts Institute of Technology, 1988.

[129] Stocco, L., Salcudean, S. E., and Sassani, F., "Matrix normilization for optimal robot design," in *IEE International Conference on Robotics & Automation*, (Leuven, Belgium), pp. 1346 – 1351, 1998.

[130] Stoianovici, D., Whitcomb, L. L., Anderson, J. H., Taylor, R. H., and Kavoussi, L. R., "A modular surgical robotic system for imaging guided percutaneous procedures," in *Medical Image Computing and Computer-Assisted Intervention* (MICCAI', ed.), (Cambridge, MA), pp. 404–10, 1998.

[131] Stramigioli, S., Fasse, E. D., and Willems, J., "A rigorous framework for interactive robot control," *Submitted to Int. J. Control*.

[132] Tadros, A. H., *Control System Design for a Three Degree of Freedom Virtual Environment Simulator Using Motor/Brake Pair Actuators*. Masters, Massachusetts Institute of Technology, 1990.

[133] Tajima, F., Fujie, M. G., and Kanade, T., "Palm - v^2: A pasive articulated link mechanism with variable viscosity," in *Advanced Intelligent Mechatronics (AIM)*, (Tokyo, Ja).

[134] Takesue, N., Zhang, G., Furusho, J., and Sakaguchi, M., "Precise position control of robot arms using a homogeneous fluid," in *International Conference on Robotics & Automation* (IEE, ed.), (Leuven, Belgium), pp. 2470–2475, 1998.

[135] Takesue, N., Zhang, G., Furusho, J., and Sakaguchi, M., "High stiffness control of direct-drive motor system by a homogeneous er fluid," in *International Conference on Robotics & Automation* (IEE, ed.), (Detroit, Mi), pp. 188–192, 1999.

[136] Takesue, N., Zhang, G., Sakaguchi, M., Furusho, J., and Kiyosawa, Y., "Developmment and analysis of actuator with er damper," in *International Conference on Robotics & Automation*, (San Francisco, Ca), pp. 1328–1333.

[137] Tan, H. Z., Srinivasan, M. A., Eberman, B., and Cheng, B., "Human factors for the design of force-reflecting haptic interfaces," *Dynamic Systems and Control*, vol. 55, no. 1.

[138] Taylor, R. H., Jensen, P., Whitcomb, L. L., Barnes, A., Kumar, R., Stoianovici, D., Gupta, P., Wang, Z., deJuan, E., and Kavoussi, L. R., "A steady - hand robotic system for microsurgical augmentation," in *Medical Image Computing and Computer-Assisted Intervention*, (Cambridge, UK), 1999.

[139] Troccaz, J., Peshkin, M., and Davies, B., "Synergistic mechanical devices: a new generation of medical robots," in *Symposium on Robotics Research*, (Shonan, Japan), pp. 317–323.

[140] Troccaz, J., Peshkin, M., and Davies, B., "The use of localizers, robots and synergistic devices in cas," in *CVRMed-MRCAS*, (Grtenoble, France), pp. 727–736.

[141] Troccaz, J., Peshkin, M., and Savies, B., "Guiding systems for computer assisted surgery: introducing synergistic devices and discussing the different approaches.," *Medical Image Analysis*, vol. 2, no. 2, pp. 101 – 119.

[142] Troccaz, J. and Delnondedieu, Y., "Semi - active guiding systems in surgery. a two - dof prototype of the passive arm with dynamic constraints (padyc)," *Mechatronics*, vol. 6, no. 4, pp. 399 – 421.

[143] Tsumugiwa, T., Yokogawa, R., and Hara, K., "Variable impedance control based on estimation of human arm stiffness for human-robot cooperative calligraphic task," in *IEEE International Conference on Robotics and Automation*, vol. 1, (Piscataway, NJ), pp. 644–50, 2002.

[144] Venkataraman, S. T., Gulati, S., Barhen, J., and Toomarian, N., "A neural network based identification of environments models for compliant control of space robots," *IEE Transactions on Robotics and Automation*, vol. 9, no. October (5), pp. 685 – 697.

[145] Wannasuphoprasit, W., Akella, P., Peshkin, M., and Colgate, J. E., "Cobots: A novel material handling technology," in *International Mechanical Engineering Congress and Exposition* (ASME, ed.), (Anaheim, Ca), 1998.

[146] Wannasuphoprasit, W., Gillespie, R. B., Colgate, J. E., and Peshkin, M., "Cobot control," in *International Conference on Robotics and Automation* (IEEE, ed.), (Albuquerque, NM), pp. 3571–6, 1997.

[147] Wickens, C. D., *Engineering Psychology and Human Performance*. New York: Harper Collins, 2 ed., 1992.

[148] Will, C., III, C. D. C., and Adsit, P., "Implementation of a six-defree-of-freedom manual controller with passive force-feedback," in *SPIE – Telemanipulator and telepresence technologies*, (Philadelphia, Pennsylvania), pp. 1430–150.

[149] Xu, Y. and Hollerbach, J. M., "Effect of force perturbation on elbow joint pulse response in posture," in *International Conference of the IEEE Engineering in Medicine and Biology Society* (IEEE, ed.), (Baltimore, MD), pp. 426–7.

[150] Xu, Y. and Hollerbach, J. M., "Single trial versus ensemble data methods for identification of time-varying elbow joint dynamics," *?*, p. ?

[151] Yoshikawa, T., "Force control of robot manipulators," in *IEE International Conference on Robotics & Automation*, (San Francisco, Ca), pp. 220–226.

[152] Yoshikawa, T. and Yoshimoto, K., "Haptic simulation of assembly operation in virtual environment," in *International Mechanical Engineering Congress and Exposition* (ASME, D. S. and Division, C., eds.), vol. 69-2, (Orlando, Fl), pp. 1191–1198, 2000.

[153] Zhu, W. H., Salcudean, S. E., Bachmann, S., and Abolmaesumi, P., "Motion / force / image control of a diagnostic ultrasound robot," in *IEE International Conference on Robotics & Automation*, (San Francisco, Ca), pp. 1580 – 1585.

[154] Zhu, W.-H. and Salcudean, S. E., "Teleoperation with adaptive motion/force control," in *International Conference on Robotics & Automation*, (Detroit, Mi).

[155] Zhu, W.-H., Salcudean, S. E., and Zhu, M., "Experiments with transparent teleoperation under position and rate control," in *International Conference on Robotics & Automation*, (Detroit, Mi).

[156] Zilles, C. B. and J, K, S., "A constraint-based god-object method for haptic display," in *International Conference on Intelligent Robots and Systems*, (Pittsburgh, Pa), pp. 146–151.